NAVAL POSTGRADUATE SCHOOL

MONTEREY, CALIFORNIA

THESIS

ENHANCING MECHANICAL PROPERTIES OF COLD-SPRAYED ALUMINUM COATINGS USING GRAPHENE-NANOPLATELET AND MICRO-BORON-CARBIDE REINFORCEMENTS

by

Samuel P. Rice

June 2022

Thesis Advisor: Andy Nieto
Co-Advisor: Troy Ansell

THIS PAGE INTENTIONALLY LEFT BLANK

REPORT DOCUMENTATION PAGE			*Form Approved OMB No. 0704-0188*

1. AGENCY USE ONLY *(Leave blank)*	**2. REPORT DATE** June 2022	**3. REPORT TYPE AND DATES COVERED** Master's thesis

4. TITLE AND SUBTITLE
ENHANCING MECHANICAL PROPERTIES OF COLD-SPRAYED ALUMINUM COATINGS USING GRAPHENE-NANOPLATELET AND MICRO-BORON-CARBIDE REINFORCEMENTS

5. FUNDING NUMBERS
RMKAR

6. AUTHOR(S) Samuel P. Rice

7. PERFORMING ORGANIZATION NAME(S) AND ADDRESS(ES)
Naval Postgraduate School
Monterey, CA 93943-5000

8. PERFORMING ORGANIZATION REPORT NUMBER

9. SPONSORING / MONITORING AGENCY NAME(S) AND ADDRESS(ES)
ONR, Washington DC, 22217

10. SPONSORING / MONITORING AGENCY REPORT NUMBER

11. SUPPLEMENTARY NOTES The views expressed in this thesis are those of the author and do not reflect the official policy or position of the Department of Defense or the U.S. Government.

12a. DISTRIBUTION / AVAILABILITY STATEMENT
Approved for public release. Distribution is unlimited.

12b. DISTRIBUTION CODE
A

13. ABSTRACT (maximum 200 words)

This study explores the individual and combined reinforcement effects of graphene nanoplatelets (GNP) and micro-boron carbide (μB4C) in cold-sprayed Al matrix composite coatings. High energy ball milling was used to create compositions of 2 vol.% GNP, 2 vol.% μB4C, and one of 1 vol.% GNP with 1 vol.% μB4C. All reinforced compositions consisted of a total of 2 vol.% reinforcement to compare the effectiveness of single and dual reinforcement and not the amount of total reinforcement. Coatings were heat treated for 1 h at 400◦C to improve coating densification. Each coating was evaluated using microhardness tests, nanoindentation, dry-sliding wear tests, and adhesion tests. The coatings were also qualitatively evaluated using optical and scanning electron microscopy. All three reinforced coatings experienced a greater than 47% increase in microhardness after heat treatment than the control Al coating. Adhesion testing revealed that 2 vol.% μB4C and the dual-particle coatings had a 40% and 29% increase in adhesion strength, respectively. Most notably, nanoindentation showed that the dual-particle coating experienced a 17% increase in hardness and a 13% increase in elastic modulus compared to the unreinforced coating. The singly reinforced coatings either had the same or lower hardness and elastic modulus than the unreinforced coating.

14. SUBJECT TERMS
additive manufacturing, cold spray, nanoparticles, boron carbide, graphene nanoplatelets, adhesion, high energy ball milling, aerospace, composites

15. NUMBER OF PAGES
115

16. PRICE CODE

17. SECURITY CLASSIFICATION OF REPORT	**18. SECURITY CLASSIFICATION OF THIS PAGE**	**19. SECURITY CLASSIFICATION OF ABSTRACT**	**20. LIMITATION OF ABSTRACT**
Unclassified	Unclassified	Unclassified	UU

NSN 7540-01-280-5500

Standard Form 298 (Rev. 2-89)
Prescribed by ANSI Std. 239-18

THIS PAGE INTENTIONALLY LEFT BLANK

Approved for public release. Distribution is unlimited.

ENHANCING MECHANICAL PROPERTIES OF COLD-SPRAYED ALUMINUM COATINGS USING GRAPHENE-NANOPLATELET AND MICRO-BORON-CARBIDE REINFORCEMENTS

Samuel P. Rice
Ensign, United States Navy
BS, United States Naval Academy, 2021

Submitted in partial fulfillment of the
requirements for the degree of

MASTER OF SCIENCE IN MECHANICAL ENGINEERING

from the

NAVAL POSTGRADUATE SCHOOL
June 2022

Approved by: Andy Nieto
Advisor

Troy Ansell
Co-Advisor

Garth V. Hobson
Chair, Department of Mechanical and Aerospace Engineering

THIS PAGE INTENTIONALLY LEFT BLANK

ABSTRACT

This study explores the individual and combined reinforcement effects of graphene nanoplatelets (GNP) and micro-boron carbide (μB4C) in cold-sprayed Al matrix composite coatings. High energy ball milling was used to create compositions of 2 vol.% GNP, 2 vol.% μB4C, and one of 1 vol.% GNP with 1 vol.% μB4C. All reinforced compositions consisted of a total of 2 vol.% reinforcement to compare the effectiveness of single and dual reinforcement and not the amount of total reinforcement. Coatings were heat treated for 1 h at 400◦C to improve coating densification. Each coating was evaluated using microhardness tests, nanoindentation, dry-sliding wear tests, and adhesion tests. The coatings were also qualitatively evaluated using optical and scanning electron microscopy. All three reinforced coatings experienced a greater than 47% increase in microhardness after heat treatment than the control Al coating. Adhesion testing revealed that 2 vol.% μB4C and the dual-particle coatings had a 40% and 29% increase in adhesion strength, respectively. Most notably, nanoindentation showed that the dual-particle coating experienced a 17% increase in hardness and a 13% increase in elastic modulus compared to the unreinforced coating. The singly reinforced coatings either had the same or lower hardness and elastic modulus than the unreinforced coating.

THIS PAGE INTENTIONALLY LEFT BLANK

TABLE OF CONTENTS

LIST OF FIGURES

LIST OF TABLES

THIS PAGE INTENTIONALLY LEFT BLANK

LIST OF ACRONYMS AND ABBREVIATIONS

Al	aluminum
Al_2O_3	aluminum oxide, alumina
AM	additive manufacturing
BPR	ball-to-powder ratio
BNNP	boron nitride nanoplatelet
CNT	carbon nanotube
DOD	Department of Defense
EDS	energy-dispersive X-ray spectroscopy
GNP	graphene nanoplatelet
HEBM	high energy ball milling
MMC	metal matrix composite
μB_4C	micro-boron carbide
MW-CNT	multi-walled carbon nanotube
SEM	scanning electron microscope

THIS PAGE INTENTIONALLY LEFT BLANK

ACKNOWLEDGMENTS

I would first like to thank my advisor Dr. Andy Nieto for his help and guidance throughout this entire process. He truly pushed me to learn and apply knowledge thoroughly and thoughtfully. I would also like to thank my co-advisor, Dr. Troy Ansell, for his guidance and training me on much of the laboratory equipment. Finally, I would like to thank Captain Bradford Baker who first introduced me to the field of material science and additive manufacturing and helped me to gain this amazing opportunity through the Bowman Scholar program.

I would be remiss if I did not also thank my beautiful wife, who has stood by me and supported me. It is the daily encouragement and love from you that gives me the strength to better myself each day.

THIS PAGE INTENTIONALLY LEFT BLANK

I. MOTIVATION AND OBJECTIVES

A. MOTIVATION AND TECHNOLOGY BENEFITS

To date, there has not been any study on the cold spray process using a dual-nano-reinforced aluminum composite with graphene nanoplatelets (GNPs) and micro-boron carbide (μB_4C). This thesis aimed to investigate the synergistic effects between the two reinforcements to increase adhesion to an aluminum substrate.

The cold spray process can apply coatings to metals with vastly differing mechanical properties. Coatings with increased corrosion and wear resistance can be very useful to the military. The Department of Defense (DOD) spends over $23 billion on corrosion-related expenses every year, which is about 40% of the total DOD maintenance budget [1]. Specifically, for the Navy, corrosion is an everyday battle. The marine environment all navy vessels operate in can quickly corrode and wear down equipment. Surface wear on military equipment also causes eventual failure, depletes resources, and inhibits readiness. Cold spray provides a solution through lightweight metallic coatings that can be tailored to the machinery under wear or corrosion. The entire cold spray process could one day be on military platforms as a portable system. Cold spray can increase the life of military equipment and in the event of a mechanical failure, it could restore damaged materials to an operable status while waiting on replacement parts.

B. OBJECTIVES OF THESIS WORK

The overall objective for this thesis was to enhance the mechanical properties of cold-sprayed, pure aluminum powders with the addition of μB_4C and GNPs individually and in combination. The following three objectives articulate the experimental approach for attaining enhanced mechanical properties and their measurement.

- To synthesize hybrid powders and fabricate dual-particulate reinforced cold-sprayed aluminum nanocomposite coatings

A total of three compositional combinations of nano-reinforcements were tested: pure Al with 2 vol.% GNPs, pure Al with 2 vol.% μB_4C, and pure Al with 1 vol.% GNPs

and 1 vol.% μB_4C. A fourth powder, of pure Al, was also tested as a control for comparison. All powders were mixed using high-energy ball milling (HEBM) to avoid agglomeration of the nano-reinforcements. Then each powder was cold sprayed using identical parameters onto 6061 aluminum alloy substrates. Further discussion of the fabrication and cold spray process is discussed in Chapter III. Microstructural analysis of the sprayed layers was then conducted to confirm the presence of the nano-reinforcements in the composite and their effect on microstructure using optical microscopy, scanning electron microscopy, and energy dispersive spectroscopy.

- To improve adhesion strength and hardness using reinforcements

Each sample underwent several tests to determine changes in the mechanical properties of the coatings with and without reinforcements to determine improvement. Adhesion tests examined to what degree the composite coatings adhered to the substrate, or if the coatings had a cohesive failure. Material hardness was measured in a cross-section of each sample by micro-indentation. A series of wear tests were conducted to find the volume loss to determine wear resistance.

- To identify any synergistic effects

By creating samples of a similar volume percent of each reinforcement and one with the same amount of the combined reinforcements, the presence of synergistic effects can be determined. The objective was to compare the dual-reinforced coating to both the 2% μB_4C by volume and the 2% GNP by volume coatings. Any improvement in mechanical properties from this comparison would confirm the presence of synergistic effects. The next objective was to determine what physical phenomena were causing this improvement and how the GNPs and μB_4C interact within the coating using electron microscopy.

II. REVIEW OF THE STATE-OF-THE-ART

A. BACKGROUND

The cold spray process is an additive manufacturing method using metal powders to form coatings by the high-speed impact on a substrate. Figure 1 shows several types of thermal spray processes. Cold spray is desirable because the powders remain under the material's melting temperatures, thus retaining most of the physical and chemical properties found in the powder feedstock. Some thermal spray processes including cold spray allow for the addition of material reinforcements to create composite coatings with specific mechanical properties. The cold spray process's low temperatures also allow the use of nano-sized reinforcements that would otherwise be damaged by the increased temperature [2].

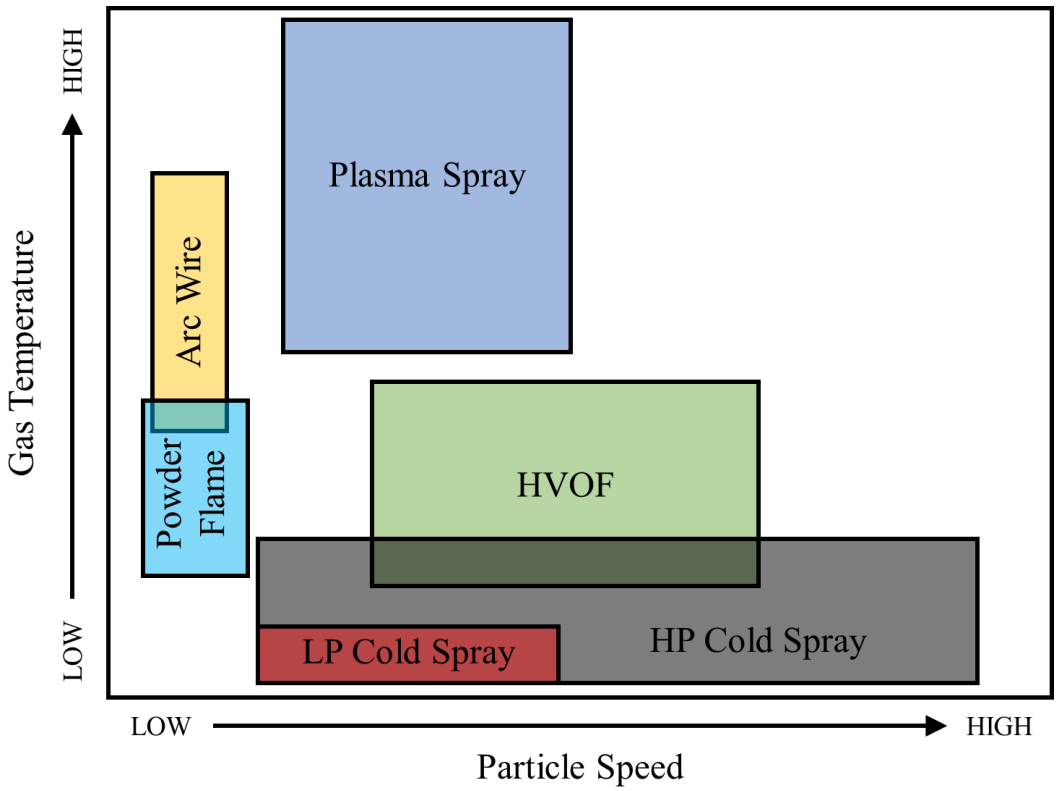

Figure 1. Varieties of thermal spray processes. Adapted from [2].

B. HOW COLD SPRAY WORKS

Cold spray deposition is characterized by two main processes: adhesion particles to a substrate and subsequent build-up into a bulk coating [3]. Each process has different bonding mechanisms. Adhesion at the interface experiences a high strain rate of plastic deformation under high-speed collisions of the particles initially on the substrate [4]. Then, as the deposit builds up, interparticle cohesion from the plastic deformation of the particles locks them together via overlapping splat boundaries [5].

The cold spray process propels the powders via a pressure difference over a converging-diverging nozzle, or De Laval nozzle. The converging part has gas flowing and accelerating at a subsonic velocity where the particles are then injected and entrained within the heated gas. The gasses used in cold spray are heated to temperatures below the melting temperature of the sprayed material [2]. In the diverging part, the gas expands and the velocity of the gas and particles is now supersonic. The rate of particle feed, temperature and pressure of the gas, and dimensions of the nozzle determine the characteristics of the particles in flight and their behavior upon impact on the substrate [6]. These impacts begin to form a deposit on the substrate by the modes of adhesion and cohesion described earlier. Figure 2 details the cold spray process and highlights the important parameters that affect the deposition of particles.

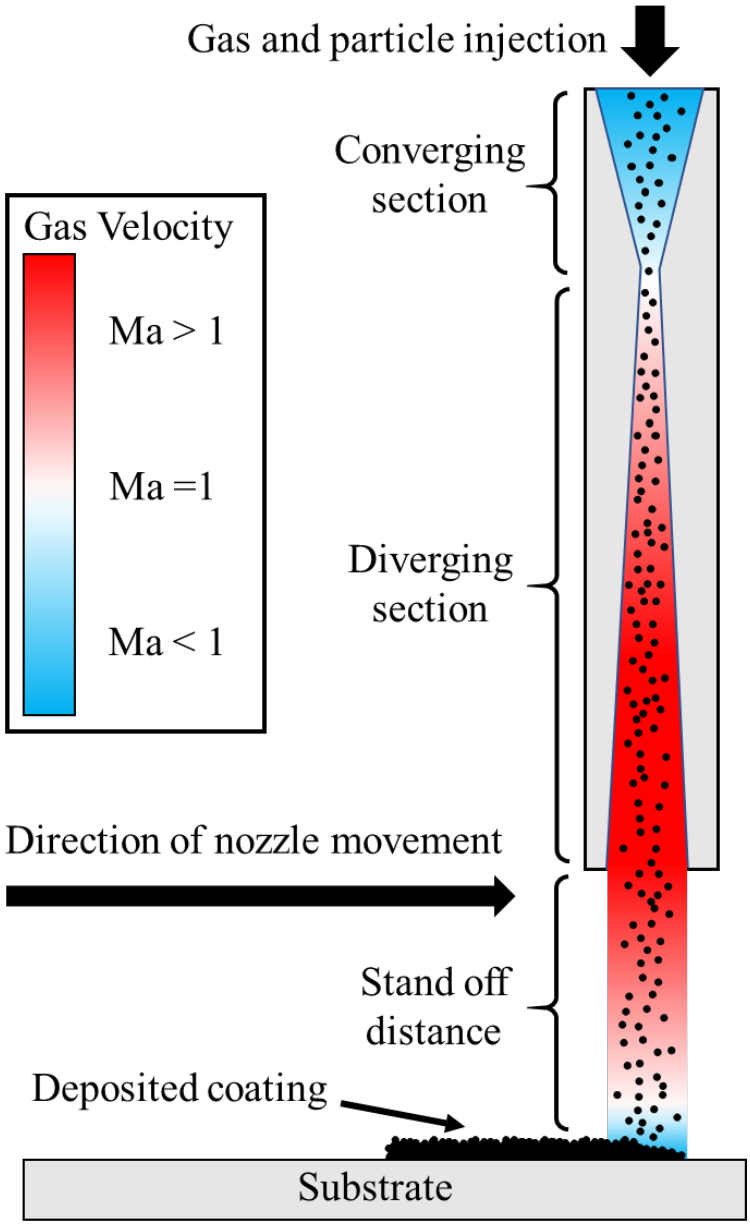

Figure 2. Cold spray process schematic

The cold spray process uses a heated gas as a propellant for particles, usually helium, or nitrogen, but the process also works with air. The gas is heated as it flows through a heater, then particles are injected downstream. This gas heats the particles as they are propelled to the substrate, and by increasing the temperature and pressure of this gas the particle temperature and velocity through the nozzle will increase [6]. This will make the particles more ductile and improve deposition efficiency. Although it is more

expensive than nitrogen, helium is the most efficient gas to use for cold spraying. Helium has a higher specific gas constant and lower molecular weight than nitrogen [6]. This combination allows helium to reach higher speeds than nitrogen in the nozzle at the choke point where the gasses reach Ma=1. Helium also allows for a higher working temperature and lower critical velocity, which means less is used while spraying [6]. Studies have shown helium to improve the densification of cold spray deposits [7].

Adhesion and cohesion of the deposited material on the substrate involve several bonding mechanisms: metallurgical bonding, mechanical anchoring, and interlocking or interfacial mixing [6]. These mechanisms all happen below the melting temperature of the metal particles, which ensures the mechanical properties of the particles are preserved. This phenomenon causes recrystallization and is sometimes referred to as hyper-quenching. Mechanical anchoring and interlocking are the primary bonding mechanisms of particles in a cold-sprayed coating. Particles are embedded in the substrate and the deformed particle boundaries overlap, anchoring and locking particles together. Particle embedment into the substrate is seen to increase when the substrate is a softer material such as a metal on polymer combination [6]. Interfacial mixing is an adhesion mechanism that involves interfacial vortices that mix the particles and substrate across the interface [6].

C. FACTORS THAT AFFECT ADHESION

One of the main factors affecting adhesion is the temperature and velocity of the particulates once they leave the opening of the nozzle. The kinematic behavior of the particle mid-flight is determined by several parameters such as temperature and speed of the gas, temperature of the particle, and material, shape, morphology, and distribution of particle sizes [6]. A particle's velocity and temperature characterize the particle's deposition capability called its deposition window [6]. The deposition window is the likelihood of the particle properly adhering to the substrate. The velocity of the particle is much easier to measure than its temperature due to its speed and small size. For a particle to adhere to the substrate, it must be deformed by the impact. The minimum speed required for particle deformation is called the critical velocity.

Particulates that deform upon impact with the substrate, known as a splat, are characterized by their dimensions using the flattening ratio. A higher flattening ratio means the particle will become more deformed following impact. A higher flattening ratio will also mean the particle will have a higher final surface area that can be used for bonding. The coating will then have lower porosity and increased adhesive/cohesive strength [4], [8]. The critical velocity and flattening ratio are greatly affected temperature of the gas propelling the particulates. Increased temperature will increase the ductility of the particle, which increases the flattening ratio and thereby decreases the critical velocity. A balance must be achieved between the temperature and velocity of the propelling gas to ensure the proper adhesion of particles onto the substrate. Depending on the particle size, these parameters can be adjusted. There is a direct correlation between particle size and its impact velocity; a particle with a smaller size will accelerate faster and have a higher impact velocity than a larger particle [9].

A second factor determining adhesion is the surface characteristics of the substrate. Increasing surface roughness and temperature of the substrate can increase the deposition window for some materials. Though it is known what interfacial mechanisms are desired for good adhesion, the required specifications on the input parameters to produce this reliable recipe for good adhesion remain unarticulated.

D. FACTORS THAT AFFECT WEAR RESISTANCE

Wear is defined as a gradual change in a specimen's mass or volume, sometimes with the creation of loose debris or a scar from the deformation of ductile material [10]. All wear is a process of plastic deformation. Tribology is the broad study of friction, lubrication during wear. There are several types of wear, but sliding and abrasive wear are most important to cold-sprayed coatings. Sliding wear is like abrasive wear except that the proportion of debris particles is low. These debris particles act as cutting chips that add grit to sliding wear and increase damage. In some metals, sliding wear transitions to abrasive wear due to third body effects, or debris particles that have been taken from the wear surface and now act abrasively on the wear surface [10].

There are currently many ways to test wear resistance, but all involve the same factors: normal load, sliding speed, ambient temperature and environment, sliding distance, and unidirectional or oscillating motion [10]. All these factors are linked, and by changing one, the other will have differing behaviors. Since there are such a large number of variables in wear testing, the data can be difficult to analyze and compare across methods. Some have tried to approximate the wear process with a simple linear equation that equates a volume loss over distance ratio to a load over hardness ratio, usually multiplied by a wear constant that corresponds to the severity of wear [10]. These types of equations have weaknesses when it comes to the existence of transitions, where the wear rate would change drastically [10]. Sliding and abrasive wear are characterized by large plastic strains, small cracks, complex loading patterns, and various surface effects [10]. Therefore, such simple equations limit what we can learn from wear testing. Instead, sliding and abrasive wear can be analyzed by looking at the details of plastic deformation and the size and shape of debris particles.

Of the factors that affect wear resistance, material hardness is the most influential. In general, a higher hardness will result in better wear resistance because the material is less likely to undergo plastic deformation. During sliding wear, the transfer of material between the wear surface and the counter surface is common [10]. This mechanism forms a tribo-layer that is subjected to large plastic strains, and its chemical composition is often different from the base material and oftentimes has a higher hardness than the base material. This will cause a smooth wear scar and irregular shapes and sizes of wear debris. If the mixed layer is not significantly harder, the wear scar will not press into the base material and will appear rough and have flake-like wear debris. In either case, the tribo-layer structure consists of fine grains of both the components, and the mixing process is similar to mechanical alloying with repeated deformation, fracture, and adhesion [10].

E. BORON CARBIDE REINFORCED COMPOSITES

1. Microstructure and Material Characteristics

The structural unit of B_4C consists of 12-atom icosahedra arranged in a rhombohedral lattice of trigonal symmetry [11]. This unit is formed because of boron's

ability to create caged structures forming two pentagonal pyramids bonded together at their bases [11]. The base unit of B_4C is shown in Figure 3.

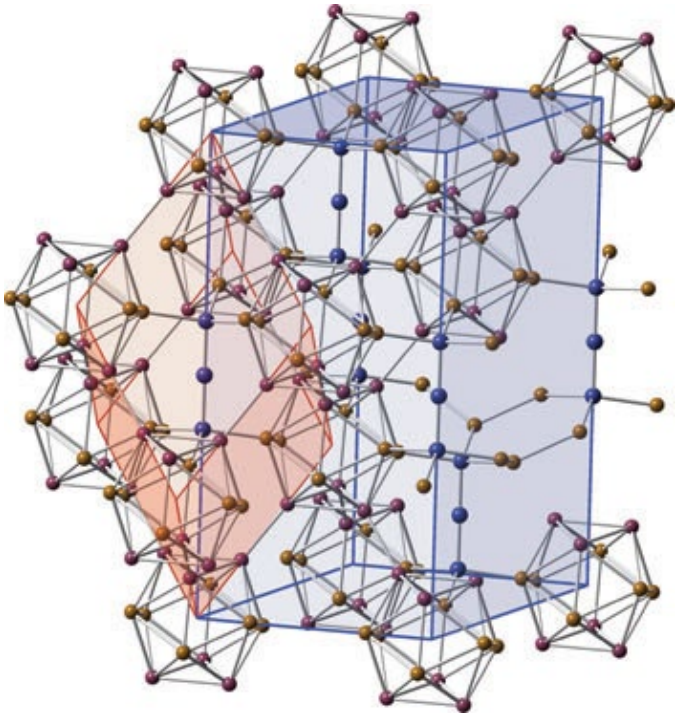

Figure 3. Boron carbide lattice. Source: [11].

Boron carbide melts at 2350ºC, boils above 3500ºC, has hardness up to 9.3 on the Rockwell scale, and has flexural strength that is greater than 400 MPa [12]. Boron carbide has a high thermal stability with a standard enthalpy of formation from -38.9 to -71.5 kJ/ mol [12]. Also, B_4C has anti-oxidation properties, high-temperature resistance, high strength, hardness, and elastic modulus [13]. B_4C is also known to have high wear-resistance, and good self-lubrication characteristics [13].

In an aluminum matrix composite, various sizes of B_4C particles: micro, sub-micro, and nano-B_4C, were compared by Nieto et al. [14]. It was found that micro and sub-micro B_4C particles did not exhibit any crystallographic orientation relationship with the Al matrix. The nano-B_4C, on the other hand, was found at grain boundaries and within the aluminum grains and shared parallel atomic plains. This strong interface between nano-

B_4C and aluminum has a higher bond strength than that found with larger B_4C particles [14].

Aside from the useful mechanical properties provided by the structure of B_4C, the material is also useful in nuclear applications. B_4C with naturally occurring boron has a 19.6 atomic percent natural abundance of Boron isotope B^{10}, which has an extraordinarily high thermal neutron capture cross-section of 3840 barns [15]. Today, B^{10} enriched B_4C can be easily purchased up to over 96% B^{10} in several forms, even in powders of less than 5 microns in size [16].

2. Mechanical Properties

Ceramics are known to enhance the mechanical properties of metal matrix composites (MMC) when added as reinforcements. This enhancement is due to ceramics having higher stiffness and hardness because of localized covalent bonds and higher inter-atomic electron density [11].

In an aluminum matrix composite, Rao et. Al. used a stir casting process to make Al-B_4C composites of differing B_4C wt%. This study found that increasing the amount of B_4C caused a decrease in density, and an increase in hardness relative to the amount of B_4C present. Compressive engineering stress vs. strain was also measured and showed an increase when B_4C was increased as shown in Figure 4. The number following the "A" is the wt% of B_4C in the composite. This increase in strength was attributed to the B_4C particles inhibiting dislocation movement in the Al matrix through a dispersion strengthening mechanism [17].

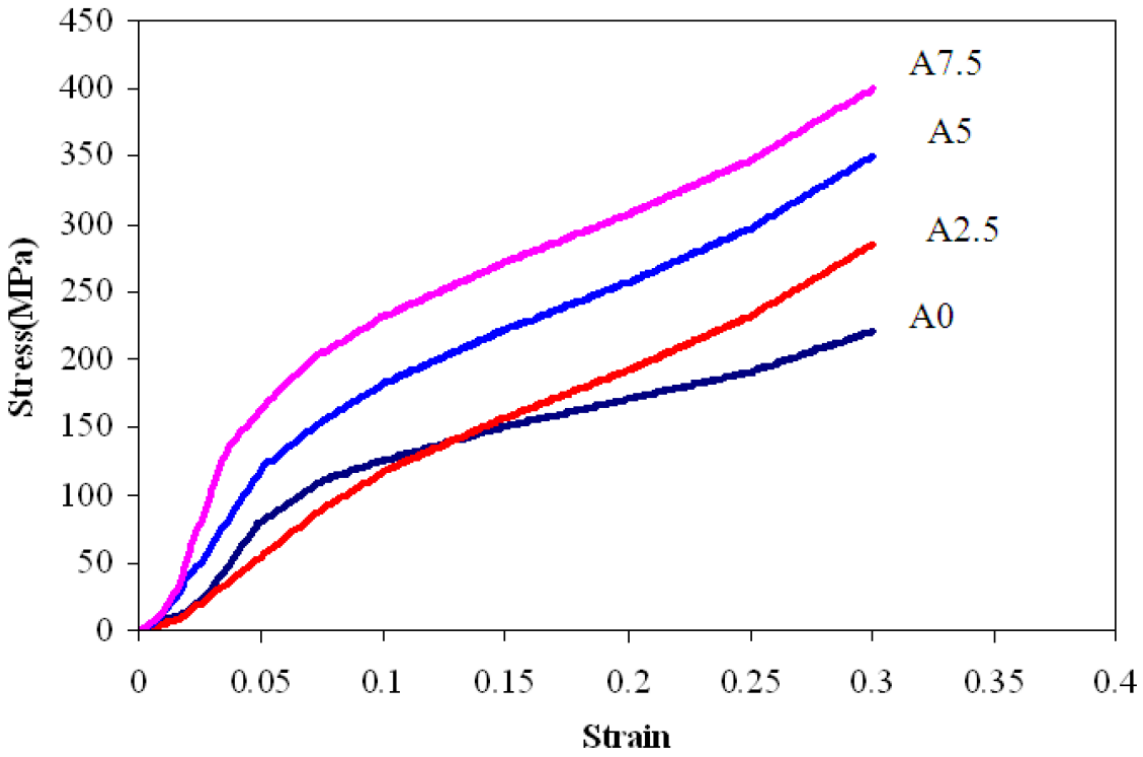

Figure 4. Compressive engineering stress vs. engineering strain for Al-B4C composites. Source: [17].

B_4C, being one of the hardest known ceramics, is ideal for high impact and high wear applications. The study by Nieto et al. found a 56% increase in hardness and a 7% increase in wear resistance of an aluminum matrix composite with nano-B_4C, while larger particle sizes led to smaller increases respectively [14].

3. Wear Behavior

The increase in the hardness of B_4C reinforced aluminum composites affects the abrasive wear resistance of the composite. The addition of B_4C particles reduces the depth to which abrasive particles can penetrate and reduces the ductility of the area being worn. Another method affecting wear resistance is particle pull-out. Under abrasive wear, a B_4C particle can be pulled out of the material, which dissipates energy and accelerates wear. The particle is now counted in the total volume lost to wear, and the surrounding area now has an open pore that can begin to crack and further decrease wear resistance [14].

F. GRAPHENE-NANOPLATELET REINFORCED COMPOSITES

1. Microstructure and Material Characteristics

Graphene is the basic structural unit of graphite. A graphene nanoplatelet (GNP) consists of 10–30 layers of graphene [18]. These layers contain sp^2-bonded carbon atoms that give graphene desirable in-plane mechanical properties such as high tensile strength (130 GPa) [19] and high Young's modulus (0.5–1 TPa) [20]. GNPs are also desirable because they are generally cheaper, easier to produce, and easier to disperse in a composite than either single-layer graphene or carbon nanotubes. GNPs also maintain their desirable mechanical, thermal, and electrical properties when combined in a composite material [21].

Since GNPs are formed from layers of graphene, the in-plane ultimate tensile strength of graphene may be high, but when dispersed into a composite as nanoplatelets, orientation matters. The strength of the stacked layers relies on van der Waals forces, so the tensile strength in the cross-plane direction is far weaker. Given this weak force keeping the planes together, sheets of graphene in a GNP can easily slip past one another.

2. Mechanical Properties

In a composite matrix, GNPs have four main strengthening mechanisms: grain refinement, Orowan Strengthening (resistance to passing dislocations), stress and load transfer, and increasing dislocation density by impeding dislocation motion. Good dispersion of GNPs in a composite is crucial for mechanical benefits to reach their potential. Large agglomerates must be broken up and dispersed well within the matrix. The large surface area of GNPs requires a large contact area within the composite matrix as seen in Figure 5. This strong interfacial bonding will ensure effective load transfer from the matrix to the reinforcement [22], [23].

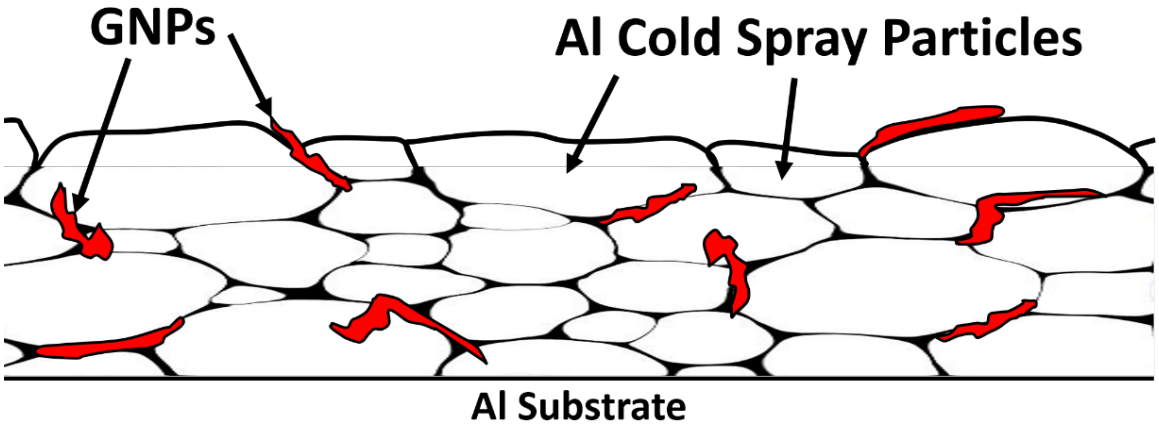

Figure 5. GNPs in aluminum cold spray composite

GNPs exhibit intrinsic energy dissipating mechanisms in ways different from other forms of graphene, such as nanotubes. These mechanisms are matrix-independent and consist of sheet kinking, sheet sliding, and out-of-plane compression. Sheet kinking has been shown to increase the plasticity of a matrix by bending the graphene sheets without damaging them [21], [22]. Sheet sliding, as discussed earlier, can provide friction between layers in a GNP. This friction absorbs energy that may reduce the spread of cracks in the matrix. The van der Waals forces between the sheets of graphene can be compressed in the out-of-plane direction. This compression absorbs energy that would otherwise cause damage via microcracks in the composite matrix [22].

It is unlikely that solid solution hardening or second phase hardening are present in GNP composites with aluminum because the solubility of carbon in aluminum is very low [23]. There should not be any new phases generated in an Al-GNP composite [23]. It is possible, however, that a formation of carbides can become present if the process reaches high enough temperatures.

3. Wear Behavior

In a metal-GNP composite, GNPs can be used as a solid lubricant since they have a high in-plane tensile strength, and easily slip past one another due to the weak van der Waals forces. This is a desirable trait because traditional lubricants are consumed under

wear and must be replaced, while an Al-GNP composite has an internal source of solid lubrication that replenishes as it is worn [22]. GNPs are chemically inert and maintain this solid lubrication property at high temperatures, unlike many commercial lubricants. GNP-MMCs have also shown an increase in surface hardness under wear due to work hardening, which will ultimately result in higher wear resistance [24].

G. HEAT TREATMENT OF COLD-SPRAYED COATINGS

Some mechanical properties can be improved in cold-sprayed coatings by heat treatment. Heat causes the sprayed coating to undergo the transitions shown in Figure 6. Cold-sprayed coatings can be heat treated just below the recrystallization temperature to maintain the desired material properties of the coating. Similarly, to the cold spraying process, the sprayed powder does not reach melting temperature and thus maintains bulk material properties. Figure 6 also shows the importance of having a dense coating before heat treatments. A coating with many pores will maintain those pores through the heating process, weakening the final coating.

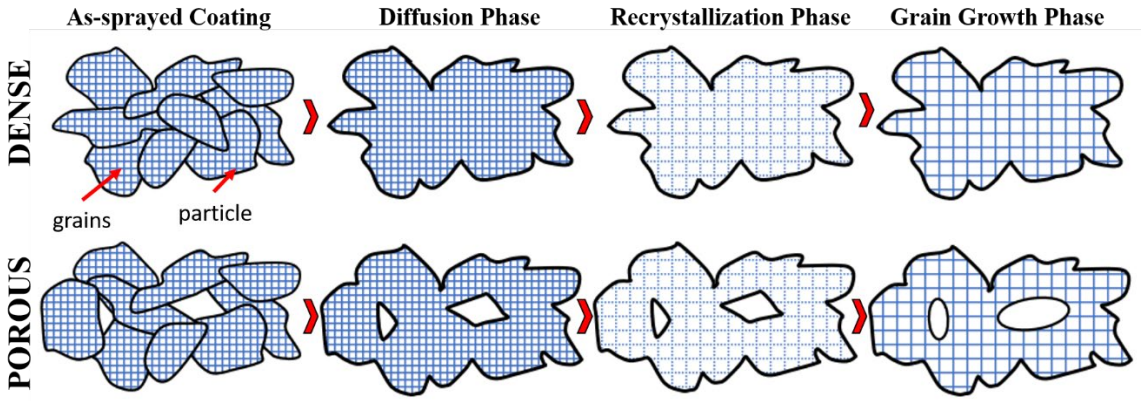

Figure 6. Schematic of cold-sprayed coatings during heat treatment

As the temperature increases, the interfaces of the particles begin to diffuse in the dense coating, becoming obscure, and only the compact interfaces in the porous coating diffuse. This diffusion of particle boundaries strengthens the coating, and all of the work hardening done to the particles during the spray process remains due to the low

temperatures. This strengthening will only be present in a lesser sense in porous coatings due to the lack of compact interfaces [25].

As the temperature is increased to the material's recrystallization temperature, the work hardening and dense accumulations of piled-up dislocations will begin to disappear. As the coating dwells at this temperature, the grains will begin to recrystallize and form smaller grains. If the temperature continues to increase, the coatings will undergo grain growth. A coating that has reached this point will likely plastically deform at a significantly lower yield strength [25]. This is generally undesirable in cold-sprayed coatings.

H. SYNERGISTIC EFFECTS OF DUAL NANO-REINFORCEMENTS

The idea that a synergistic effect could arise from dual nano-reinforcements in a cold-sprayed coating is a very new concept. A synergistic effect is when the combined effects of a least two substances work together in a unique way that creates a more significant impact than either substance on its own. While dual nano-reinforcements have been investigated in a few studies, only one has ever taken the approach through cold-sprayed materials [26]–[31].

In 2014, GNPs and multi-walled carbon nanotubes (MW-CNT) were added to pure magnesium and tested for synergistic properties [26]. The dual nano-reinforced Mg exhibited a higher failure strain than either of the singularly reinforced Mg composites. This increase confirmed the presence of a synergistic effect [26]. It was predicted that the synergistic effect was due to the constraining of agglomeration of GNPs by the one-dimensional MW-CNTs between sheets of GNPs. These three-dimensional structures would have been formed during a sonication process where the MW-CNTs intercalated between the layers of GNPs, causing an increase in surface area contact within the Mg matrix. An example of this physical combination of nano-reinforcements is shown in Figure 7. The MW-CNTs also act as extensions from the outside of these three-dimensional structures which can entangle among the matrix of the Mg composite [26].

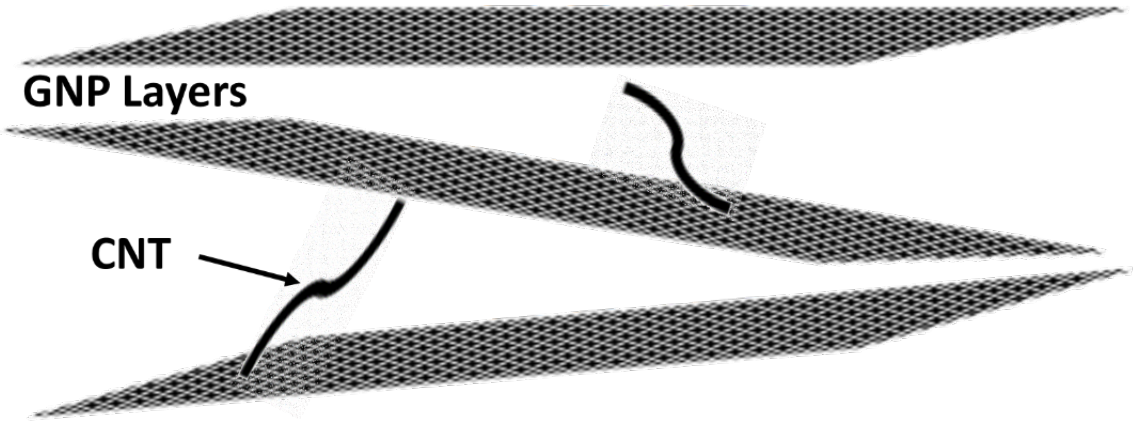

Figure 7. Sketch diagram of GNP-CNT hybrid structure. Adapted from [26].

In another study, aluminum matrix composites reinforced by carbon nanotubes (CNT) and silicon carbide nanoparticles were fabricated using HEBM and hot pressing [27]. The hardness of the dual nano-reinforced Al was up to eight times higher than that of pure Al, but this was not compared to Al reinforced with just silicon carbide nanoparticles or just CNTs using the same volume percent. One sample had 10% CNTs by volume and another had 10% CNTs and 10% SiC by volume, so any change in mechanical properties was likely due to the increase in total reinforcements in the composite rather than a synergistic effect. It is unknown if the two reinforcements had a synergistic effect, but this study did confirm that the addition of even a small amount of SiC nanoparticles helped to break up agglomerated CNTs and disperse them into the Al matrix [27].

Nano-diamond and MW-CNTs were used to reinforce aluminum matrix composites [28]. Like the previous study, this study created dual and single nano-reinforced Al composites for comparison. The single reinforced cases each had 1% reinforcement by volume and the dual case had 1% each by volume [28]. These samples cannot be properly compared to find synergistic effects because the dual case has twice the volume of nano-reinforcements.

In 2016, Al powder was mixed with B_4C and multi-walled CNTs in various concentrations and combinations [29]. This study found that the dual reinforced composite had better material properties than using just one reinforcement. This, however, did not determine synergistic effects because this and other studies compared coatings with two

nano-reinforcements to coatings with one using higher amounts of nanoparticles in the dual-system [28]–[31]. A composite with more nanoparticle reinforcement would be expected to have greater mechanical properties associated with the increased amount of reinforcement, which does not determine a synergistic effect.

In 2020, dual-nanoparticle reinforcements of nB_4C and boron nitride nanoplatelets (BNNP) were added to pure aluminum cold spray powders to examine the corrosion behavior of the coatings [32]. Equal amounts were added of single and dual reinforcements in each sample to properly assess the presence of synergistic effects. This study confirmed increased mechanical properties using nano-reinforcements but highlighted one major drawback. Coatings with nanoparticle reinforcement experienced increased pitting corrosion in a marine environment. This study attributed this loss of corrosion resistance to the presence of nanoparticles interrupting the formation of Al_2O_3 films, which led to localized corrosion. The study also noted galvanic corrosion occurring between the coating and its substrate, which had not been previously recorded to happen between cold spray coatings of the same material [32].

One expected synergistic method for an Al cold spray coating with μB_4C and GNP reinforcements is increased dispersion during milling. Similarly, to the study depicted in Figure 7, the μB_4C particles can help to split up the GNP layers and break up agglomerated GNPs by acting as an abrasive [26]. Once well dispersed in the Al powder, the reinforcements will be well dispersed in the composite coating where other strengthening mechanisms take place as that will be discussed later.

THIS PAGE INTENTIONALLY LEFT BLANK

III. EXPERIMENTAL METHODS AND MATERIALS

A. MATERIALS AND POWDER COMPOSITIONS

The base powder and reinforcements used are described in Table 1. The aluminum base powder and the reinforcements were milled together in the compositions described in Table 2.

Table 1. List of powders

	Composition	Powder Size	Vendor	Identification
Aluminum Powder	Al	-45 to +5 µm	SST Practical Cold Spray Coatings	SST-A5001
Boron Carbide (µB_4C)	B_4C	1-3 µm	US Research Nanomaterial Inc	B_4C Powder
Graphene Nanoplatelets (GNP)	C	Thickness: 6–8 nm Diameter: 15 µm	XG Sciences	xGnP M-15

Table 2. Sample compositions

Composition ID	Al [vol.%]	GNP [vol.%]	μB_4C [vol.%]
Pure Al	100	0	0
Al – GNP	98	2	0
Al – μB_4C	98	0	2
Al – GNP - μB_4C	98	1	1

To ensure enough of each powder composition was available for multiple coatings, 200 g of each composition was prepared. The compositions were measured using the manufacturers' values for powder densities recorded in Table 3.

Table 3. Densities of powders

Powder	Density [g/cm^3]
Al	2.66
GNP	2.52
μB_4C	2.11

Scanning electron microscope (SEM) images of the powder reinforcement are shown in Figures 8–10.

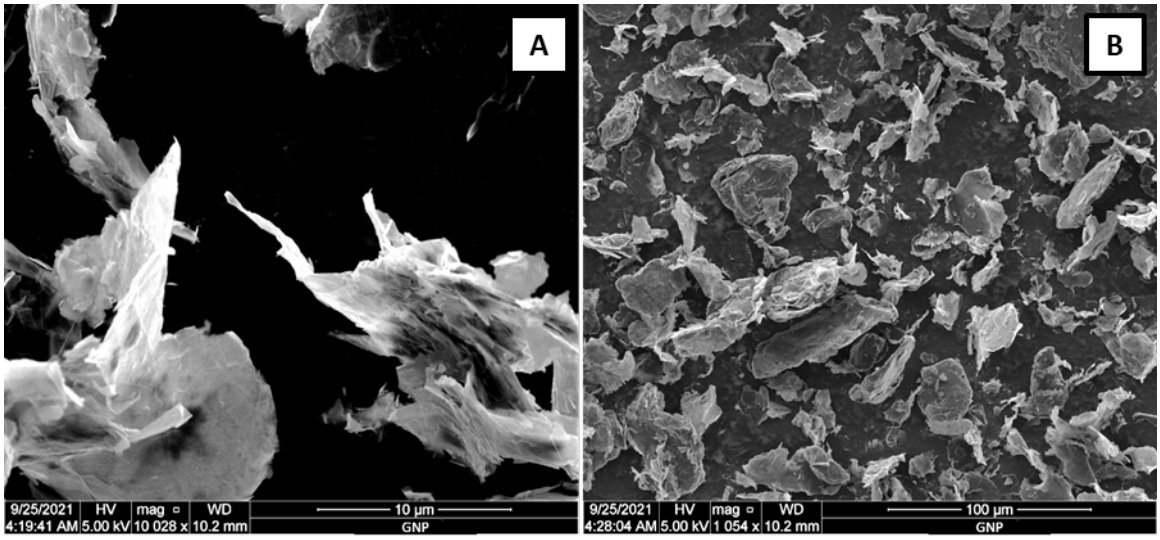

Figure 8. SEM image of a) single GNP clump, and b) many GNPs as received from XG Sciences

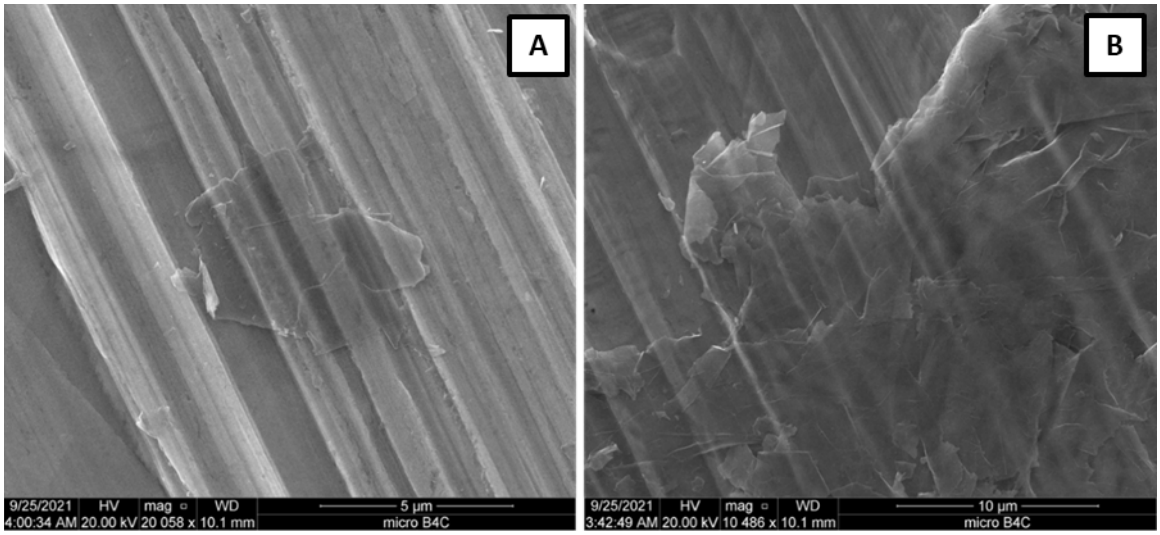

Figure 9. SEM image of a, b) GNP single layer over Cu tape

Figure 9 shows a single-layer GNP on a piece of Cu tape. The lines from the tape can be easily seen through the GNP.

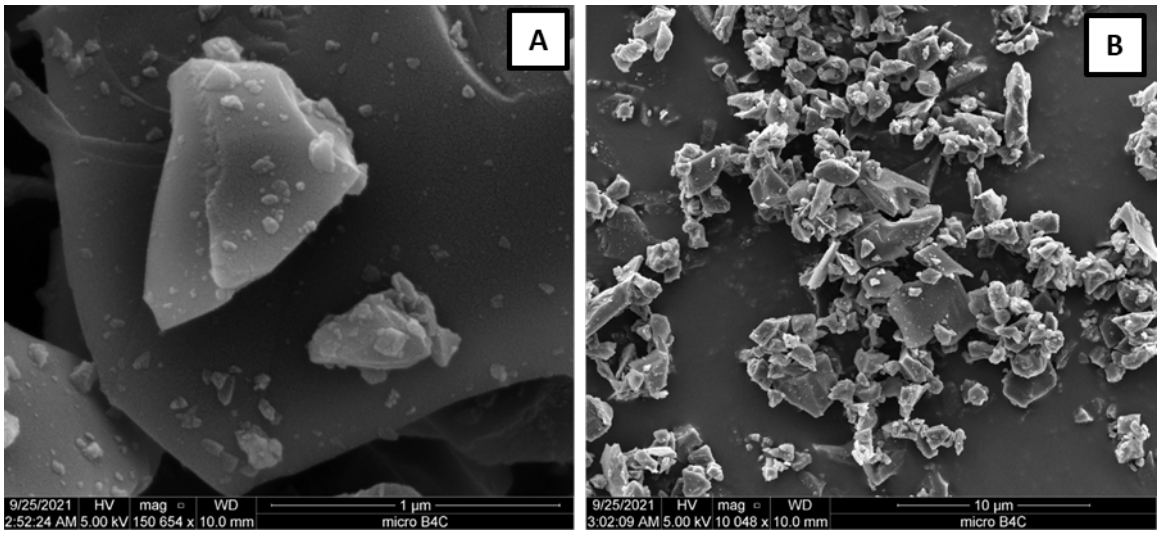

Figure 10. SEM images of a) single boron carbide particle, and b) boron carbide powder as received from U.S. Research Nanomaterial Inc

B. HIGH ENERGY BALL MILLING

All powders in this study were mixed using high-energy ball milling (HEBM). HEBM is a dry process using a milling media where particles are bombarded by collisions with the milling media. These collisions cause particles to be welded together and fractured in a repetitive process [33]. HEBM also breaks up the agglomeration of nano-reinforcements and disperses them well in the powders. The ball mill used was an SPEX SamplePrep Mixer/Mill 8000D [34]. Figure 11 shows that by increasing the ball-to-powder ratio (BPR) and by increasing the number of cycles, particles become larger and flattened [35]. For cold spray, particles need to be small and generally uniform in size and dimensions. Large flake-like particles will not spray well or adhere to the substrate well. For this reason, ball-to-powder ratios were tested and examined to determine the best fit for the aluminum powders and nano-reinforcements used in this study.

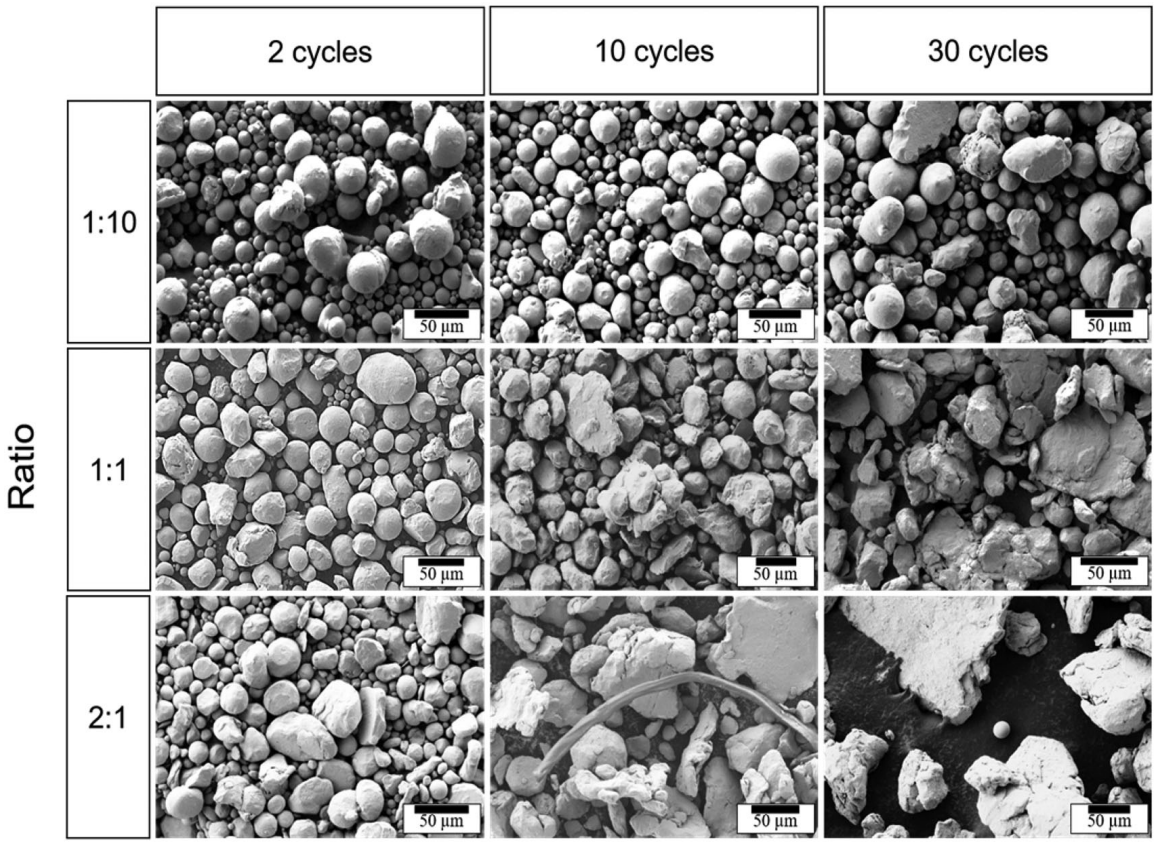

Figure 11. Example of effects of HEBM on 316L stainless steel powders. Source [35].

For the compositions in this experiment, a ball-to-powder ratio (BPR) of 1:5 was chosen after attempting a series of increasing ratios of 1:10, 1:5, 1:1, 2:1, and 5:1. The 1:10 BPR was insufficient in breaking up agglomerated GNPs in the composite powders as seen in Figure 12.

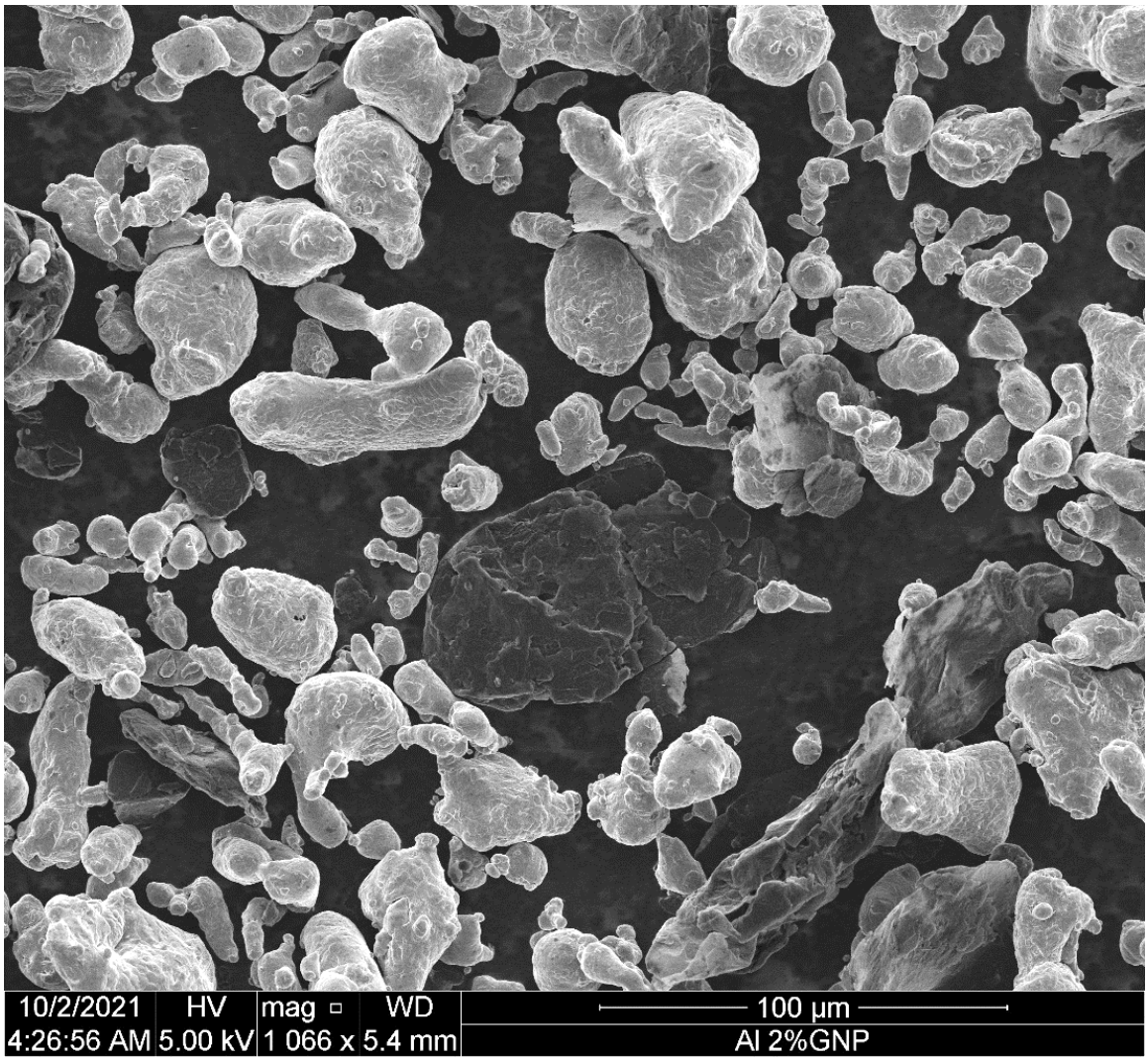

Figure 12. Inadequate dispersion of GNPs using 1:10 BPR

When using the 2:1 and 5:1 BPR, the milled powders became too deformed. The particles were large and flat, and the GNPs have broken apart and are small as seen in Figure 13. Particles of this size and geometry are not desirable for the cold spray process.

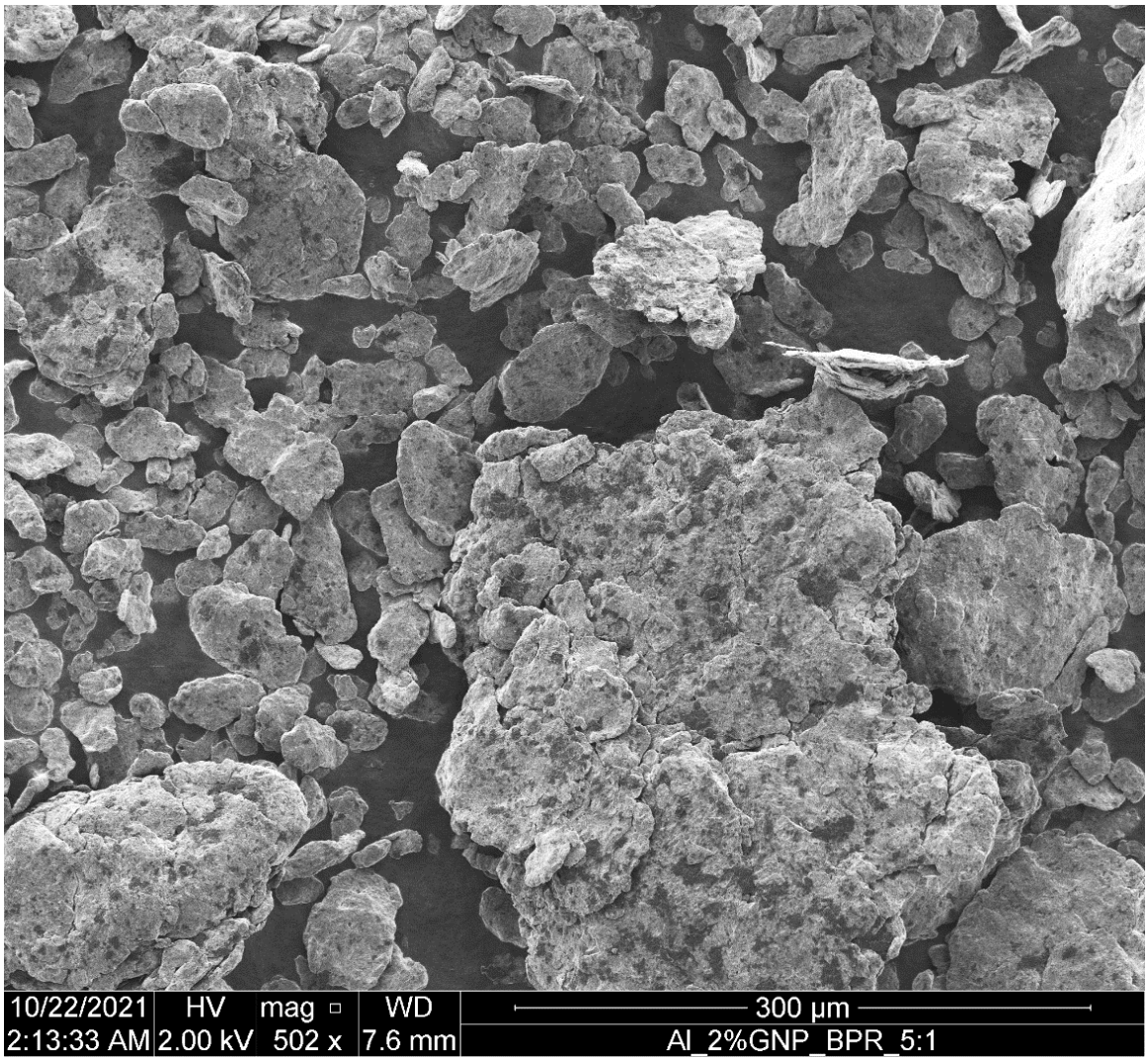

Figure 13. Large flat particles obtained using 5:1 BPR

The final parameters for ball milling are recorded in Table 4. The run and rest times chosen for this experiment were used from a previous study by Ansell et al. [35]. This period of rest between run times gives the powder a chance to cool down, thus preventing melting or overly flattening the particles.

Table 4. HEBM testing parameters

Total Mass of Powder	Milling Media	Containment	BPR	Run Rest Cycle
50 g	3 mm SS balls	Stainless Steel Jar	1:5	2 min on 5 min rest

C. COLD SPRAYING

All mixed powders were left in a 75˚C oven overnight to remove any remaining moisture before spraying. All samples were sprayed using a Centerline Supersonic Spray Technologies division (SST) Series P Spray Machine, with an X-Feeder, and a Series P Automatic Spray Gun. The machine settings for all coatings were recorded in Table 5. Initial samples received a single layer coating, but after wear experiments, it was determined coatings were too thin, and henceforth samples with 2 layers were used instead. The second layer was added to ensure wear testing did not go all the way through the coatings.

The surface of each substrate was roughened before spraying using an Eastwood Benchtop Blast Cabinet with aluminum oxide (Al_2O_3) blast media. Roughening the surface of the substrate increases the adhesion of the first layer of the coating. This increase is due to better mechanical interlocking between the particles and the substrate surface. A smooth substrate causes more particles to bounce off until a thin layer of particles begins to build up. The hardness of the substrate can affect the ability of particles to adhere to the surface. If the substrate has a significantly higher hardness than the particles, they are more likely to bounce off. For this reason, the Al-6061 substrate was chosen for these tests. All powders were sprayed onto Al-6061 substrates measuring 220 x 18 x 3 mm.

Table 5. Cold spray testing parameters

Gas	Feed Rate	Nozzle Temperature	Gas Pressure	
Nitrogen	5% (4.28 g/min)	425˚C	1.65 MPa (240 psi)	
Traverse Speed	**Stand-off Distance**	**Line Spacing**	**Nozzle Material**	**Number of Layers**
40 mm/s	12.7 mm (0.5 in)	1 mm	WC-Co	2

D. HEAT TREATMENT

To determine the optimal heat treatment parameters for this study, several similar studies were reviewed. In 2013, Pitchuka et al. [36], [37] investigated the wear behavior of cold-sprayed aluminum amorphous/nanocrystalline coatings. Using an Al-6061 substrate, Al amorphous/nanocrystalline alloy powder (Al–4.4Y–4.3Ni–0.9Co–0.35Sc (at.%)) was deposited via the cold spray method. These coatings were then heat-treated for 1 hr at 300˚C. The heat-treated coatings had a decreased porosity of 0.5% compared to 2% in the as-sprayed coatings. The heat-treated coatings exhibited a slightly higher hardness attributed to the densification of the coating, particle crystallization, and the formation of hard intermetallic phases. These phases were confirmed by x-ray diffraction. Due to the nucleation of these intermetallic phases, which reduces the inter-atomic spacing, the elastic modulus of the heat-treated coatings increased by 33% [37]. Investigation of further material properties revealed that scratch resistance improved after the treatment. This improvement was attributed to the densification of the coatings and increased hardness. Wear testing showed the as-sprayed coatings had a 68% higher wear volume loss, and the heat-treated coatings exhibited a smoother wear surface and reduced signs of plastic deformation. The heat-treated coatings also exhibited a more dense and smooth fracture surface attributed to a stronger intersplat region [36].

In 2021, Bobzin et al. studied the best time and temperature combinations for heat treatment of cold-sprayed coatings to increase cohesive strength within the coatings. This study focused on Al99.0 and AA7075 coatings. These coatings were ground off their substrates and heat-treated as free-standing coatings at 400°C for various dwell times [38]. These temperature and dwell time combinations were compared via hardness testing as shown in Figure 14.

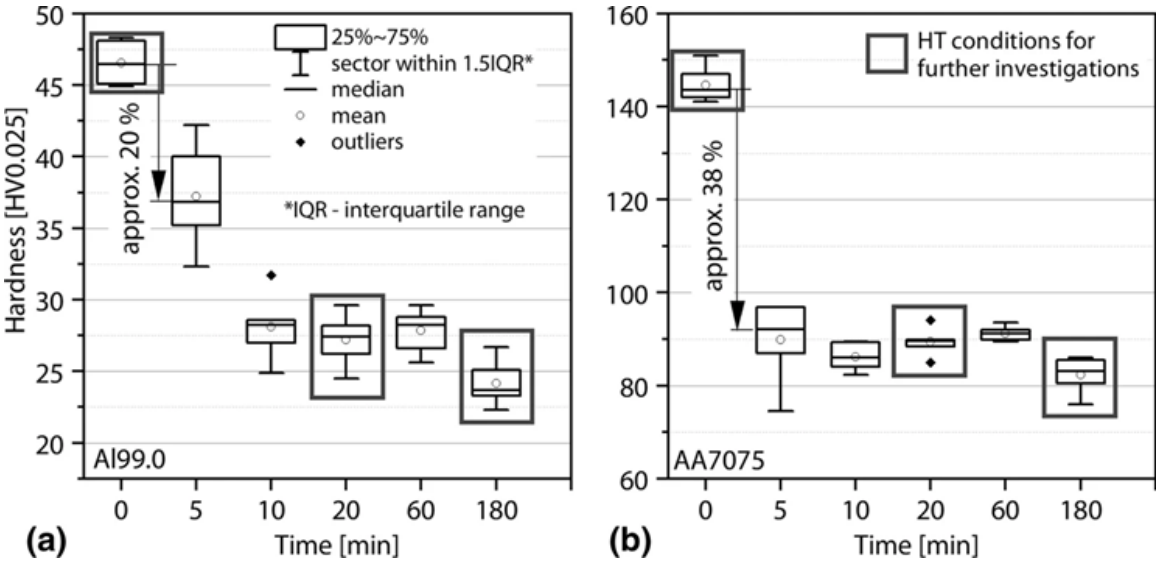

Figure 14. Effects of heat treatments on coating hardness T = 400 °C for a) Al99.0 coating and b) AA7075 coating. Source: [38].

It was noted that many precipitates formed along grain boundaries in treatments up to 20 minutes. Extended heat treatment caused coarsening of the precipitates but did not promote the nucleation of new grains [38]. The effects of these grain sizes can be seen in Figure 15 as the samples transitioned from being more brittle to more ductile depending on dwell time.

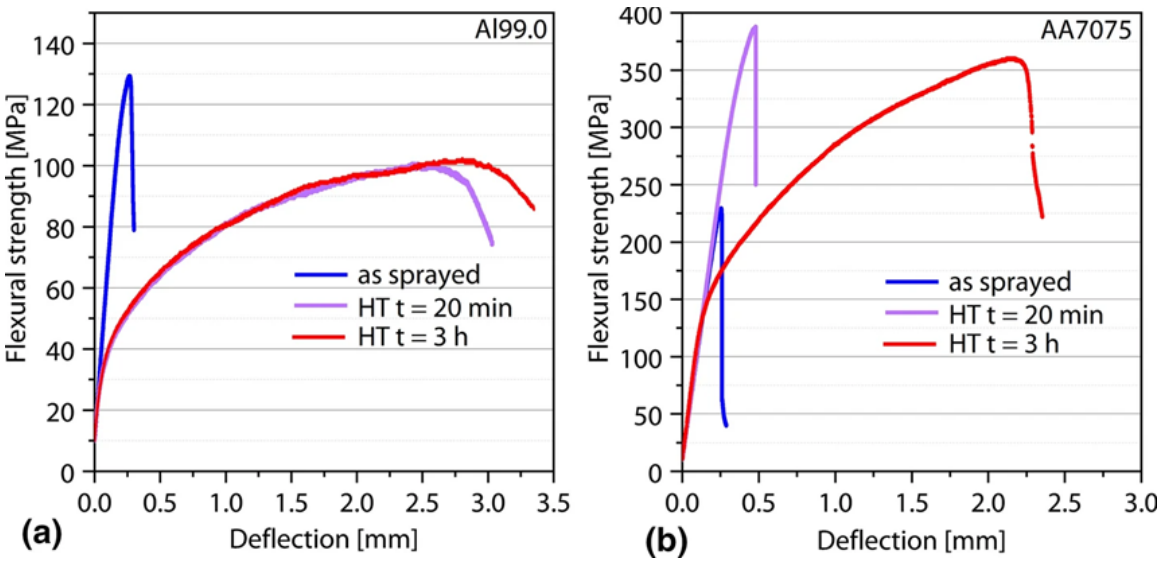

Figure 15. Bending stress and deflection curves for heat-treated coatings at T = 400◦C for a) Al99.0 coating and b) AA7075 coating. Source: [38].

This study concluded that a purely brittle fracture occurs for both coatings in the as-sprayed condition and that the fracture occurs along the splat boundaries. There is a transition to mixed fracture during the heat treatment due to softening of the microstructure. For the Al99.0 coating, there was a significant increase in ductility at T=400˚C for t_{HT} = 20 min [38].

In 2014, Huang et al. studied the effects of heat treatment on the mechanical properties of cold-sprayed coatings for several materials including Al. This study heat-treated all coatings for 4 hours under different temperatures. The graphs in Figure 16 show the tensile properties for the Al sample [25].

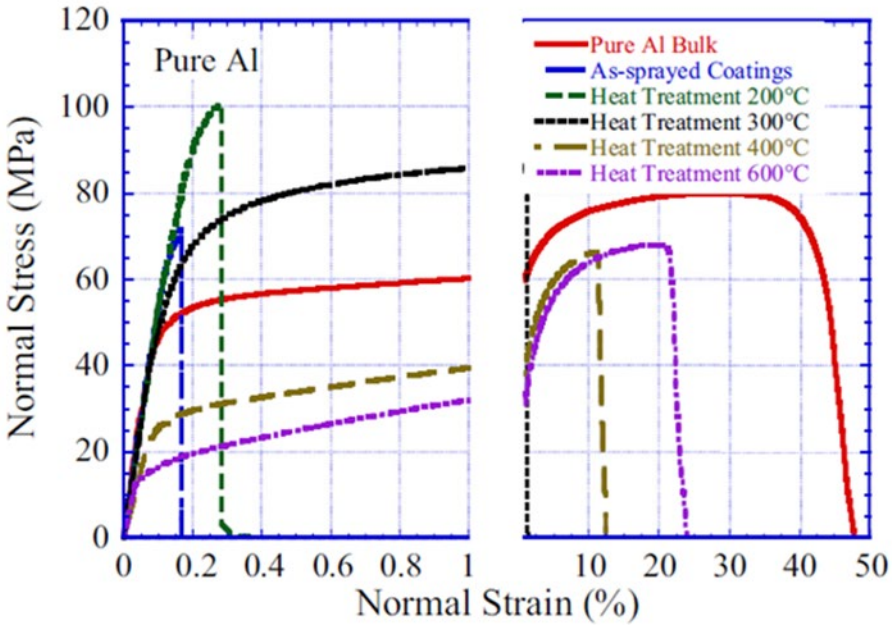

Figure 16. Tensile properties of cold-sprayed Al Coating with various heat treatment temperatures. Source: [25].

This study also looked at fracture surfaces under SEM as shown in Figure 17. It was determined that the as-sprayed coating experienced de-cohesive rupture because the cohesion of the particles was poor. For the 300°C heat-treated coating, particles were more cohesive but still fractured mostly at the splat boundaries. The 600°C heat-treated sample had dimples on the fracture surface, denoting a more cohesive failure.

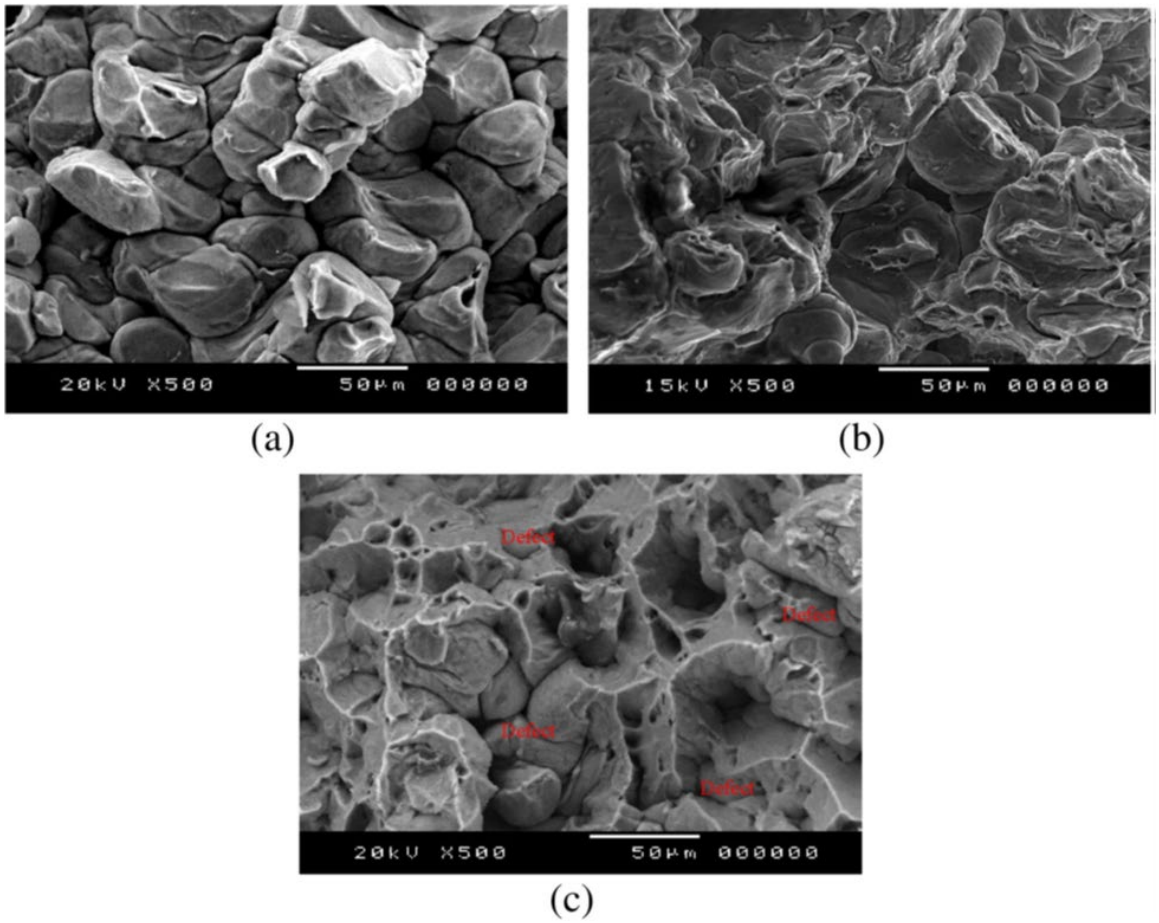

Figure 17. Fracture surface of as-sprayed Al coatings. a) heat-treated at 300°C, b) and 600°C, c). Source: [25].

After reviewing the current literature about heat treatments of aluminum cold spray coatings and aluminum composites, parameters for heat treatments for this study were decided. Heat treatment parameters for this study are recorded in Table 6. All heat treatment was conducted using a 1–2" 1250°C Compact Split Tube Furnace from MTI Corporation model OTF-1200X. These parameters were determined to be sufficient to begin diffusion of the coatings and strengthen the interfaces between particles and between the coating and substrate while staying below the recrystallization temperature for Al. The heat treatment was conducted under a constant flow of argon, which pressurized the tube furnace to 0.04 MPa. The sample was set on an Al_2O_3 crucible to avoid touching the walls of the furnace. The heating element was set to ramp up to the maximum temperature of 400°C over 20 minutes. The sample was then left to dwell at this temperature

for 60 minutes, then the machine was turned off. Cooling of the sample was also allowed to happen under constant argon flow until the temperature was below 150˚C at which point the sample was removed from the tube furnace.

Table 6. Heat treatment testing parameters

Gas	Ramp-up Time	Treatment Temperature	Dwell Time
Argon	20 min	400˚C	60 min

E. CHARACTERIZATION

1. Hardness Tests

A series of 15 micro-indentation hardness tests were conducted on each cross-section. All micro-hardness measurements were conducted using a Struers DuraScan Vickers hardness tester. The indentation setting used Vickers HV 0.05. Careful attention was made to ensure all tests were on areas of the cross-section within the coating, not on pores or scratches.

A series of 50 nano-indentation hardness tests were conducted on each cross-section. All nano-hardness measurements were conducted using an Agilent Technologies Nano Indenter G200 using the same parameters for each batch of 50 tests as recorded in Table 7.

Table 7. Nano indenter testing parameters

Max Load [gf]	Peak Hold Time	Time to Load / Unload	Poisson's Ratio
0.200 gf (1.961 mN)	3 s	10 s	0.330 [39]

Nanoindentation tests the hardness of a sample and calculates the elastic modulus using the Oliver-Pharr method [40], [41]. This method was first introduced in 1992 and uses the load and displacement curves to calculate hardness and elastic modulus. One of the key improvements in this method was the new understanding that the loading and unloading curves on the load-displacement plot were not linear. This method accounts for this curvature and uses it to justify the determination of the depth and shape of the indenter to obtain accurate values for hardness and elastic modulus [40], [41]. For nanoindentations in this study, 0.200 gf (1.961 mN) was used as the maximum load. Calculation of the elastic modulus used the poisons ratio for pure Al of 0.330 [39] and the percent unload for the stiffness calculation of 50.00%. Each nanoindentation took 10 seconds to reach the max load, was held at the maximum load for 3 seconds, and was unloaded over 10 seconds. To choose testing points, an array was not used because the sample surface was not homogeneous due to splat boundaries. All 50 testing points were chosen by hand to avoid scratches from the polishing process, pores in the coating and splat boundaries.

2. Adhesion Testing

A series of five adhesion tests were conducted on the heat-treated coatings. Each test used an Elcometer 510 Model T, an automatic adhesion tester. This form of adhesion test adheres to the ASTM specification C633. The parameters for adhesion tests are recorded in Table 8. Each adhesion test used Master Bond EP15ND-2, a one-component, heat-curing epoxy with a tensile strength of over 82.7 MPa (12,000 psi). The epoxy was cured according to the manufacturer's specification of 300–350°C for 60–90 min in a lab oven. This epoxy was used to ensure failure occurred either within the coating (cohesive failure) or at the substrate boundary (delamination / adhesive failure), not in the epoxy (glue failure). All tests gave a reading for the maximum stress and each test failure mode was determined by visual examination. The coating can either fail along the substrate-coating interface, inside the coating, or at the epoxy-coating interface, which is inconclusive. Determining failure modes helps to identify the test as reliable and accurate.

Table 8. Adhesion testing parameters

Dollie Size	Pull Rate	Epoxy
10 mm	150 psi/s	Master Bond EP15ND-2 (>12,000 psi)

3. Wear Testing

A series of six dry sliding ball-on-disk wear tests were conducted on each coating sample. All final samples tested consisted of two layers of cold spray coating. The wear tests were conducted after heat treating the samples, and took place on the surface of the coating, not on a mounted cross-section. The testing parameters for the wear tests are recorded in Table 9. All wear tests were conducted using a Nanovea T50, a standard modular tribometer. The mass of the sample was measured before and after each test to measure mass loss. The counter surface used for this wear test was a 3 mm stainless steel 304 ball. Counter surface balls and wear debris were collected for possible subsequent analysis. The first samples, which had only one layer of coating, underwent wear testing without first being heat treated. These samples seemed to wear beyond the depth of the coating, so a second layer was decided on before creating more samples. These wear tests also recorded the depth of the encoder and coefficient of friction in real-time. The data collection rate was set to 20 data points per second for both the coefficient of friction and the encoder depth. The coefficient of friction is measured using a lateral force sensor during the test. The load for each test was set to 3N, the wear tracks were 6 mm in diameter, and the sample was rotated at 100 RPM. By the end of each test, the total sliding distance was 113.2 m.

Table 9. Wear testing parameters

Test Type	Load	RPM	Duration	Wear Track Diameter	Total Sliding Distance	Counter Surface
Orbital: ball-on-disc	3 N	100	60 min	6 mm	113.1 m	Ball: 3 mm SS 304

4. Sample Preparation

Samples were made for each of the sprayed coatings by cutting perpendicular to the coating and cold mounting in epoxy. Adhesion tests were also cross-sectioned and mounted for polishing. The epoxy used was Stuers ClaroCit, a fast-curing clear acrylic cold mounting resin. Each mount was made according to the manufacturer's instructions. These sample mounts were ground flat and hand polished to expose details in the coatings by obtaining a mirror finish, free of large scratches. Table 10 shows the general process for grinding and polishing steps. Timeframes were estimated, but each step was complete when scratches from the previous step were no longer visible under the microscope. All grinding and polishing disks were 12-inch in diameter.

Table 10. Grinding and polishing steps

Step	Grit/Solution	Time [min]	RPM
1	320	5-10	350
2	600	5-10	350
3	1200	10-15	450
6	6 µm Diamond	5-10	350
7	3 µm Diamond	5-10	350
8	1 µm Diamond	5-10	350

After samples were polished to a mirror finish, they were etched to reveal the splat boundaries and to see the microstructure better in the SEM. The etching process used Keller's reagent (a mixture of 2.5 vol.% nitric acid, 1.5 vol.% hydrochloric acid, and 1.0 vol% hydrofluoric acid in water) to corrode just the splat and grain boundaries [42]. The reagent was applied using a small cotton swab and was rubbed slightly, then left for no longer than 30 seconds before being rinsed off with water.

5. Microscopy Preparation

The original powder samples that were imaged before cold spraying were applied to a double-sided carbon tape and sputtered only if it contained μB_4C. All of the samples that were mounted in resin or containing μB_4C can cause issues when imaging in the scanning electron microscope due to a lack of conductivity. These effects will lead to poor imaging but can be avoided by sputtering the samples with a conductive material. All resin-mounted samples and all samples containing μB_4C were sputtered with either palladium or gold for 30 seconds. All sputtering was done under an argon vacuum in a Cressington Sputter Coater 208HR while samples were spinning. Copper tape was often applied to give extra conductivity to metals mounted in resin before sputtering. Wear tracks not containing μB_4C were imaged without sputtering. All wear tracks were imaged as received from the wear tester and were taped to the SEM stage using copper tape. The SEMs used in this experiment were a Zeiss Neon 40 SEM, and the Thermo-Fisher Scientific Inspect F50 SEM.

6. Porosity Measurements

To understand how the nanoparticulate reinforcements interact with the porosity of the coatings, porosity measurements were taken from the polished cross-sections of each sample. As discussed earlier, porosity is the percentage of pores within the coating. These pores are formed when cold-sprayed particles do not form a perfectly solid coating. Then heat treatment causes these pores to merge and form larger pores. High porosity in a cold-sprayed coating is generally an undesirable trait. Pores act as starting points for fracture and can weaken the overall strength of the coating. This was shown in the schematic in Figure 6 in Chapter II. Measurement of porosity for each sample was conducted on the

cross-section images received from the SEM. These measurements were conducted using ImageJ where the photos were converted to binary, black and white regions denoting pores and Al particles. ImageJ would then add together all the white area (coating) and black area (pores) and calculate a percent porosity.

THIS PAGE INTENTIONALLY LEFT BLANK

IV. RESULTS AND DISCUSSION

A. COATING DEPOSITION AND MICROSTRUCTURAL CHARACTERIZATION

The first observation between the compositions was the quality and ease of spraying. The thickness and evenness of the coatings are a quick and easy way to see the quality of the sprayed coating. A bad coating may have ridges or be too thin in some places as shown in Figure 18. This failed coating was due to clogging of the spray nozzle which was later corrected by using a polymer nozzle.

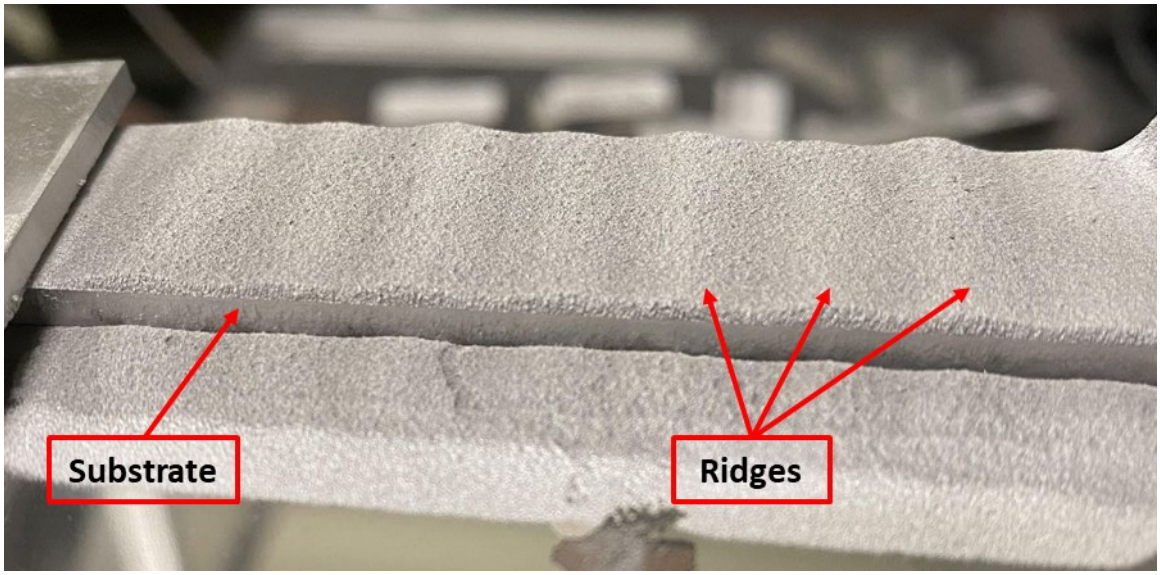

Figure 18. Failed spray due to nozzle clogging

Average coating thickness was measured from the polished cross-sections and was recorded in Table 11. Here, each composition can be compared to the control group of pure Al. The addition of any reinforcements generally decreased the thickness of the coatings, but specifically for GNPs, the coating thickness suffered. This is likely due to the high aspect ratio of the 2D nanoparticle causing issues with powder flow. A particle with a high aspect ratio has a large surface area and very little mass, which causes the particle to tend to agglomerate and cause clogging, or adhere to the inside of the feed lines. This type of

particle also causes issues in-flight due to particles being blown away by the high gas speeds. Lessening the vol% of GNP for the Al-GNP/μB_4C allowed for the coating to be closer to the control in thickness. This could also be due to the μB_4C particles helping to break up the agglomerated GNPs. The areas for each region were measured and provided as a ratio of pore area to total area. The porosity for each coating sample is given in Table 12.

Table 11. Average coating thickness

Composition	Range	Average Thickness [μm]	Standard Deviation [μm]
Al Only	462-694	561	47.4
Al-GNP	191-347	279	33.2
Al-μB_4C	341-463	412	24.7
Al-GNP/μB_4C	440-617	541	36.1

Table 12. Porosity of coatings

Composition	Porosity [%]	SD
Al Only	5.19	2.95
Al-GNP	2.88	1.44
Al-μB_4C	0.86	0.73
Al-GNP/μB_4C	1.04	0.82

The pure aluminum coating is significantly more porous than any of the reinforced coatings. However, all of the reinforced coatings have similar porosity that is too close to accurately define one as more porous than the others. Each composition is shown

in Figure 19 as cross-sections, where it is easy to see the porosity of the coatings and the thickness compared to the pure Al coating.

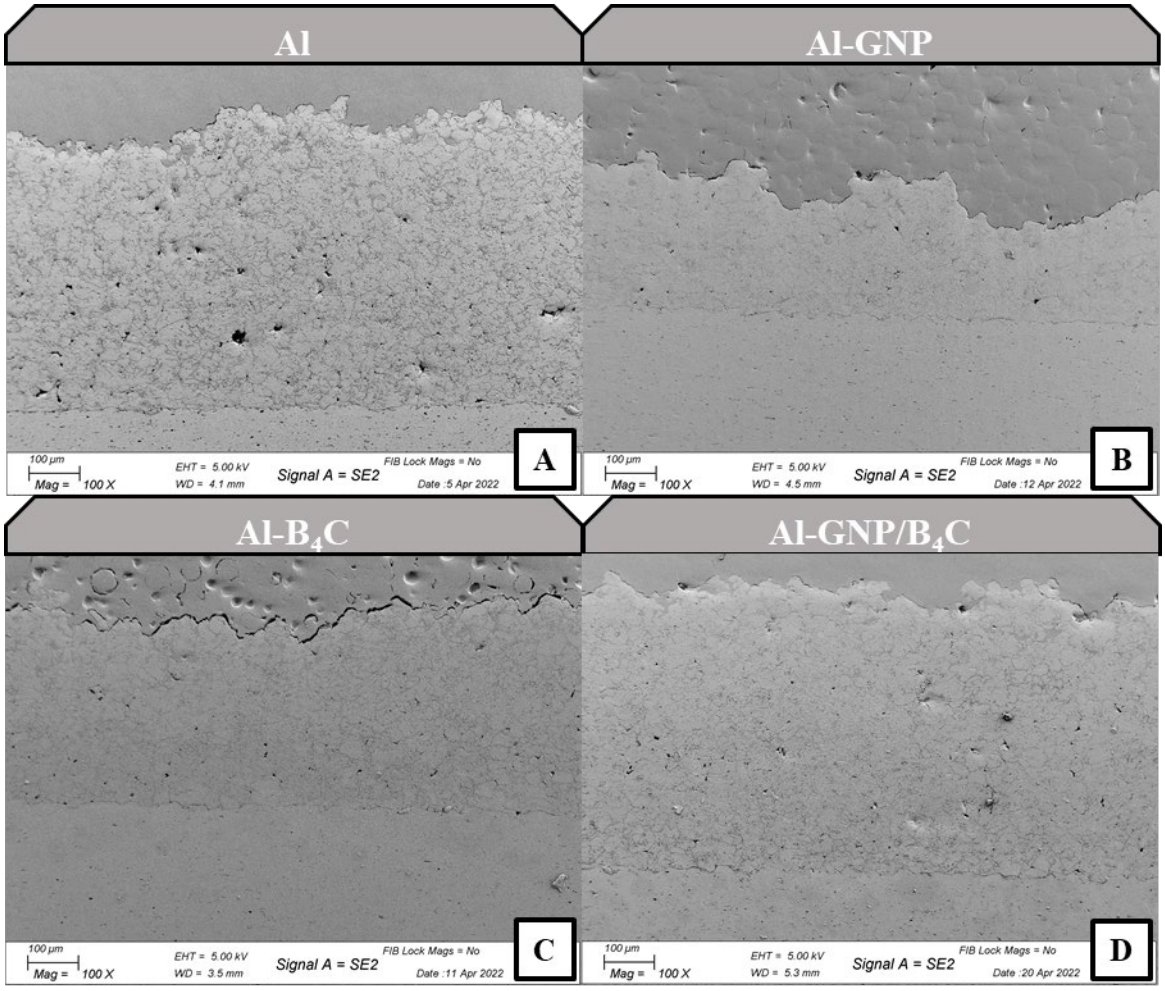

Figure 19. Coating cross-sections after heat treatment of a) Al, b) Al-GNP, c) Al-µB4C, and d) Al-GNP/µB4C

The pure aluminum coatings are free from any particle reinforcements as shown in Figure 20. Figure 20a shows splat boundaries between a few particles which appear as a black line. Figure 20b shows what a clean splat boundary looks like; there are no reinforcing particles wedged in between.

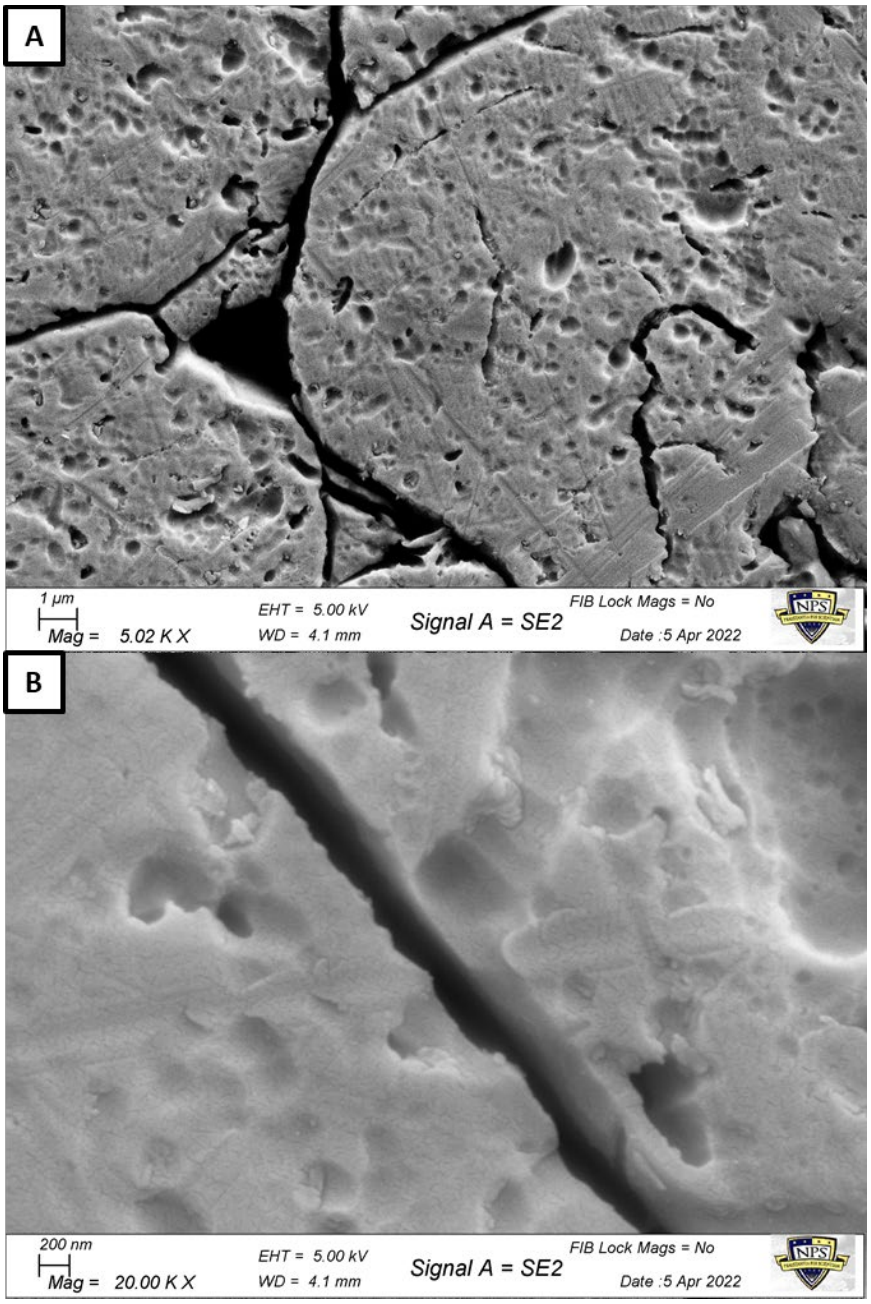

Figure 20. Al coating without the presence of reinforcements showing an a) intersplat region, and a b) high magnification splat boundary

Figures 21 and 22 were taken to show proof of reinforcements in the sprayed coatings. These figures show how the reinforcement particles often appear in the Al coatings. Figure 21a shows the Al-GNP composition with exposed GNPs near the edge of a splat. Figure 21b shows layers of GNPs that form along the splat boundaries, bridging

the gap between Al particles. These particles are confirmed as GNPs due to their two-dimensional, plate-like shapes. If the GNP is only a couple of layers thick, it can appear electron transparent in the SEM. These platelets are often several layers thick as seen in Figure 21a, and these layers are often folded or kinked back over themselves. This kinking can be seen as straight lines on the GNP overlapping each other, or as a crinkled thin sheet.

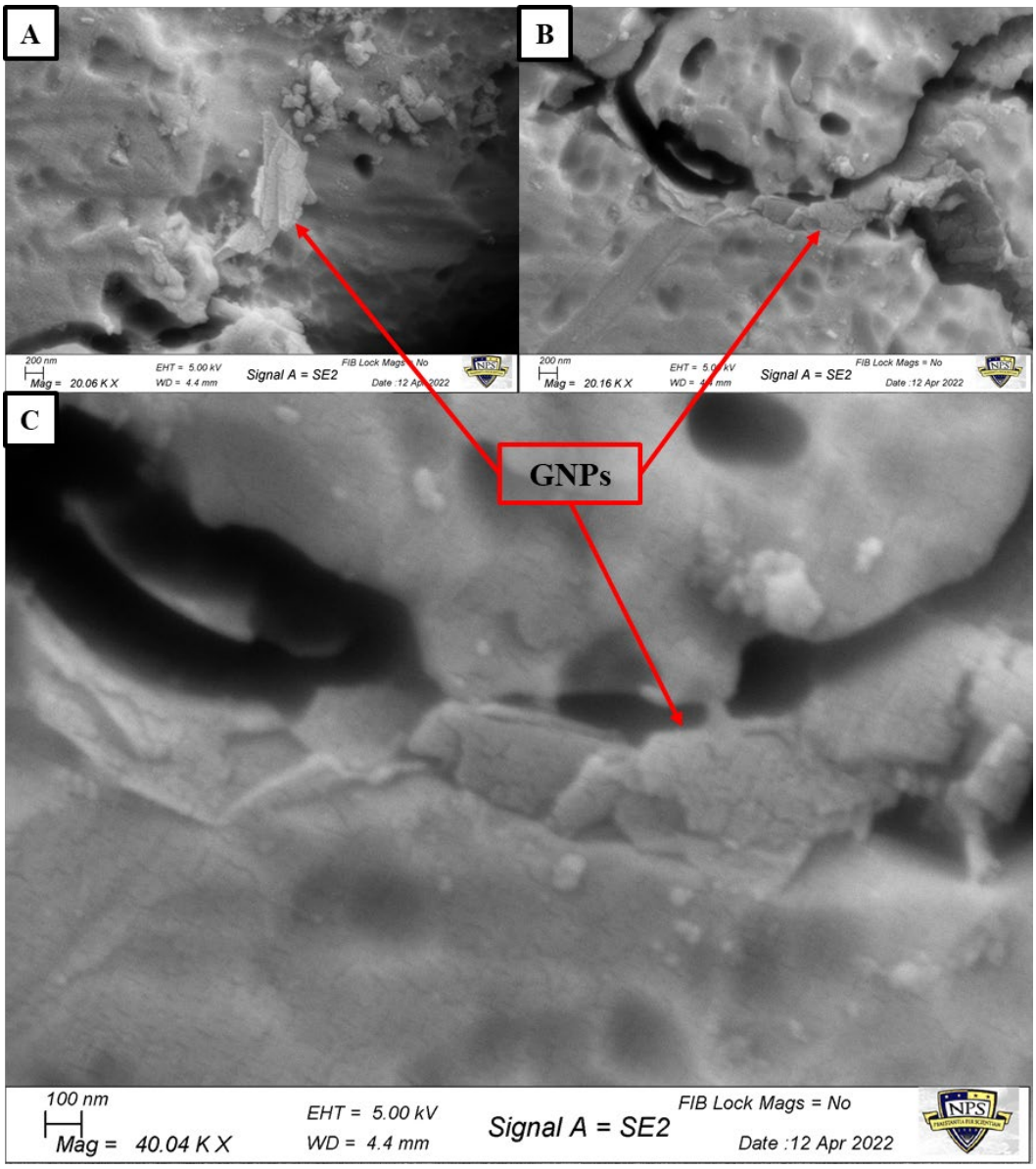

Figure 21. Al-GNP coating showing the presence of GNPs at the a) surface of an Al particle, and b) in an intersplat region, and c) again at higher magnification

The presence of μB4C particles is confirmed in both the Al-μB4C and Al-GNP/μB4C samples as shown in Figure 22. The μB4C particles appear in the splat boundaries and are usually no larger than 1 μm due to breaking apart during milling or cold spraying. These particles can be confirmed as μB4C particles by looking at their geometry under the SEM. The μB4C particles used in this experiment have sharp angles and flat edges, and since μB4C is nonconductive, μB4C particles will often show up brighter than the surrounding Al as shown in Figure 10. While imaging in the SEM, the presence of μB4C was often noted by charging or the appearance of horizontal lines across the screen.

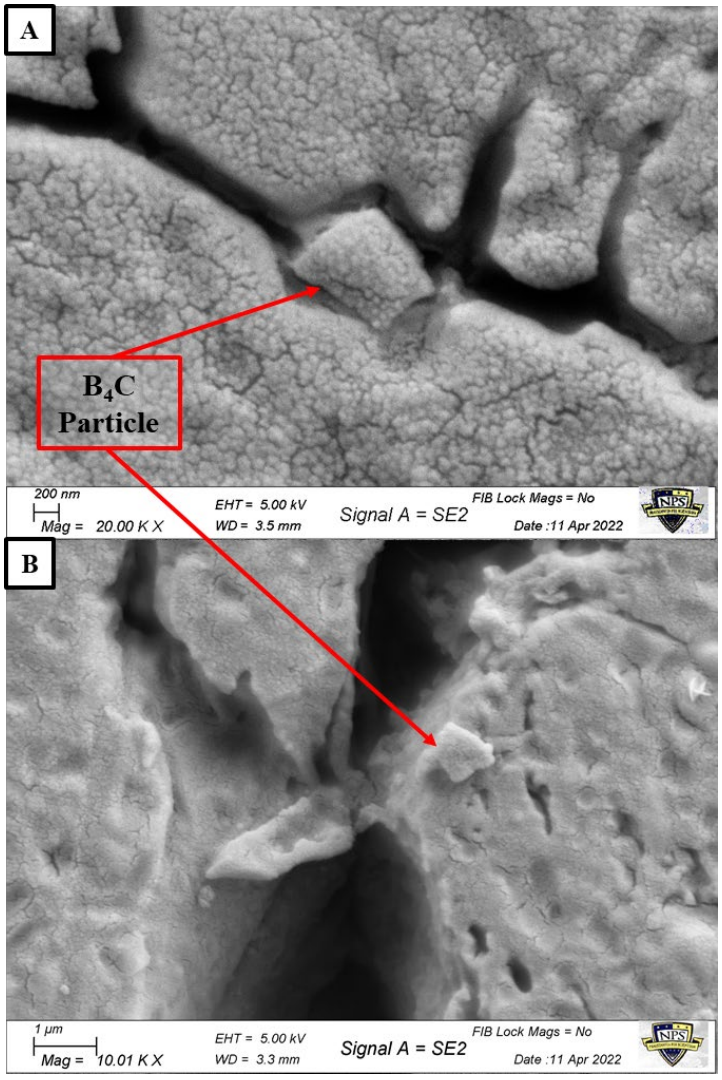

Figure 22. Al-μB4C coating showing the presence of μB4C particles a) in the intersplat region, and b) near a crack

Energy-dispersive X-ray spectroscopy, or EDS, was conducted on the Al-GNP/μB4C coating on a location that was believed to contain μB4C particles. Using the particle mapping feature, x-rays released during the scan, correlating to atoms of boron, carbon, and aluminum were mapped and shown in Figure 23. This scan shows that the particles identified as GNPs and μB4C particles in Figure 23a were correctly assumed due to the high concentration of corresponding gammas shown in these areas in Figure 23b and Figure 23c. Figure 24 shows another EDS of μB4C particles within the same coating.

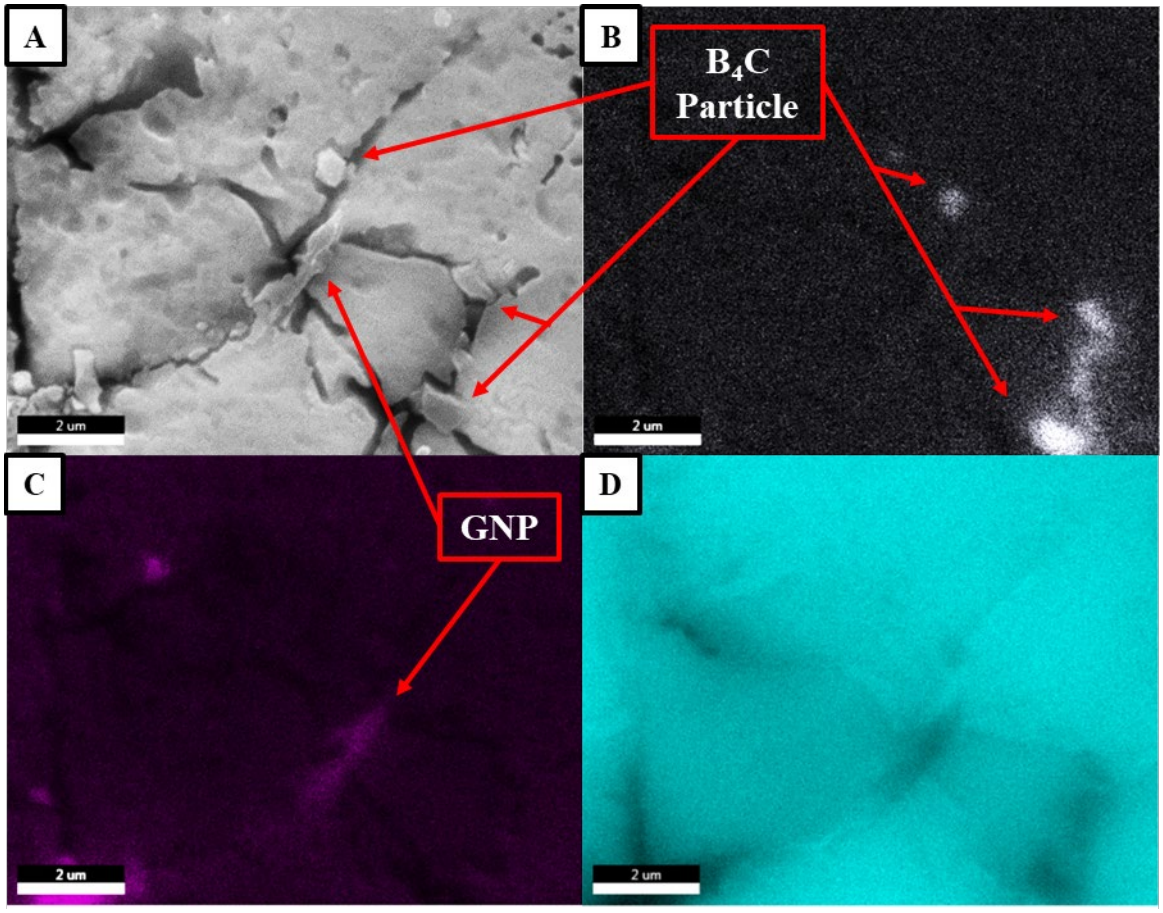

Figure 23. EDS of Al-GNP/μB4C coating showing presence of GNPs and μB4C particles. a) analyzed region, and map showing concentration of b) boron, c) carbon, d) aluminum

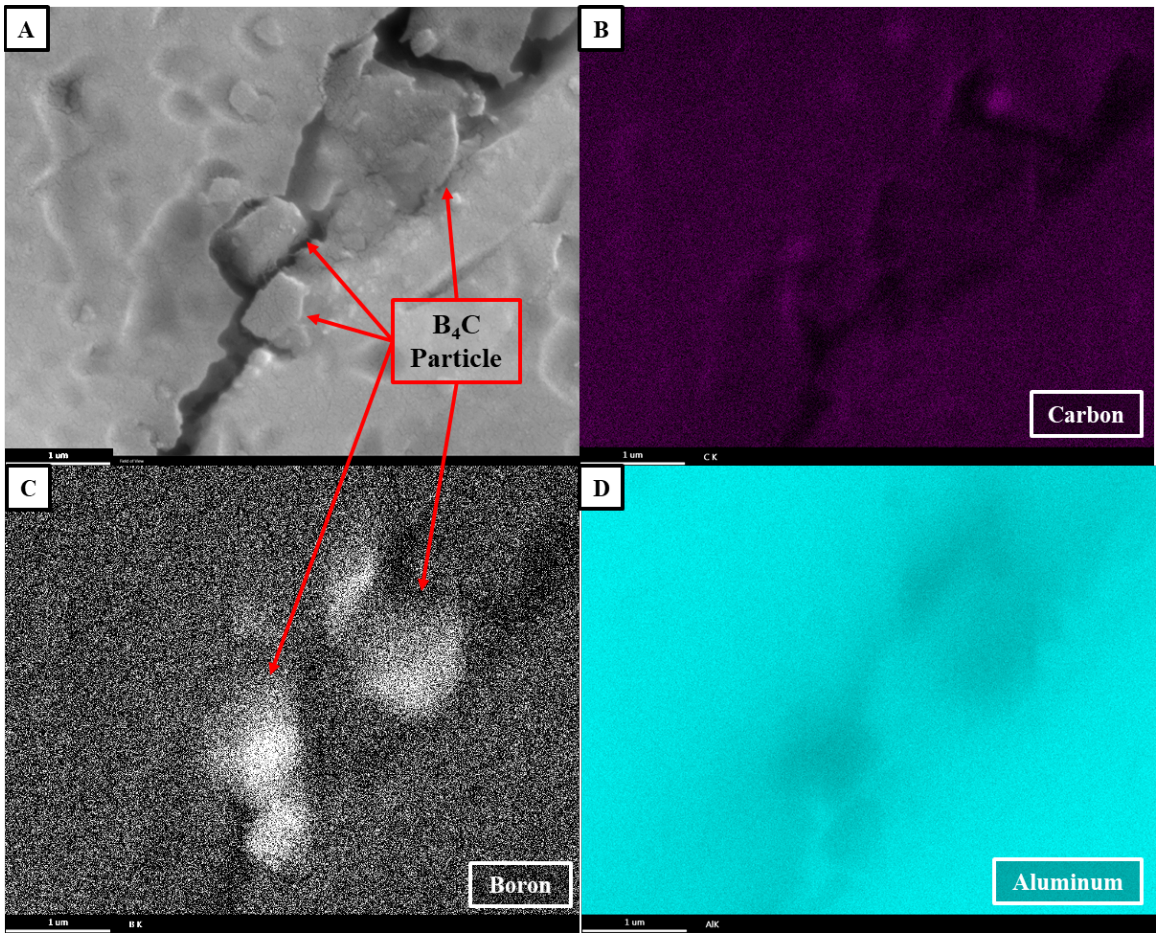

Figure 24. EDS of Al-GNP/µB4C coating showing presence of µB4C particles a) analyzed region, and map showing concentration of b) carbon, c) boron, and d) aluminum

Before spraying, the Al powder and reinforcement particles for each composition were ball milled together to mix the reinforcements and break up any agglomeration. The particles then looked like the particles shown in Figure 25. This schematic shows the effect of cold spraying on the reinforcements. The reinforcement particles began adhering to the surface of the Al particles on all sides. After spraying the Al particles, they deformed into splats stacked on top of one another. For the GNPs, this process caused most GNPs to align along the horizontal sections of the splat boundaries. The µB4C was similar, as the particles became wedged in splat boundaries, primarily along the horizontal sections. The coatings are now composites with reinforcement particles evenly distributed among the spat boundaries.

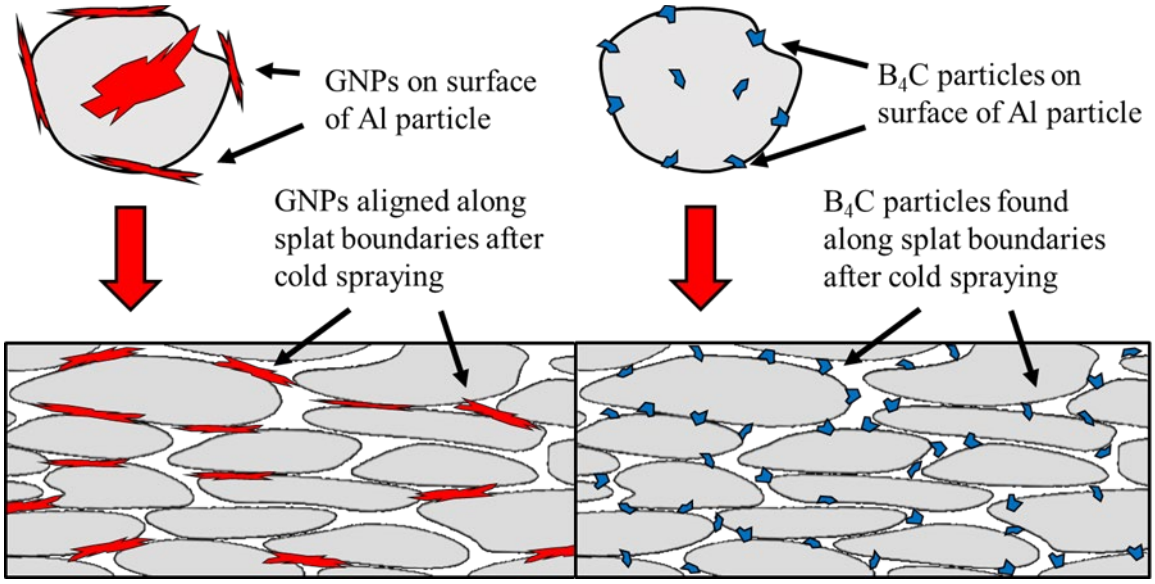

Figure 25. Effect of cold spraying on GNP and µB4C orientation

B. HARDNESS

Hardness testing is one of the most direct ways of comparing the strength of materials. Results from the micro-hardness tests are shown in Figure 26 where each of the 15 tests was averaged together. All the reinforced coatings experienced a significant increase in hardness by at least 47% with the Al-GNP coating at the highest with a 74.7% increase in hardness. This is due to the GNPs being pinned between Al splats during heat treatment.

The most common strengthening mechanism is when the reinforcement particles inhibit dislocation motion. Since the µB_4C particles have a much higher hardness than the surrounding Al, they help to pin dislocations and prevent further deformation. The cold spray process produces a high density of dislocations in the Al particles and the presence of the reinforcements helps to increase this density. Dispersion of µB_4C particles acts as a geometrical constraint for dislocation motion, also called Orowan strengthening [43]. The reinforcement particles cause strains in the Al particles during heat treatment and coating densification. The presence of both the µB_4C particles and the GNPs increases the work hardening to the Al particles during heat treatment.

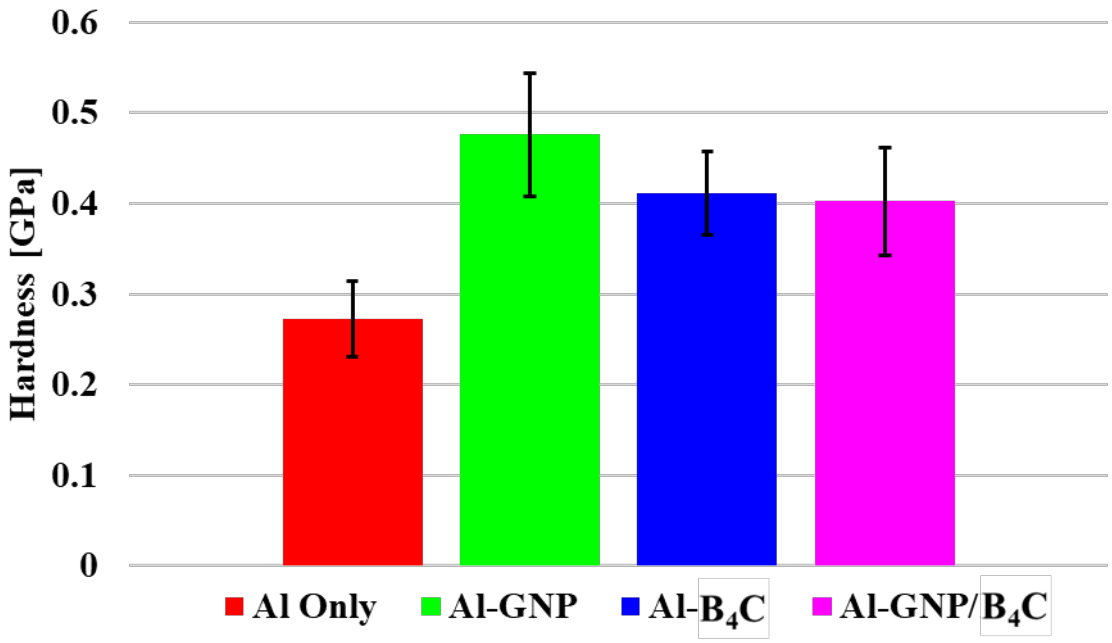

Figure 26. Vickers micro-hardness testing results

Nano-hardness measurements are used to calculate hardness and elastic modulus. Figure 27 shows a scatterplot of maximum hardness and elastic modulus for each coating composition. A box of one standard deviation for each axis was applied around an averaged data point shown in red. Some indentations failed and resulted in extremely low hardness and large elastic modulus. These points were removed as they were due to indenting on a pore in the coating. Figure 27 also shows that the grouping of tests for the Al-GNP coating was more concise about the average. This could be due to the GNPs dispersing among the coating better than μB_4C particles creating a more homogeneous coating. Similarly, for the Al-GNP/μB_4C, the presence of μB_4C particles may have helped to better disperse the GNPs as discussed in Chapter II.

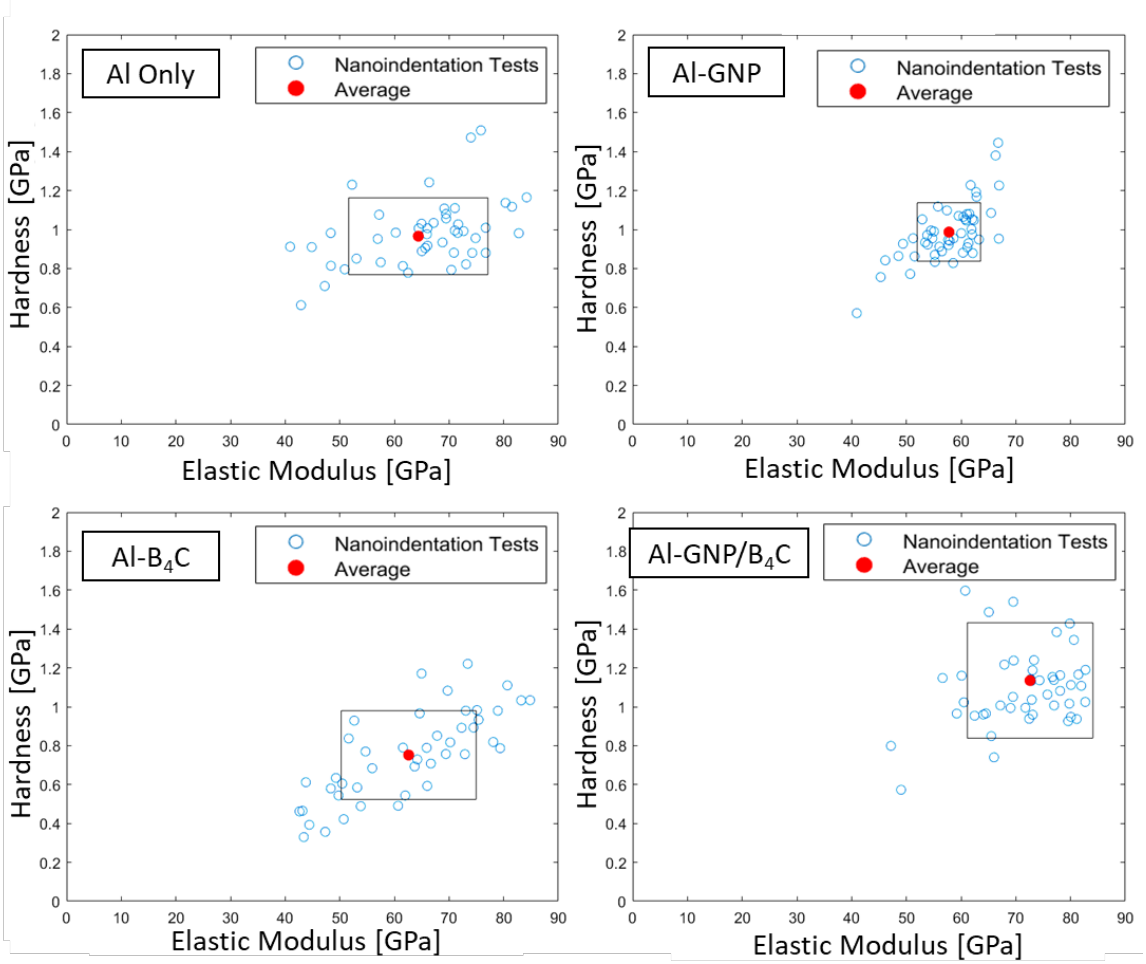

Figure 27. Scatterplots of nanoindentation tests with standard deviation boxes

Each average data point and standard deviation box from each composition was added to the same plot as seen in Figure 28. Here it is clear that the Al-GNP/μB4C coating, noted in magenta, experienced an increase in both hardness and elastic modulus. Compared to the pure Al coating, the Al-GNP/μB4C coating had a 12.8% increase in hardness and a 17.5% increase in elastic modulus. The Al-GNP coating has about the same hardness as the pure Al coating but a 10% decrease in elastic modulus. Inversely, the Al-μB4C coating has about the same elastic modulus, but with a 22% decrease in hardness. This is significant because both single-reinforcement coatings have the same or worse properties, but when added together we see improvement in both hardness and elastic modulus. This is a direct example of synergistic properties between GNPs and μB4C in an Al coating. This means

that there is some interaction between the GNPs and μB4C particles in the sprayed coating. This interaction is either a physical combination of the μB4C particles and GNPs between the spat boundaries that gives a strengthening effect, such as a load transfer mechanism, or the μB4C particles helped in the breakup of agglomerated GNPs during the milling process [31]. Both methods could cause the coating to become a higher-strength material.

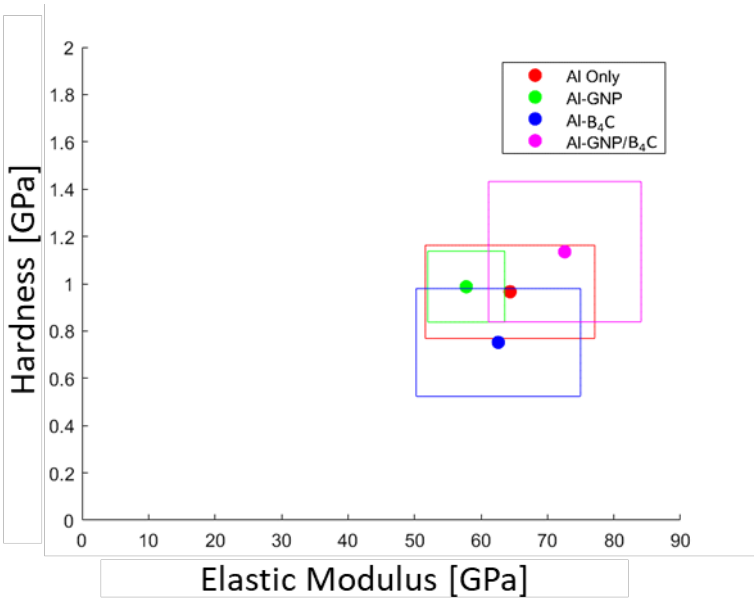

Figure 28. Nanoindentation hardness and elastic modulus at max load comparing coating types

The load and displacement data for each nanoindentation were combined as shown in Figure 29. The red line denotes the test closest to the average maximum displacement. The Al-GNP coating again experienced a more concise grouping of tests and the Al-μB4C coating had a wider range of displacement values. Both could be due to the ability of the reinforcements to disperse well in the powders during the milling process. Starting from the origin, the test begins by loading the sample until it reaches 2mN. This loading line is concave down and any samples that had a convex loading curve were removed as this is characteristic of the indenter slipping during the test. The maximum load is held for 3 seconds and then slowly unloaded. The unloading curve is used to calculate the elastic modulus and plasticity. The averages were combined into the same plot in Figure 30, where

it becomes visible that the Al-μB_4C experienced a greater displacement under identical loading. This difference is likely due to the larger range of displacements experienced by the Al-μB_4C coating.

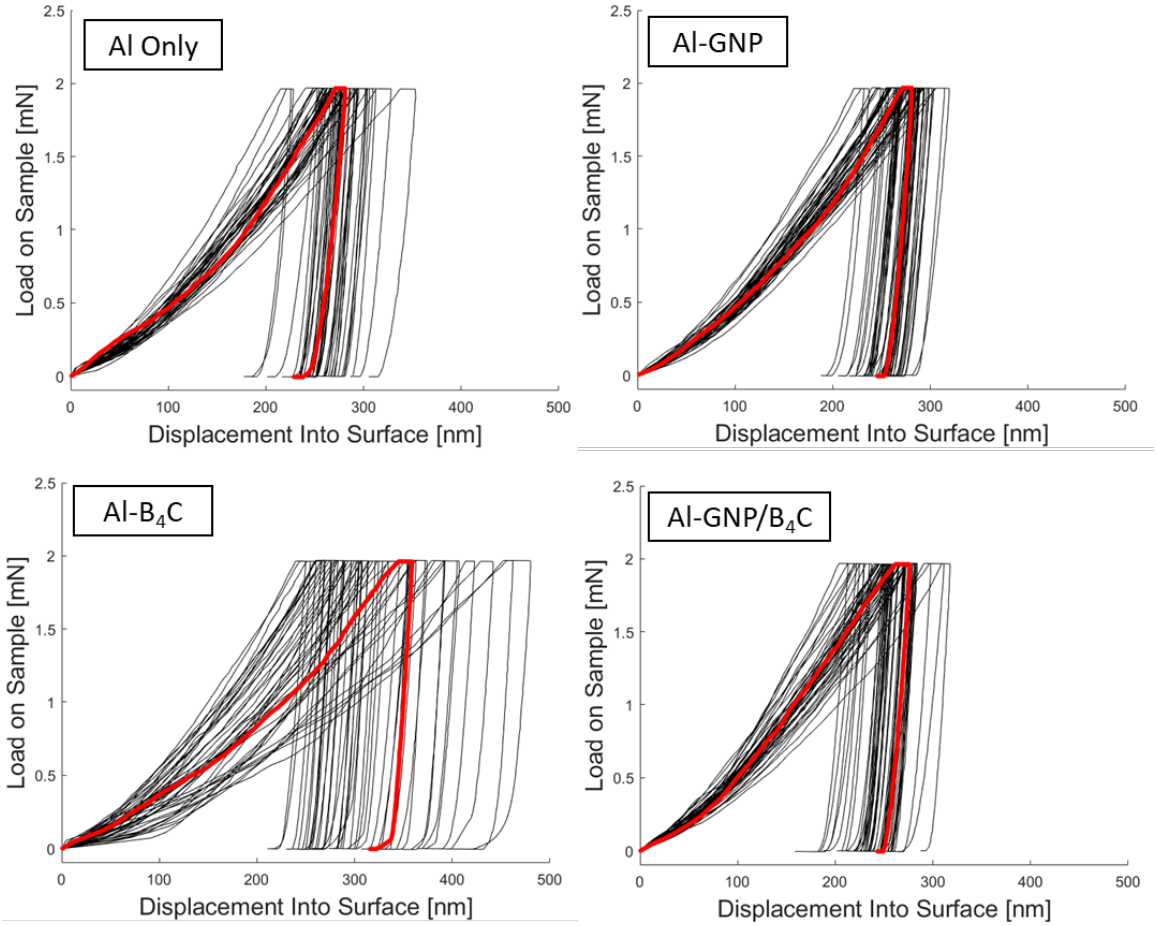

Figure 29. Load and displacement curves from nanoindentation

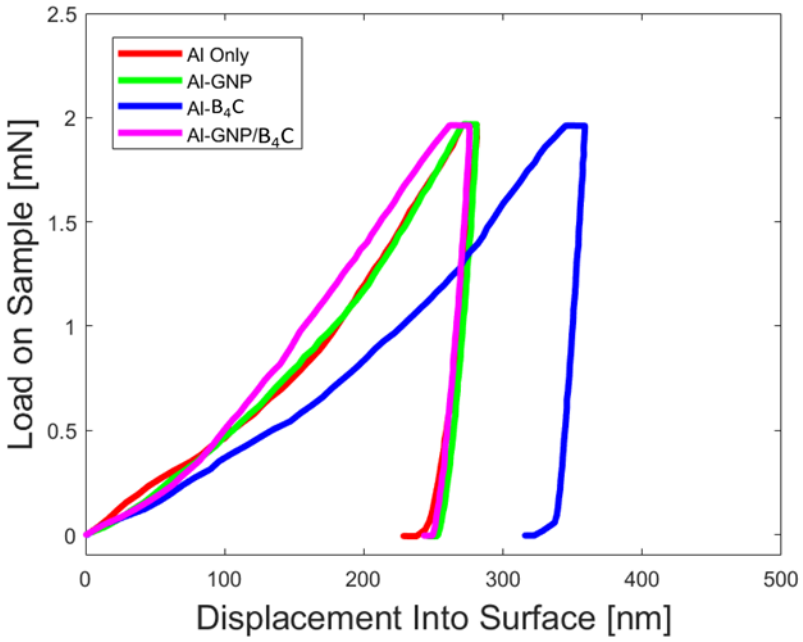

Figure 30. Average load and displacement curves compared

Using the unloading curves, plasticity can be calculated by the ratio of maximum displacement to the displacement remaining after the load is completely removed. This calculation was performed for each nanoindentation and the averages were recorded in Figure 31. The Al-GNP and the Al-GNP/μB4C coatings had about the same plasticity as the pure Al, but the Al-μB4C coating had a 2.3% increase in plasticity.

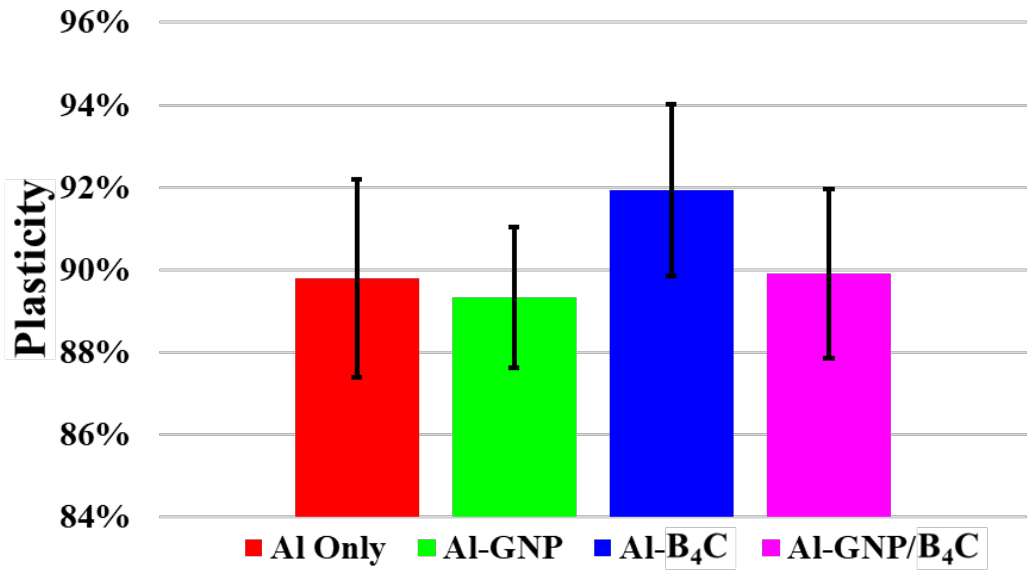

Figure 31. Plasticity calculated from load-displacement curves

C. ADHESION

After performing all adhesion tests, values for the maximum stress were averaged for each sample as shown in Figure 32. All tests were added to this plot regardless of failure mode. Samples containing μB4C experienced an increase in adhesion strength with the 2 vol.% μB4C sample being the highest with a 39.6% increase. The Al-GNP/μB4C sample, however, maintained much of this increase in adhesive strength with only 1 vol.% μB4C. This is due to the μB4C particles acting as anchors within the splat boundaries, strengthening the interlocking mechanism between layers of Al particles.

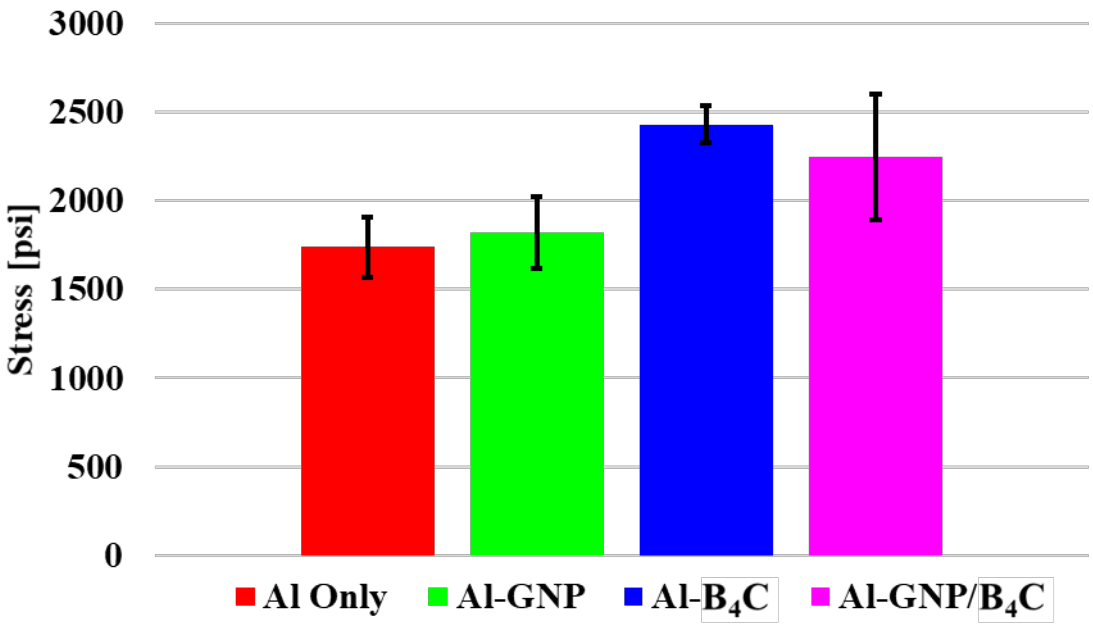

Figure 32. Average maximum stress from adhesion test

Adhesive tests will either fail between the coating and the substrate, within the coating, or within the testing epoxy. These tests can also fail with a combination of these failure modes. The failure modes experienced from samples in this experiment are shown in Figure 33. All 5 of the Al coatings experienced adhesive failure with peeling as shown in Figure 33a. This mode is an adhesive failure between the coating and the substrate where the coating does not break off but pulls the surrounding coating away with it. This failure mode shows us that the pure Al coating has a high cohesive strength within the coating layer because it did not fracture. All the other adhesion tests containing reinforcements experienced plain adhesive failure, and one of the Al-μB_4C tests is shown in Fig.33c. This test had a mixed failure mode, adhesive and epoxy failure. The value for this test fits the data from the other four tests, so it is likely that the adhesive failure happened first, and as the dolly lifted, the epoxy broke off the surface.

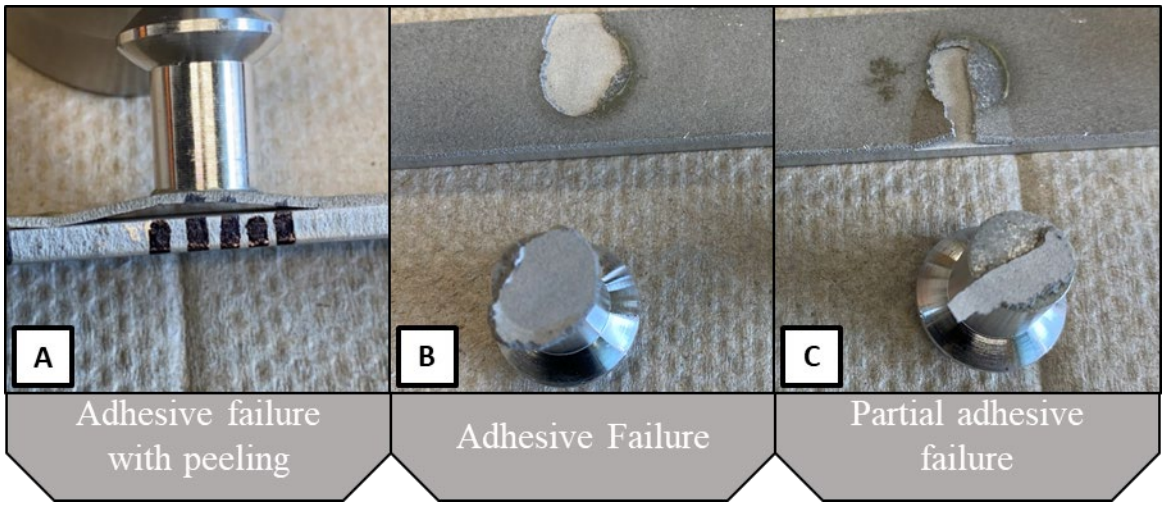

Figure 33. Modes of coating failure during adhesion tests. a) adhesive failure with peeling, b) adhesive failure, and c) partial adhesive failure

The adhesion test closest to the average max stress for each composition was cross-sectioned and polished for imaging. Figure 34 shows images from the pure Al coating adhesion test. Figure 34a shows two Al particles separated by a splat boundary then widens as it goes down the image. These Al particles are located at the end of the crack formed from the adhesion test. Resin has filled this crack and stopped where the Al particles are still together. Figure 34b shows the part of the coating that was pulled from the substrate but did not break from the coating. All the adhesion cross sections for all compositions experienced this lip formation around the adhesion test. The formation of this lip is a sign that all samples have a higher cohesive strength in the coating than adhesive strength to the substrate. Figure 34c shows the edge of the coating that was fractured at the edge of the testing dolly. The fracture surface here is similar to the coating where the fracture happens at the splat boundary.

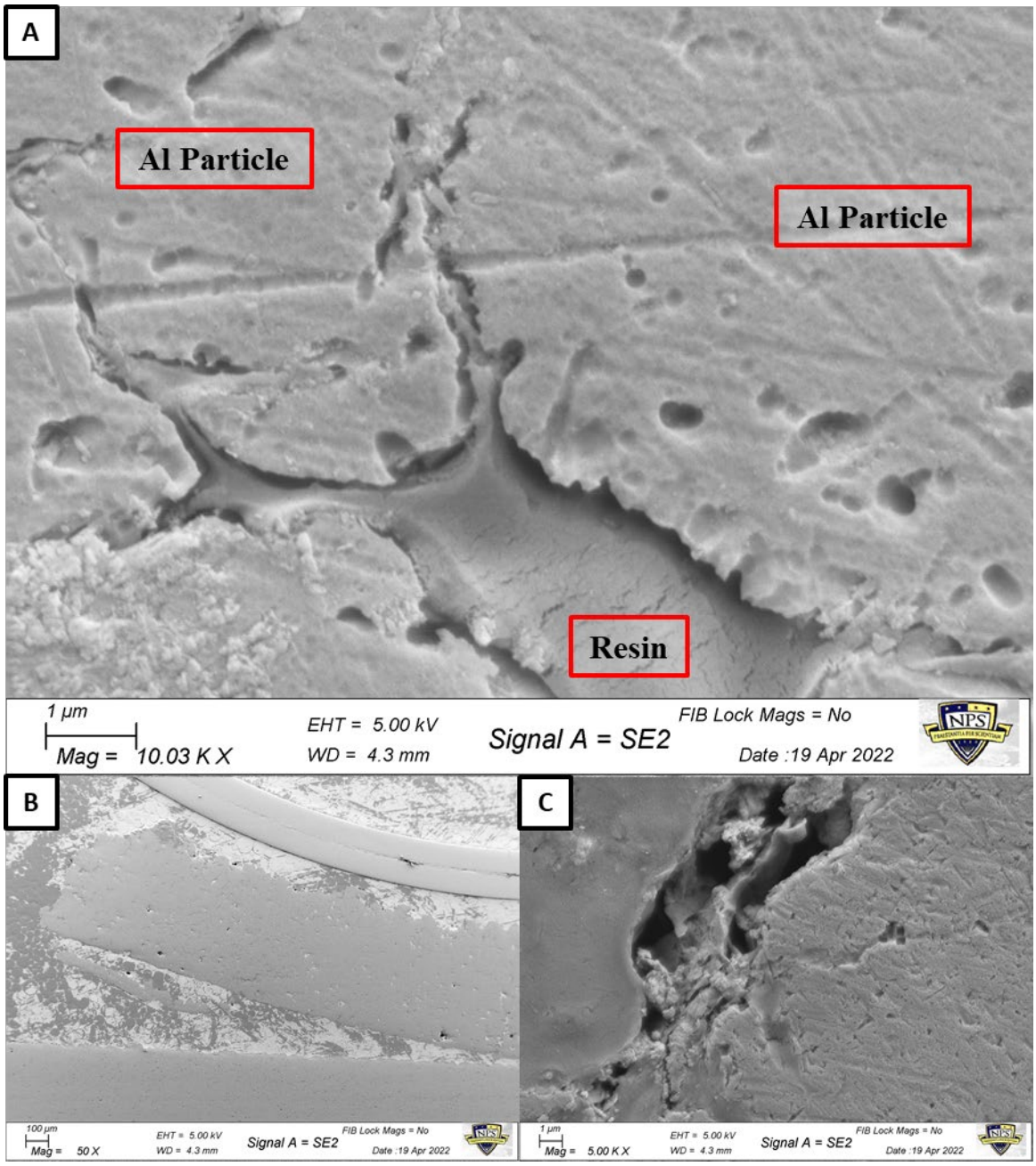

Figure 34. Al adhesion test cross-section showing a) a resin filled crack, b) peeled coating, and c) the fracture surface

The adhesion test cross-section of the Al-GNP coating is shown in Figure 35. This is a similar lip formation that was discussed earlier. The dolly pulled at the coating just to the left of this image where it fractured off a piece of the coating. This piece pulled at the

surrounding coating which caused a section of the coating to lift from the substrate and fracture at the hinge point to the right.

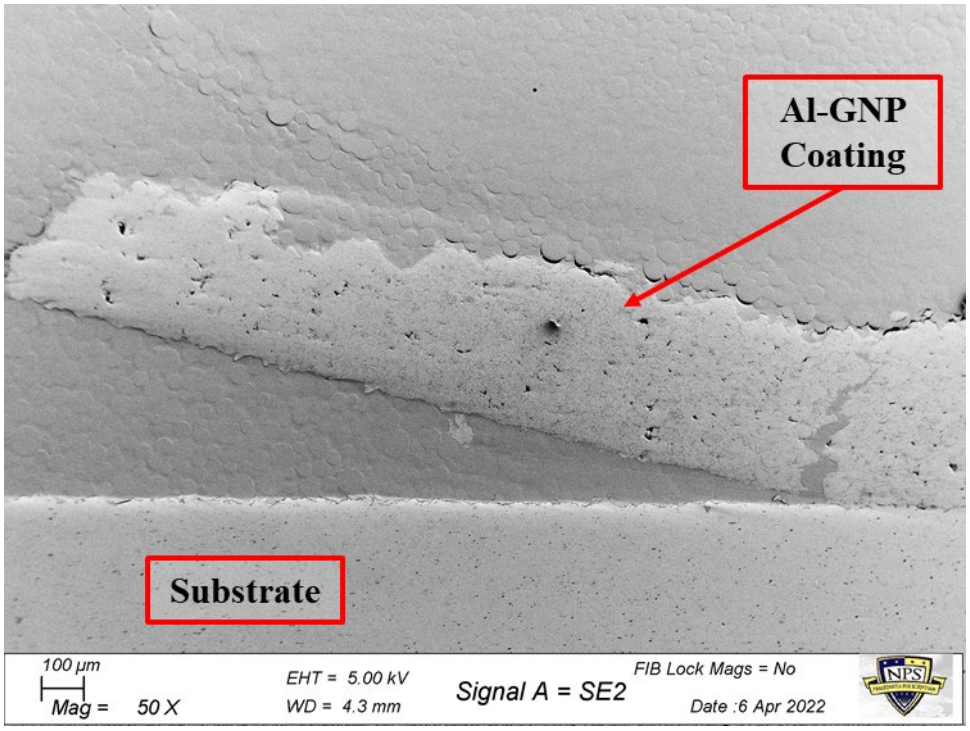

Figure 35. Al-GNP adhesion fracture cross-section

GNPs were found along fracture lines at the splat boundaries as shown in Figure 36. Figure 36a shows a GNP lodged in the splat boundary between two Al particles. The lower left particle is adjacent to the fracture line but was held to the above Al particle during the adhesion test. Figure 36b shows a GNP that has been pulled from the surface of an Al particle. The body at the lower left of the image is resin and the GNP is seen hanging from the Al particle. Figure 36c also shows a GNP along a fractured splat boundary. This GNP is embedded in the lower Al particle and extends into the gap filled with resin above. These GNPs are all located along splat boundaries and are affected when those boundaries are fractured. Energy is used up in the process of pulling on these GNPs that act as anchors or bridges between Al particles.

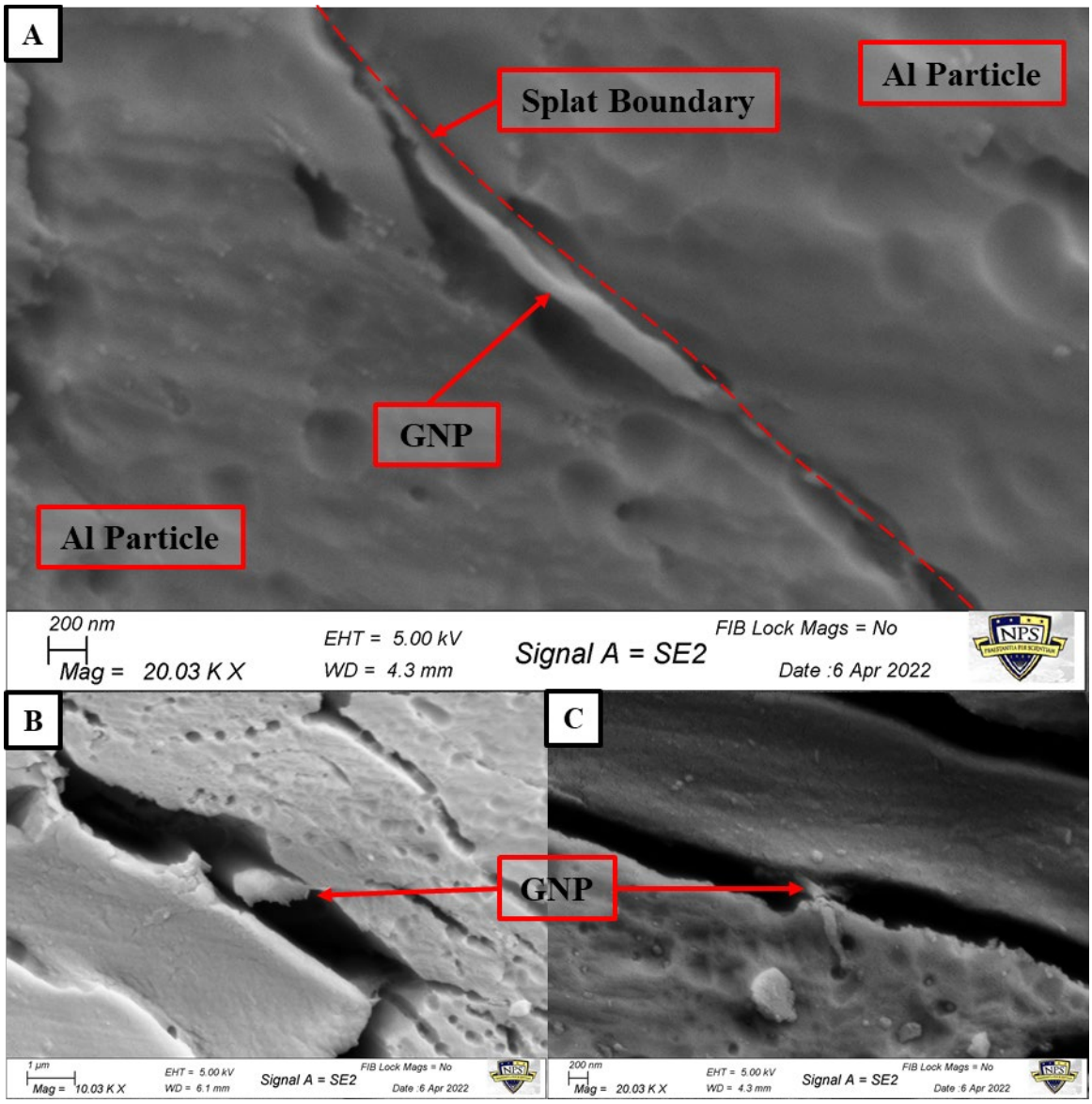

Figure 36. Al-GNP adhesion test showing GNPs a) between two Al particles, b) peeled from coating, and c) imbedded in an Al particle

The Al-µB_4C coatings experienced the highest stress before failure during the adhesion tests. This increased adhesive strength is due to the µB_4C particles located along splat boundaries as shown in Figure 37. Figure 37a shows the coating fracturing from the substrate. Figure 37b and Figure 37c show µB_4C particles that are in this crack along the fractured splat boundaries. It is assumed that during the adhesion test, loads are transferred to the µB_4C particles before fracturing along splat boundaries. This load transfer increases

the needed stress to fracture the splat boundaries because of μB4C's high hardness and strength.

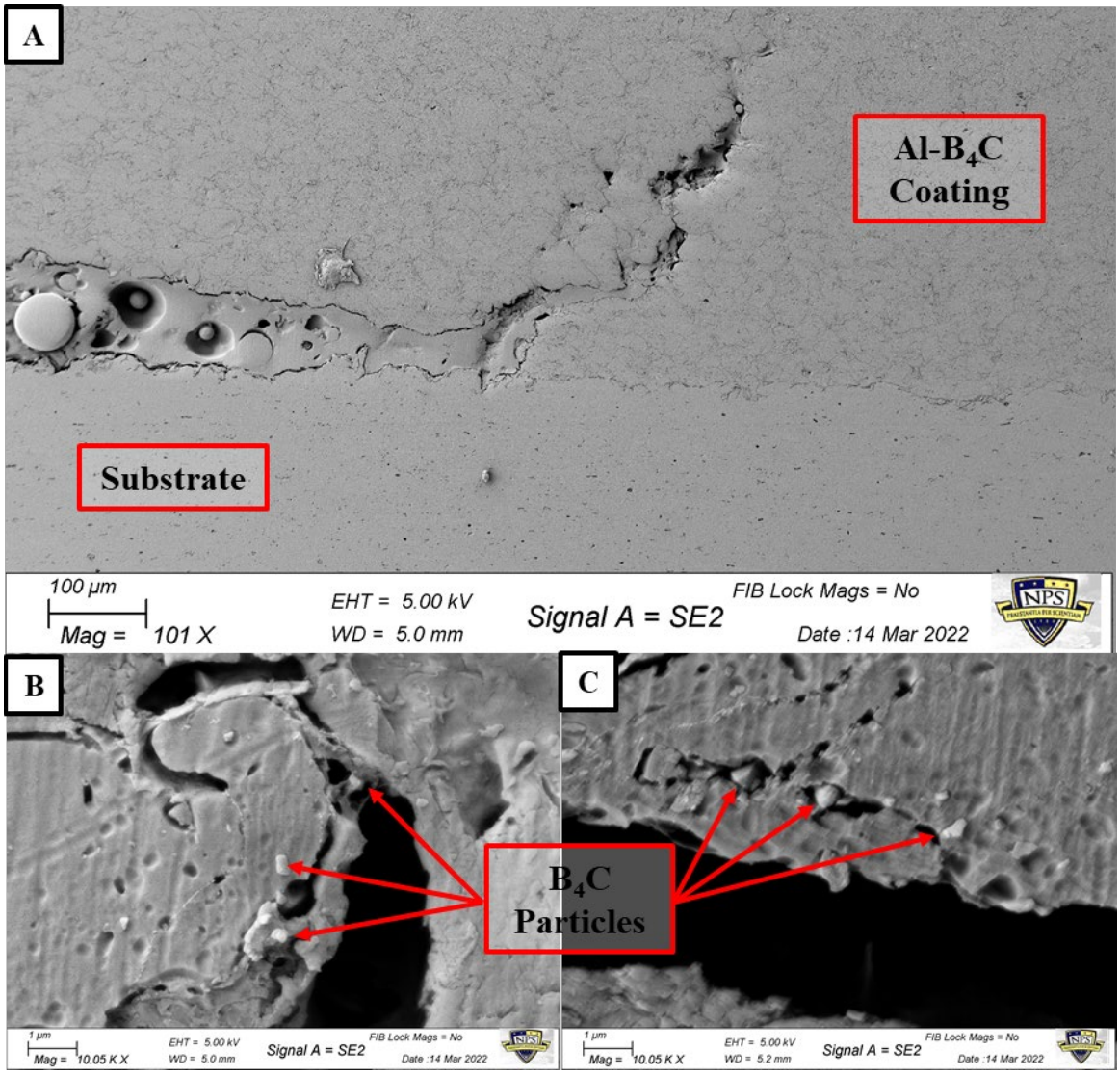

Figure 37. Al-μB4C adhesion test cross-section showing a) the cracked coating, and b, c) μB4C particles

Figure 38 shows the presence of GNPs and μB4C particles along the splat boundaries that fractured during the adhesion test in the Al-GNP/μB4C coating. Figure 38a shows a GNP that is attached to an Al particle adjacent to the fracture in the coating. Resin is shown along the bottom edge of the image, filling the crack between the substrate and

the coating. Figure 38b and Figure 38c show μB4C particles along the fractured splat boundaries.

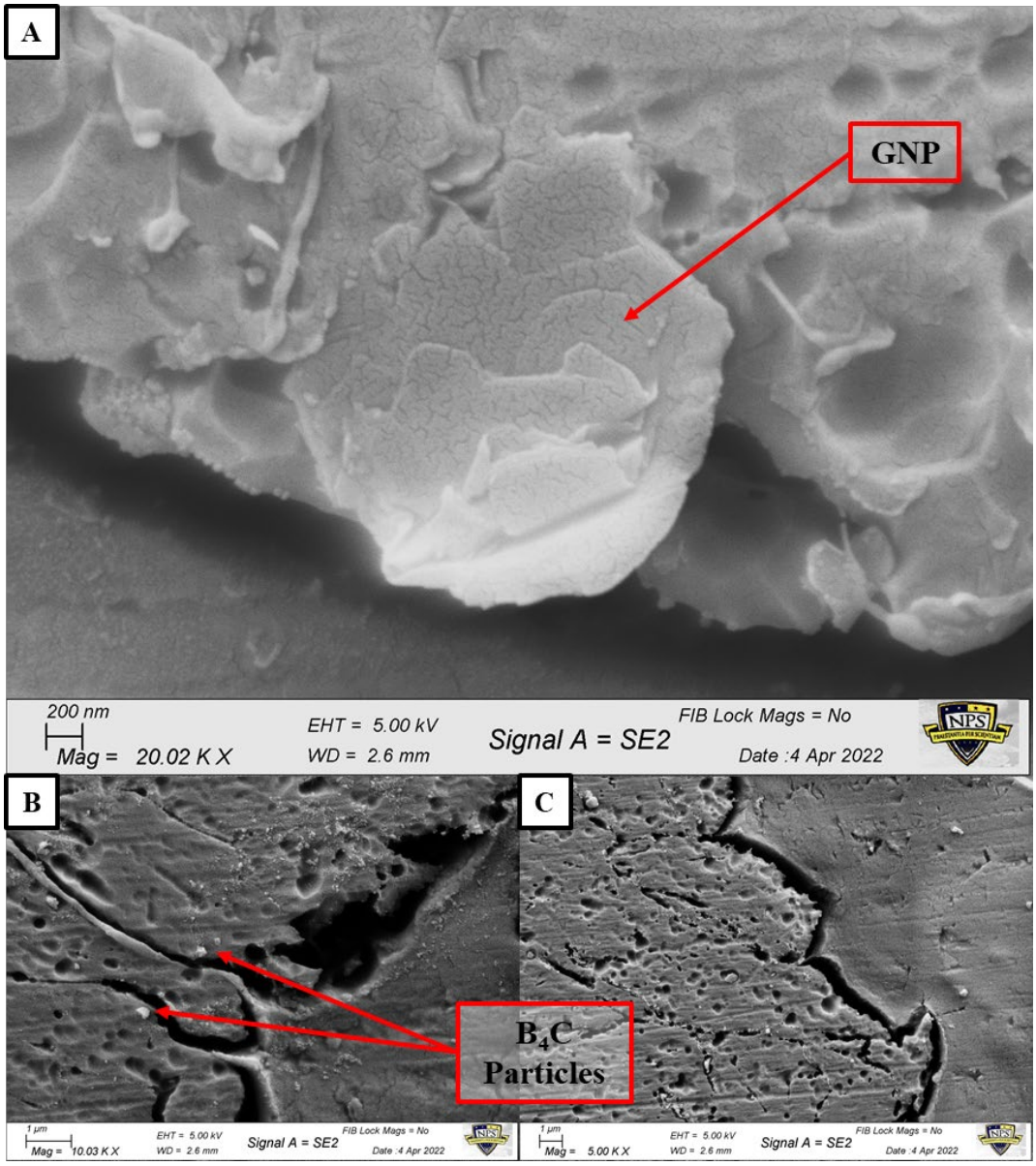

Figure 38. Al-GNP/μB4C adhesion test cross-section showing a) GNP and b) μB4C particles

The fracture surface from the pieces of coating that remained attached to the dollies can show how the reinforcements are interacting with the Al particles. The coating on the

dollies was imaged in the SEM perpendicular to the pull direction. Figure 39 shows the pure Al coating fracture surface. It is noted in Figure 39a and Figure 39b that the bright particulates are not μB_4C, as there is none present in the coating. Figure 39c shows the full coating fracture surface with the epoxy layer still attached above. The black space below the coating is where the substrate was before the adhesion test.

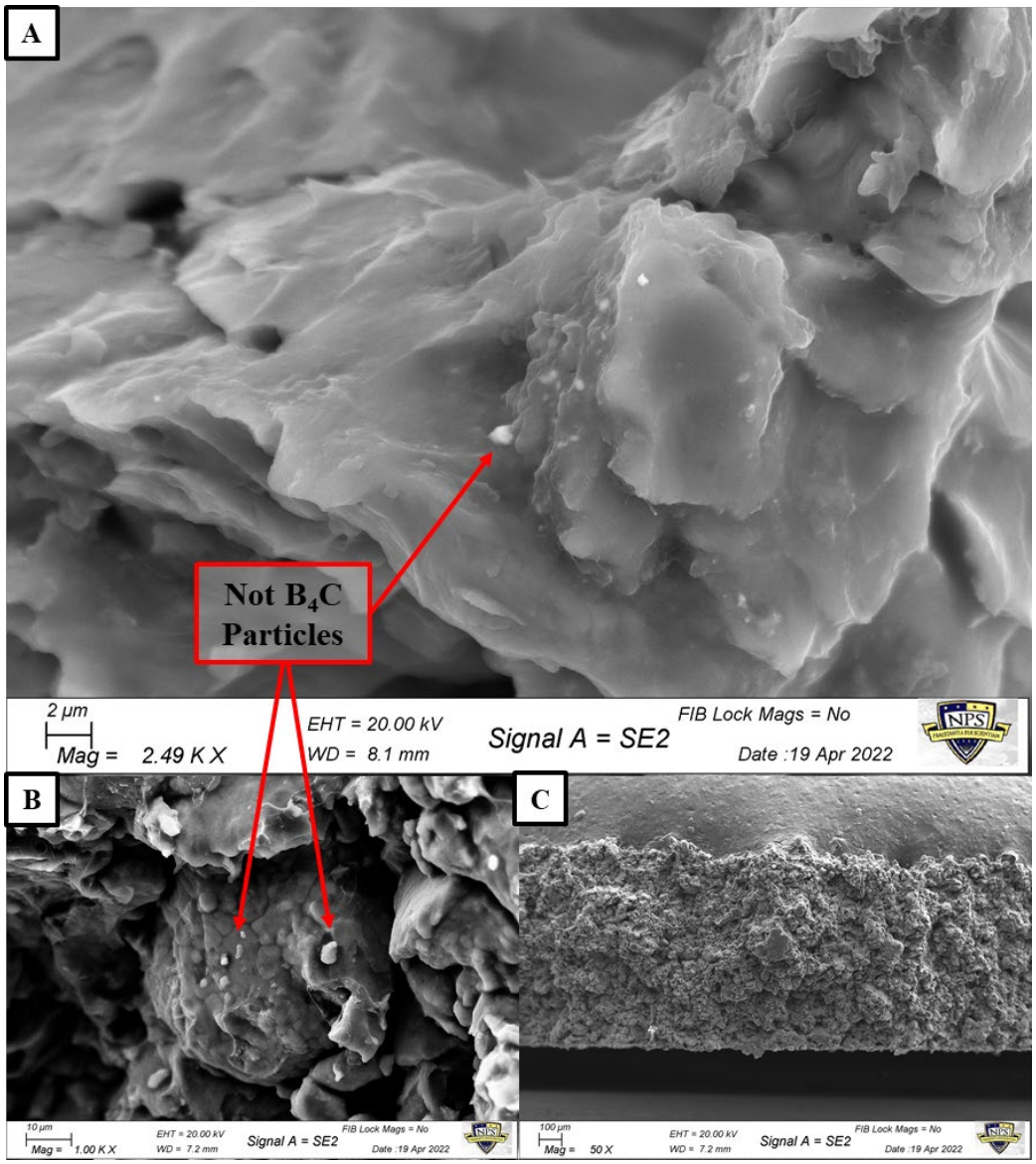

Figure 39. Al Only adhesion fracture surface showing, a, b) pure Al coating, and c) entire fracture surface

Figure 40a, Figure 40b, and Figure 40c show GNPs present in the fracture surface. Most of the GNPs are hanging off the surface of Al particles which may show that they also adhered to the Al particle across the fracture surface. These GNPs formed bridges between the Al particles across the fracture boundary.

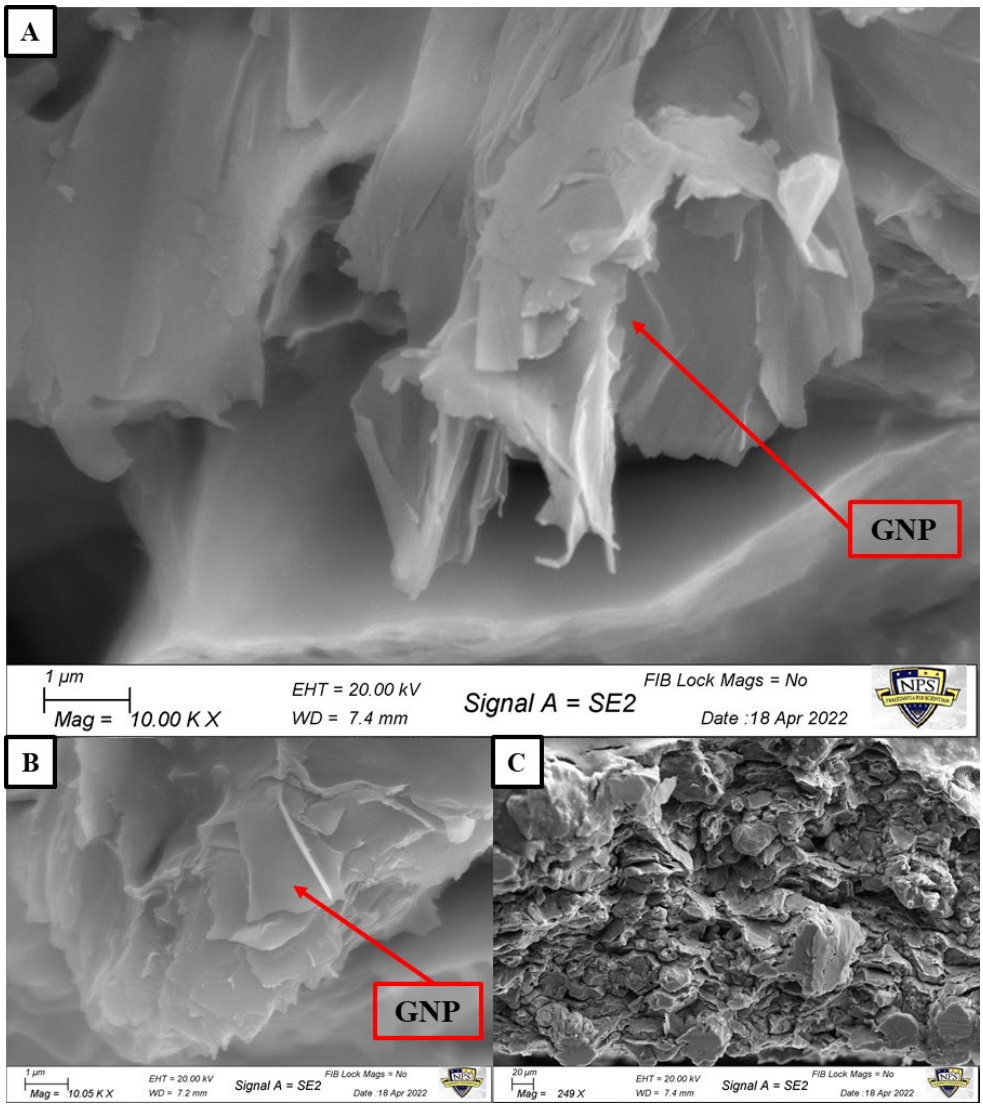

Figure 40. Al-GNP coating adhesion fracture surface with a, b) exposed GNPs, and c) low magnification of fracture surface

µB_4C particles can be seen along the fracture surface of the Al-µB_4C coating as shown in Figure 41a. This particle is most likely µB_4C because of its jagged ceramic-like

geometry and because of the brightness it has under SEM compared to the conductive Al surrounding it. Figure 41b shows a piece of Al along the bottom surface of the coating. This particle was attached to the substrate before adhesion testing and slightly peeled from the coating as the coating detached from the substrate. This peeled particle is also covered in μB_4C particles. Fig.41c shows the entire thickness of the coating fracture surface. Like the single-reinforcement coatings, the Al-GNP/μB_4C fracture surface shows exposed GNPs in Figure 42a, Figure 42b, and Fig.42d and μB_4C particles in Figure 42c. Table 13 summarizes the mechanical properties studied so far.

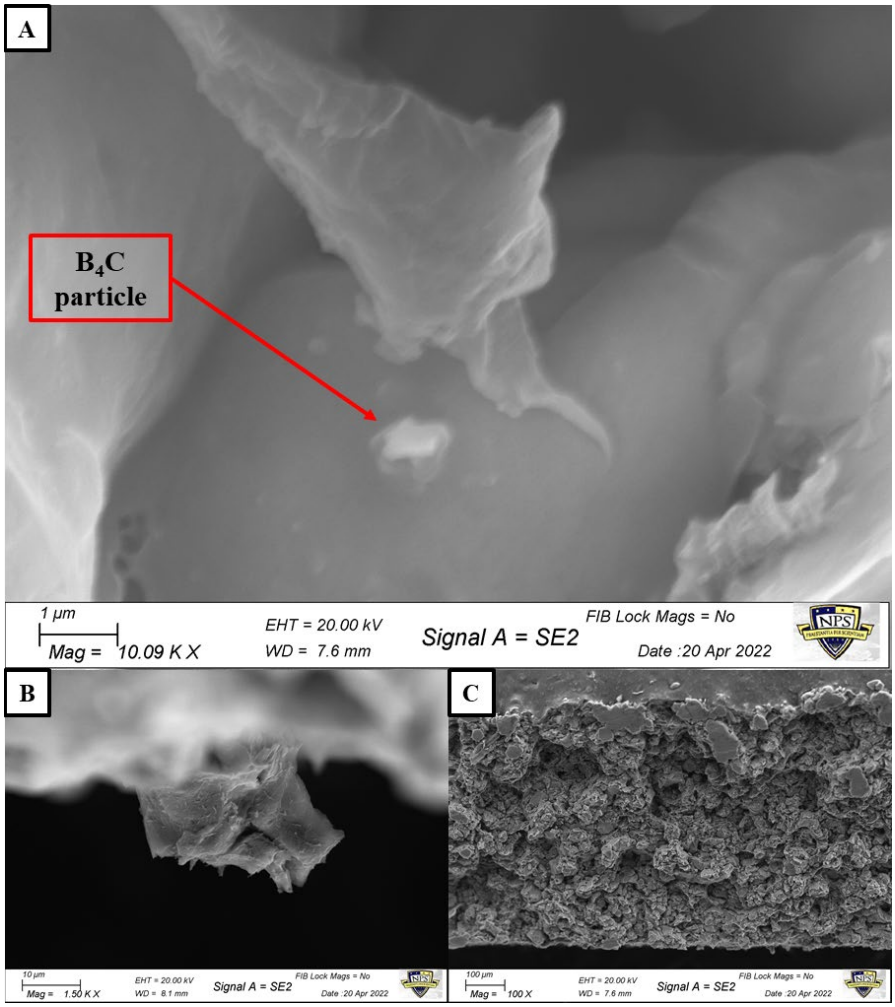

Figure 41. Al-µB4C coating adhesion fracture surface showing a) exposed µB4C particles, b) peeled Al particle with µB4C, and c) entire fracture surface

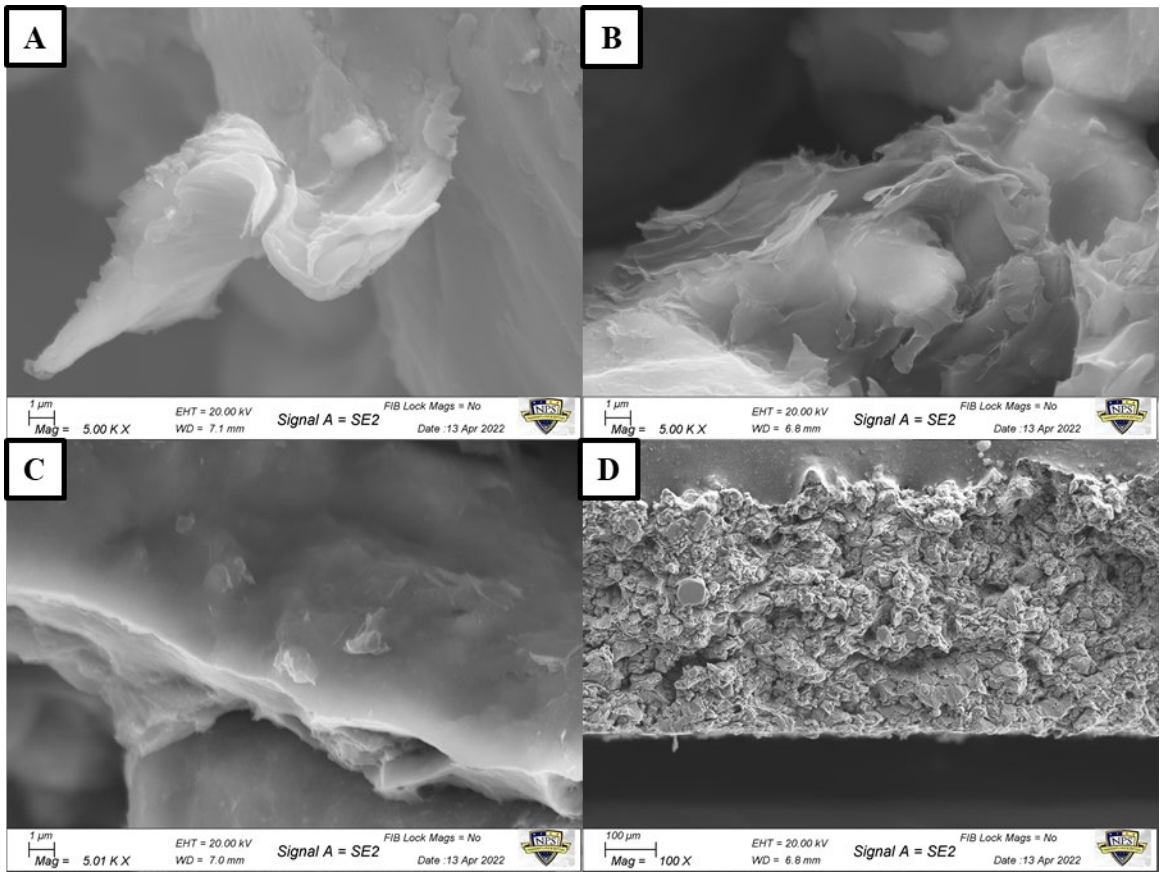

Figure 42. Al-GNP/µB4C coating adhesion fracture surface showing a, b) exposed GNPs, c) exposed µB4C particles, and d) low magnification of fracture surface

Table 13. Summary of mechanical properties

Composition	Micro-hardness [GPa]	SD [GPa]	Nano-hardness [GPa]	SD [GPa]
Al	0.2722	0.0422	0.9660	0.1970
Al-GNP	0.4758	0.0681	0.9870	0.1500
Al-B_4C	0.4112	0.0462	0.7520	0.2280
Al-GNP/B_4C	0.4020	0.0599	1.1350	0.2970
Composition	**Plasticity [%]**	**SD [%]**	**Adhesion strength [psi]**	**SD [psi]**
Al	89.7932	2.3956	1740.00	169.51
Al-GNP	89.3340	1.7001	1818.00	202.36
Al-B_4C	91.9361	2.0805	2429.00	105.64
Al-GNP/B_4C	89.9166	2.0572	2244.00	354.30
Composition	**Elastic Modulus [GPa]**	**SD [GPa]**		
Al	64.3740	12.7490		
Al-GNP	57.7800	5.7930		
Al-B_4C	62.6030	12.3410		
Al-GNP/B_4C	72.5960	11.4750		

D. WEAR

Each sample underwent wear testing and its mass was recorded before and after each test. Figure 43 shows the average mass loss due to wear for each sample. The amount of mass lost to wear is inversely proportional to the coating wear resistance. The plain aluminum coating experienced the least amount of mass loss and any addition of reinforcements decreased overall wear resistance. This is due to the nonhomogeneous composition of the coatings causing them to become less dense. The Al-GNP coating experienced the worst wear resistance with a 300% increase in mass lost during an identical wear test. The coefficient of friction was also measured in real-time and averaged throughout the 1-hour test and is shown in Figure 44. The coefficients of friction for each sample were almost indistinguishable between compositions, all about 0.53.

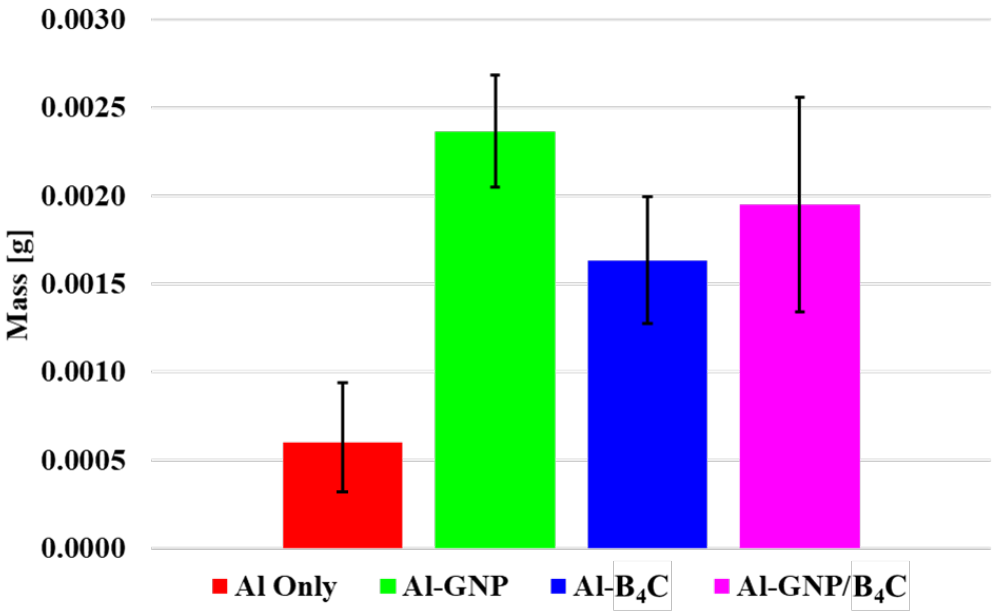

Figure 43. Average mass loss during the wear test

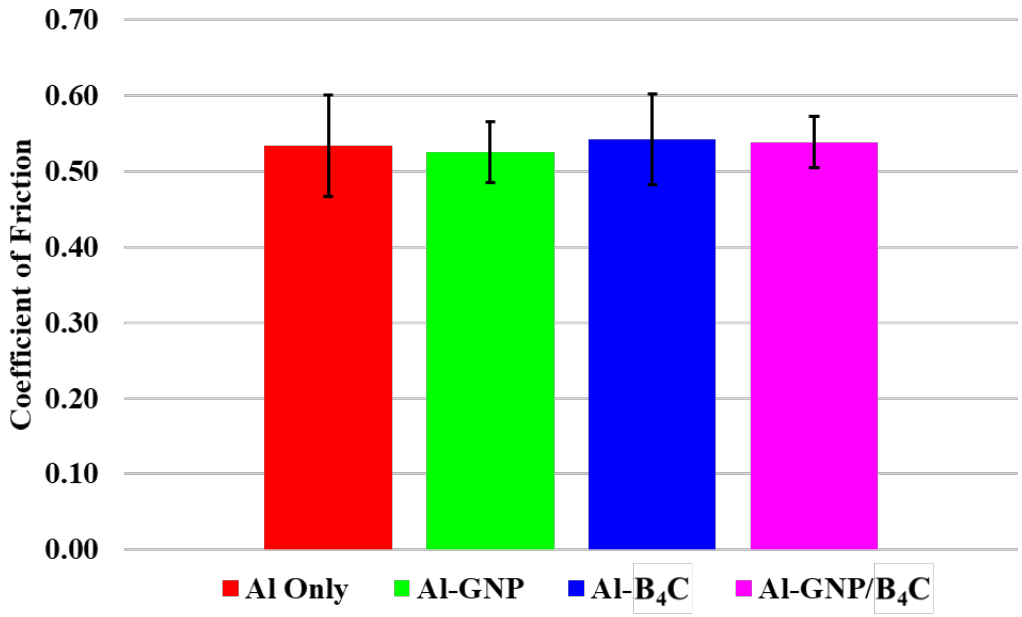

Figure 44. Average coefficient of friction during the wear test

The coefficients of friction were recorded in real-time and plotted for each of the six tests as shown in Figure 45. Real-time data received from the wear tester was noisy and could not be plotted for comparison so it was manipulated using a moving mean of every three adjacent data points. The data remains rough but still shows useful information. Most of the trends begin with a high coefficient and lowers over time. This is representative of the formation of the wear tracks, where at the beginning, friction is high due to the roughness of the cold-sprayed coating surface.

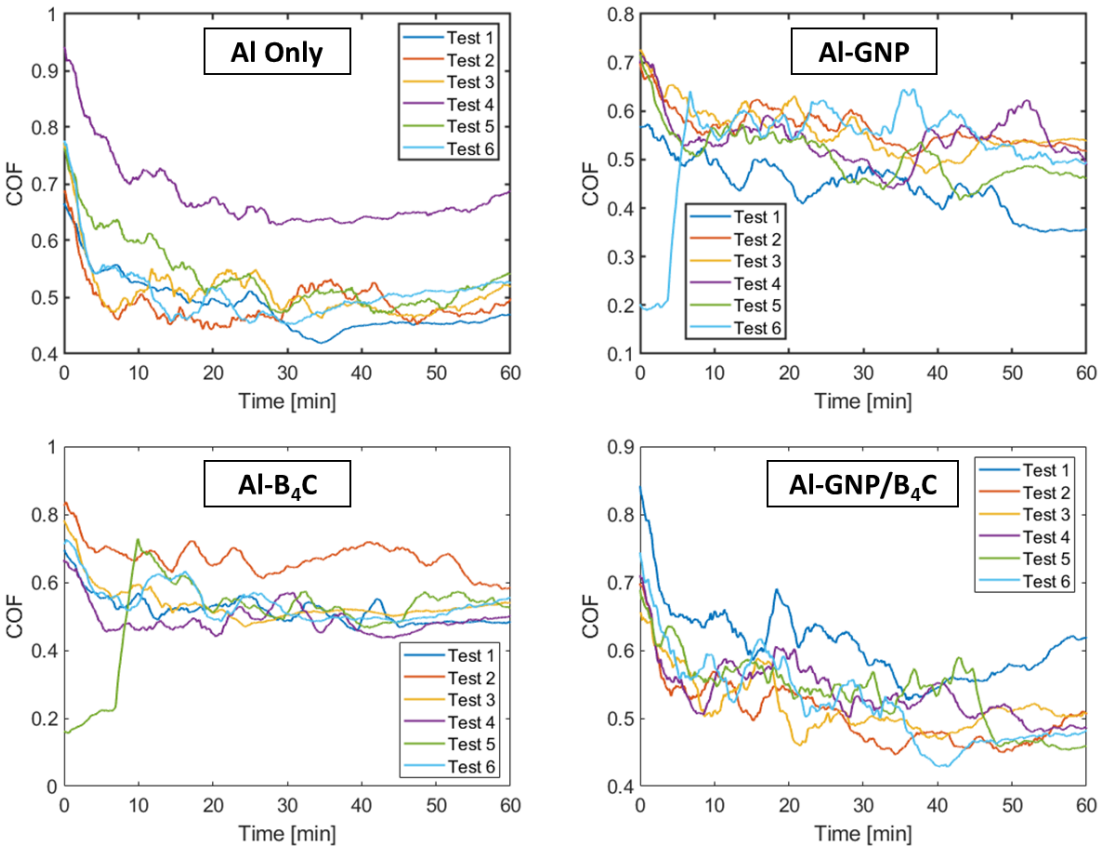

Figure 45. Real-time coefficients of friction during the wear test

For each composition, the wear test which had the closest mass loss to the average for that composition was chosen for comparison in Figure 46. Here, it is visible as to why the coatings all experienced similar average coefficients of friction.

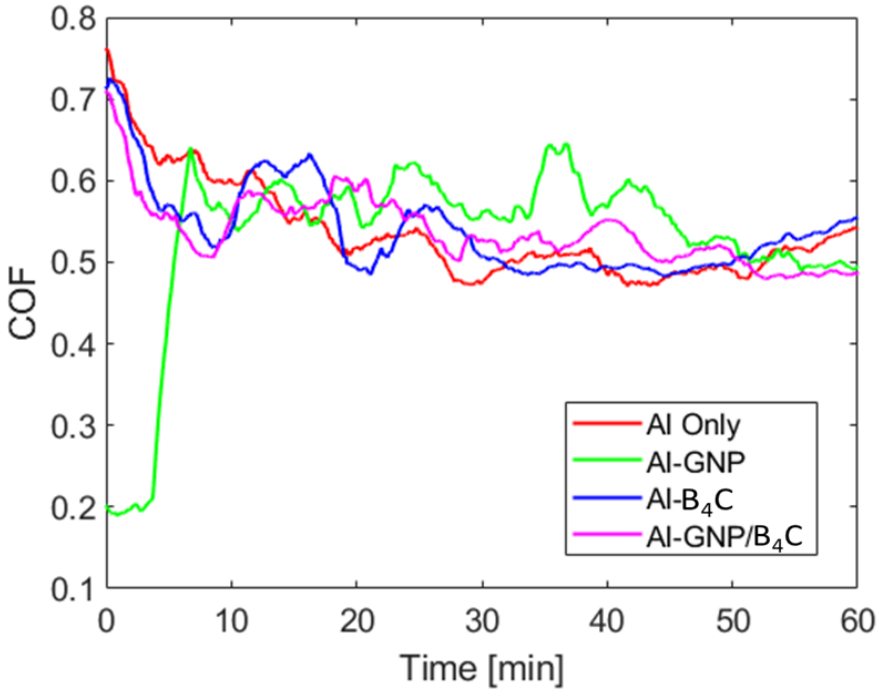

Figure 46. Combined real-time coefficient of friction for the average wear test

Similarly, to the coefficients of friction, the depth of the encoder was also recorded in real-time and plotted for each of the six tests as shown in Figure 47. Data received for the encoder depth was also noisy, so it was manipulated using the same moving mean as before. Each test was zeroed out to start at a zero-depth. The negative depth values are measurements above the original starting position. This could be due to the samples and coating surfaces not being flat and from an initial buildup of wear debris.

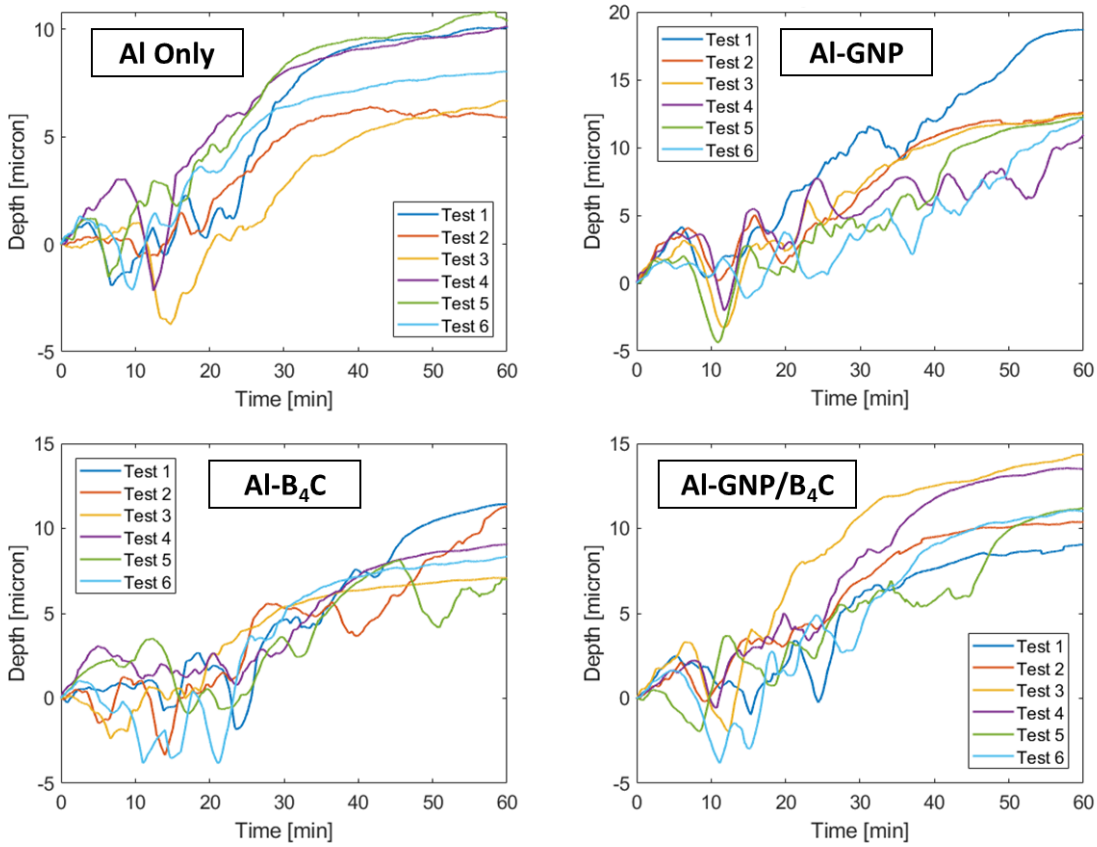

Figure 47. Real-time encoder depth during the wear test

As done for comparison before, the wear tests closest to the average mass loss for each composition are compared in Figure 48. There is a lot of variation in depth from test to test among compositions. The test with the average mass loss for the composition may vary significantly from other tests on that composition. For this reason, the plot of average mass loss in Figure 43 must be analyzed together with the plot in Figure 48. The pure aluminum coating lost less mass during the wear test than any of the reinforced coatings but appears to wear to a similar depth. This is due to the lower hardness of the pure Al coating that allows for a depression of the Al particles in the wear track rather than a removal of the mass. The Al-GNP coating experienced the greatest hardness in the macro hardness tests and experienced the greatest mass loss during the wear tests. This is a sign of the Al-GNP coating being more brittle. Instead of depressing the Al-GNP coating in the wear track, more material is removed as debris. The Al-μB4C coating experienced the least

mass loss due to wear among the reinforced coatings but shows the deepest wear depth. This could be a combination of the decreased wear resistance due to the presence of GNPs and the μB4C particles being pressed deeper into the coating during the wear process.

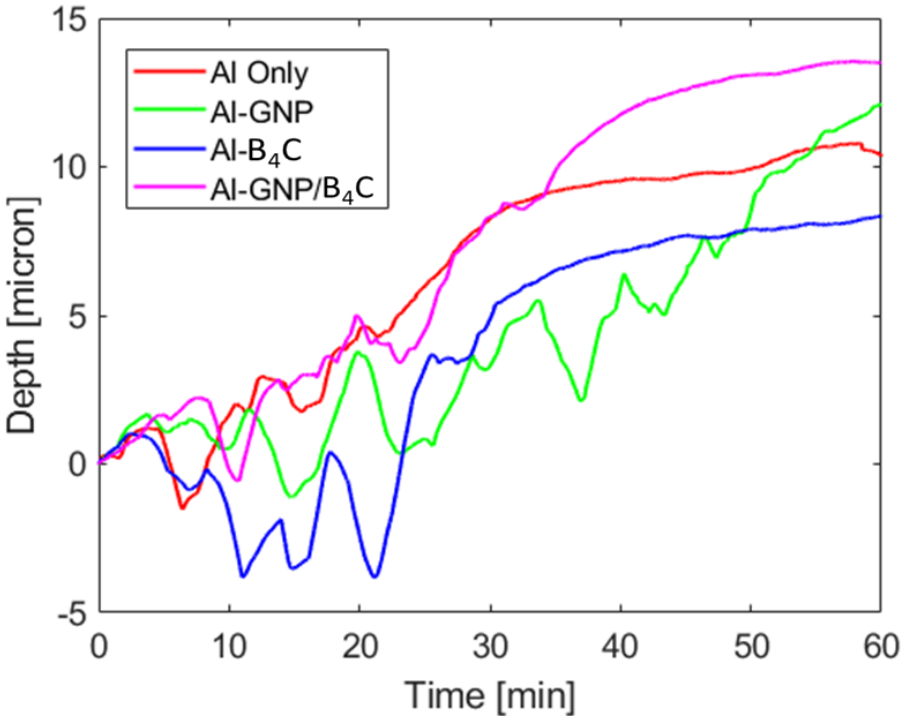

Figure 48. Combined real-time encoder depth for the average wear test

The wear tracks are formed by a combination of removing mass from the track and pushing the material down and to the sides of the track. A 3D surface scan of the Al-GNP/μB4C wear track is shown in Figure 49. Here the regions in blue are the deepest points in the wear track and the orange to red areas are above the average height of the coating. The counter surface ball creates concentric grooves in the wear track. These grooves are formed from third-body particles adding to the wear mechanism. Hard particles like μB4C may have been pulled out of the Al coating and used as an abrasive between the counter surface ball and the softer Al.

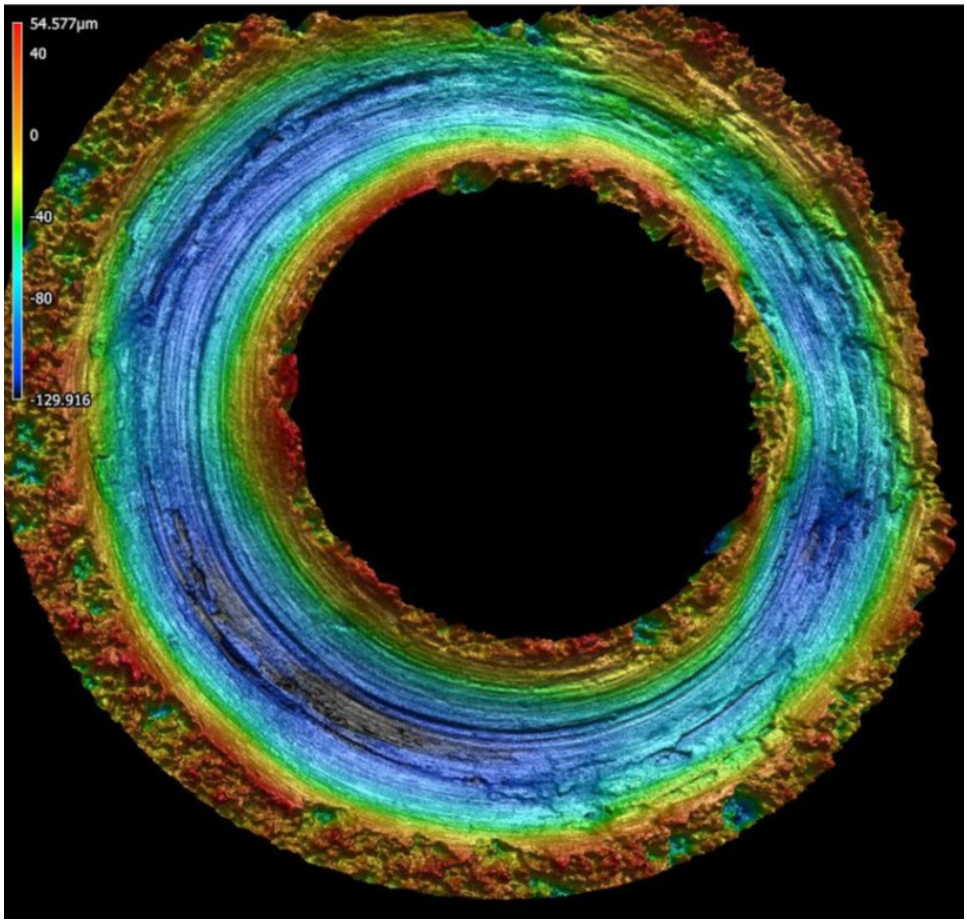

Figure 49. 3D surface scan of Al-GNP/µB4C wear track

The wear tracks were examined under SEM to look for methods of wear and to describe how the coating was affected by the tests. The wear tests with the closest to the average mass loss were chosen for SEM imaging. Figure 50 shows the wear track on the pure Al coating as a baseline for examining the reinforced coatings. Figure 50a has a darker region in the middle of the curves to the right, which is the deep center of the wear track. Figure 50b and Figure 50c magnify the center of the wear track to look into a void in the wear track. As the counter surface slides over the coating, it plastically deforms the Al particles into a thin flat layer called a tribofilm. This film can then be peeled off and re-adhered to the coating throughout the wear test. The center of Figure 50c shows a void or peeled-off piece of the tribofilm with visible unworn Al particles underneath.

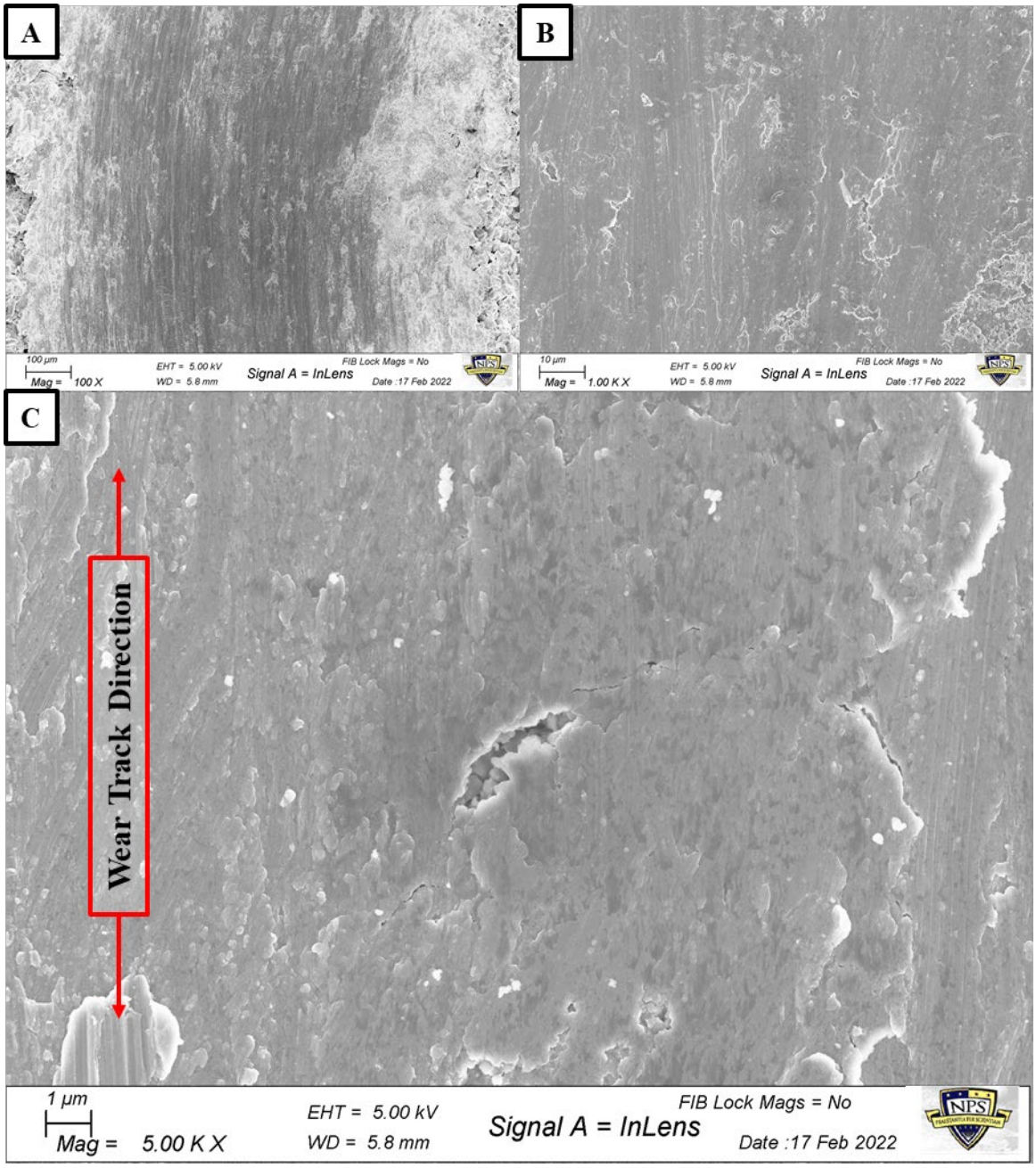

Figure 50. Al coating a, b) wear track, and c) tribofilm void

Many layers of GNPs are visible along the wear track in the Al-GNP coating shown in Figure 51. Figure 51a shows several GNPs stacked on top of each other with some kinked or folded over themselves. In the lower center of Figure 51a, a single layer of GNP is seen on top of a folded GNP. This fold line becomes slightly blurred once under the single layer of GNP because GNPs are often somewhat transparent under SEM. Figure 51b

and Figure 51c are of the same location, just magnified more in Figure 51c. Here a deeper area of the wear track is filled with overlapping GNP layers. Figure 51c shows that many pieces of GNPs are stacked and folded up on top of each other.

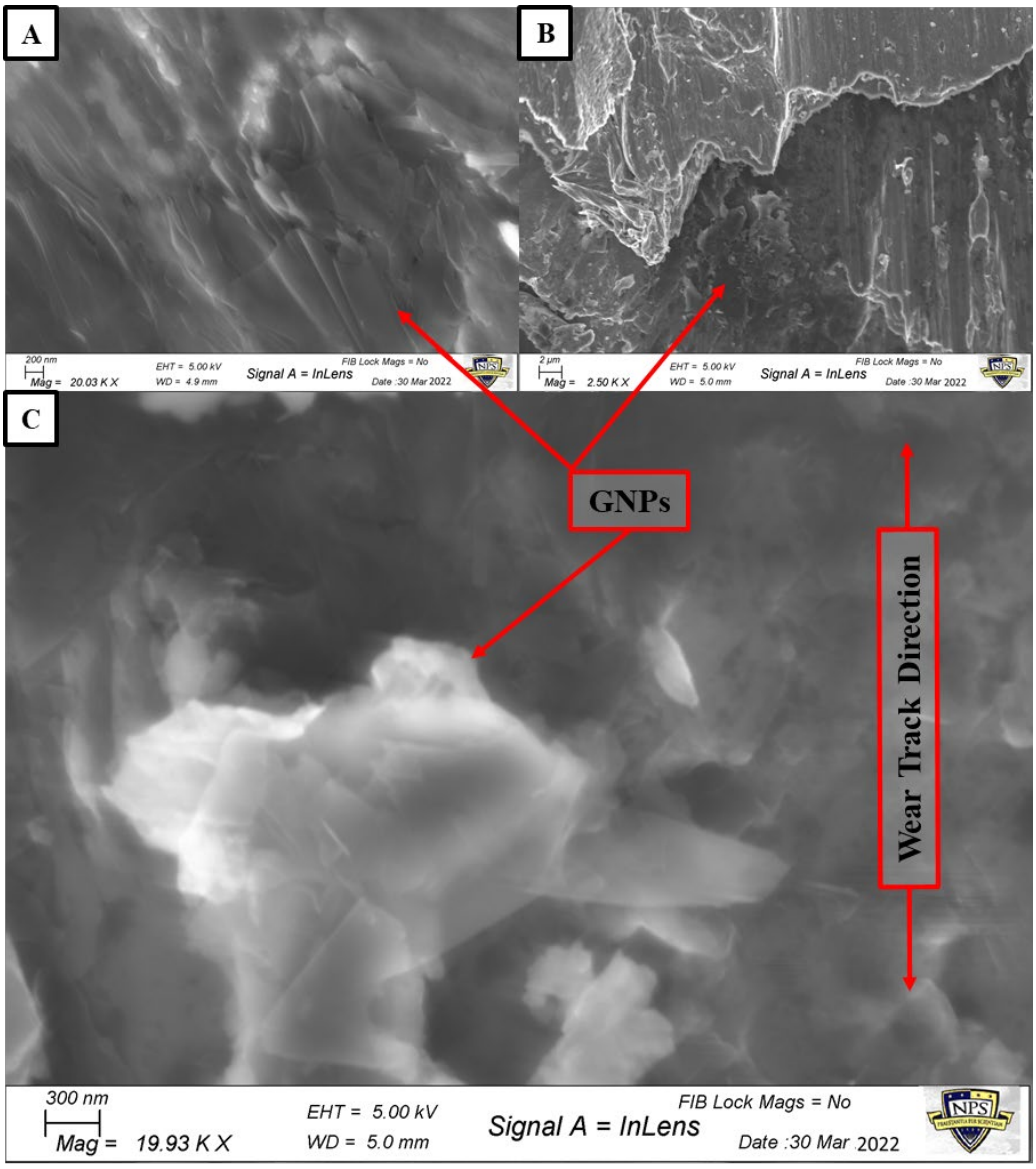

Figure 51. Al-GNP coating wear track showing a, b) exposed GNPs and c) high magnification of an exposed GNP

The wear track in Figure 52a and Figure 52b is showing the Al-μB_4C coating with μB_4C particles visible on the surface of the track. These particles are believed to be μB_4C

because of their size, geometry, and brightness under SEM. Loose µB4C particles on the surface of the wear track mean that they most likely acted as third body wear sources. These particles, which were once inside the coatings providing improved strength, now decrease the coating's wear resistance. Figure 52c is showing a deposit of wear debris containing Al and µB4C particles.

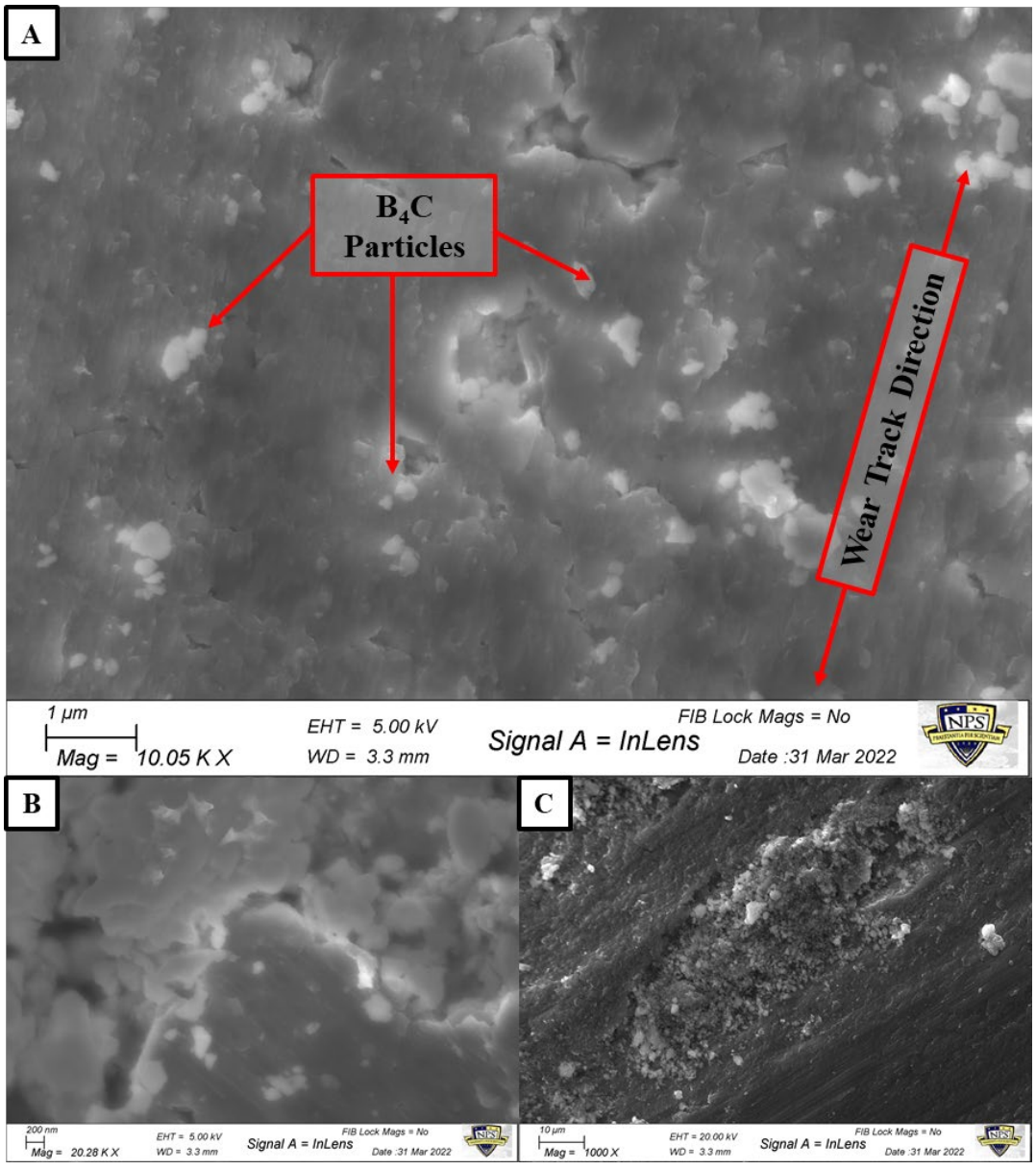

Figure 52. Al-µB4C coating wear track showing a, b) µB4C particles, and c) wear debris left on the wear track

Both μB4C particles and GNPs are seen together on the surface of the wear track for the Al-GNP/μB4C coating shown in Figure 53a and Figure 53b. Figure 53a shows a folded and kinked GNP lying next to a bright white particle. This particle was determined to be μB4C because of its brightness, geometry, and the lines seen over the particle due to charging under the SEM. Figure 53b and Figure 53c show the surrounding areas zoomed out to reveal more μB4C particles. Table 14 summarizes the wear data.

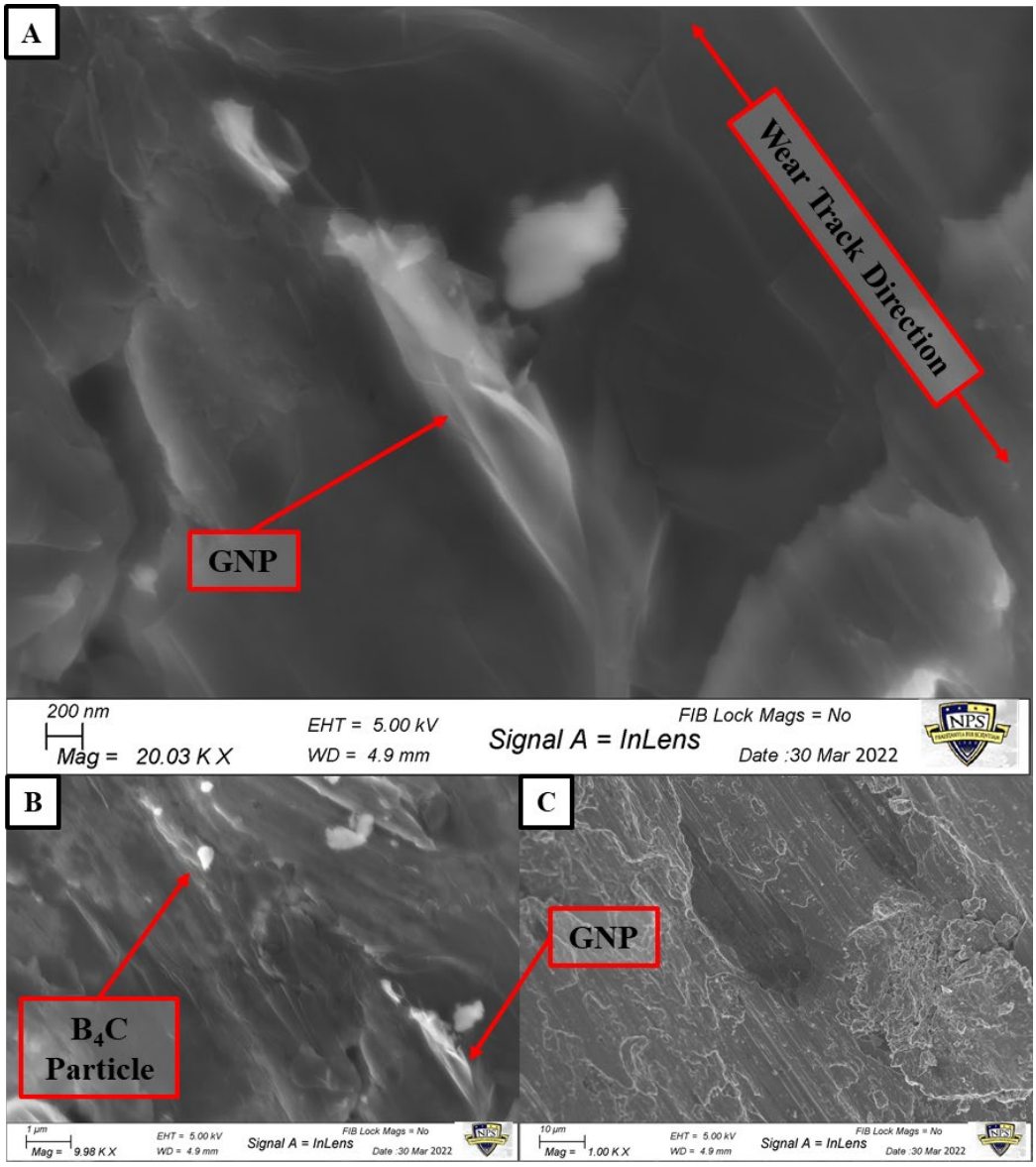

Figure 53. Al-GNP/μB4C coating showing both a, b) GNPs and μB4C particles, and c) wear track area

Table 14. Summary of wear data

Composition	Mass Loss [g]	SD [g]	Coefficient of Friction [ ]	SD [ ]
Al	0.0006	0.00034	0.5342	0.0671
Al-GNP	0.0024	0.00032	0.5256	0.0401
Al-B_4C	0.0016	0.00036	0.5428	0.0603
Al-GNP/B_4C	0.0020	0.00061	0.5389	0.0336

Composition	Max Z Depth [µm]	SD [µm]
Al	8.5155	1.7759
Al-GNP	13.5039	2.3251
Al-B_4C	9.2050	2.0267
Al-GNP/B_4C	11.5837	1.8108

E. EFFECTS OF REINFORCEMENTS

The coating containing just GNP reinforcements experienced decreased porosity after heat treatment but suffered during the cold spray process by producing a coating that was only half as thick as the pure aluminum. The Al-GNP coating had a 74.7% increase in hardness when measured using the micro-hardness tester. This increase in hardness was about 16% more than either Al-µB_4C or Al-GNP/µB_4C. The Al-GNP coating also exhibited a tight grouping in nanoindentation tests but showed a negligible increase in hardness and a 10% decrease in elastic modulus. For calculated plasticity and adhesion strength, the Al-GNP coating was indistinguishable from the pure Al coating. All reinforced coatings suffered decreased wear resistance with the Al-GNP coating having the greatest increase in mass loss (over 300%) during the wear test. From SEM imaging, it is visible how GNPs interact with the Al particles to strengthen the coatings.

Figure 54 shows a schematic of how GNPs act as bridges during a fracture event. The lower left box shows how many of the GNPs located along the splat boundaries that fractured would slightly peel off of the Al particles and bridge the gap. These GNP bridges strengthen the coatings during fracture events by providing additional support to Al particles across the fracture surface before they are pulled out. The bottom right box shows

how the GNPs would often be covered in µB4C particles. These µB4C particles add additional friction between the GNPs and the Al particles and help strengthen the coatings. The GNPs were also seen with thin strips of Al metal still attached to the pulled-out GNP. This is evidence of the GNPs being well adhered to the surface of the Al particles.

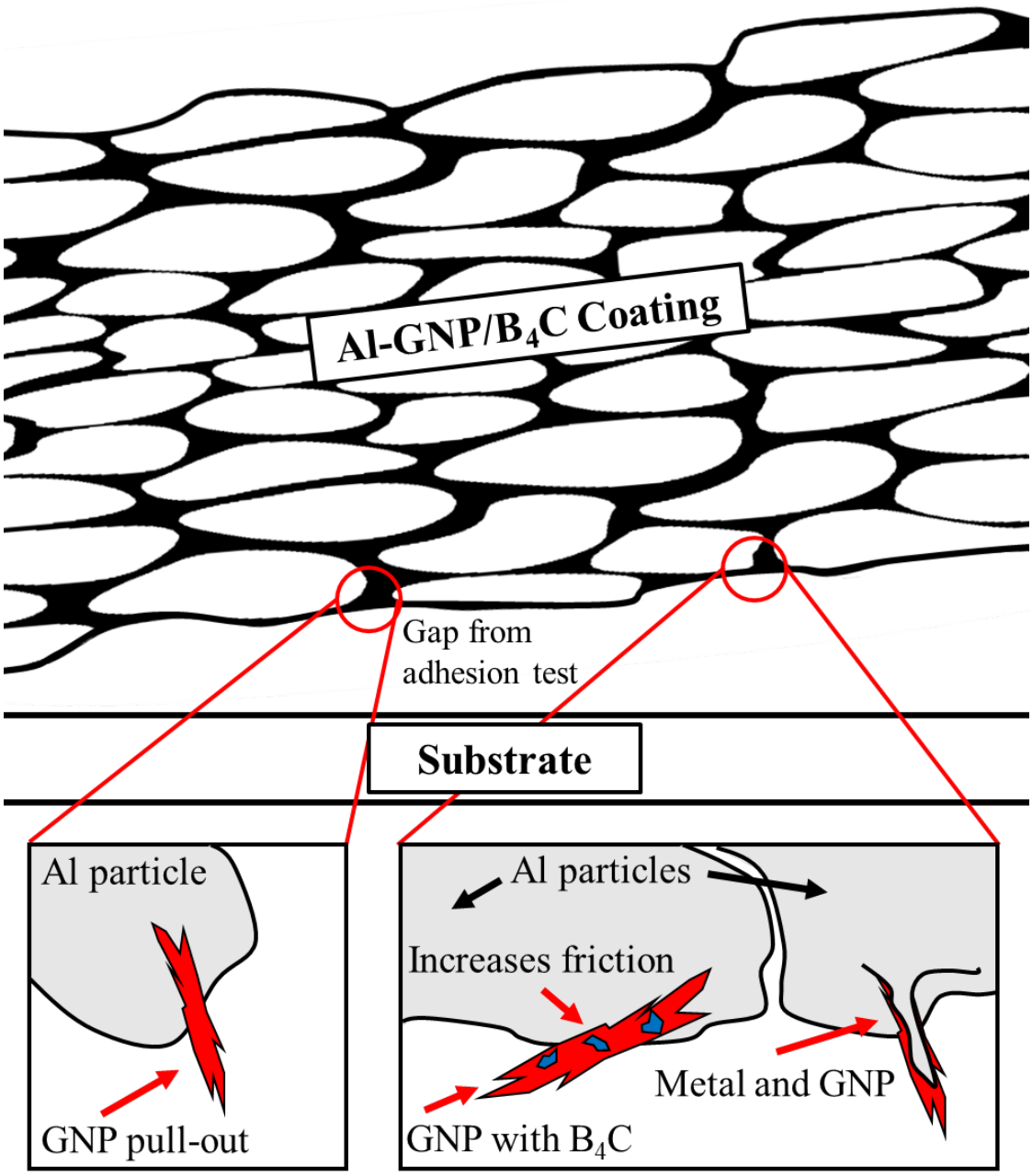

Figure 54. GNP and µB4C strengthening mechanism schematic

The images in Figure 55 are an example of the strengthening mechanism of a GNP pull-out with Al metal attached. There are also likely to be μB_4C particles along this surface and between the GNP and Al. These photos are located at the bottom of the fracture surface from the Al-GNP/μB_4C adhesion test. This GNP was located between the coating and the substrate and was partially pulled from the coating during the fracture.

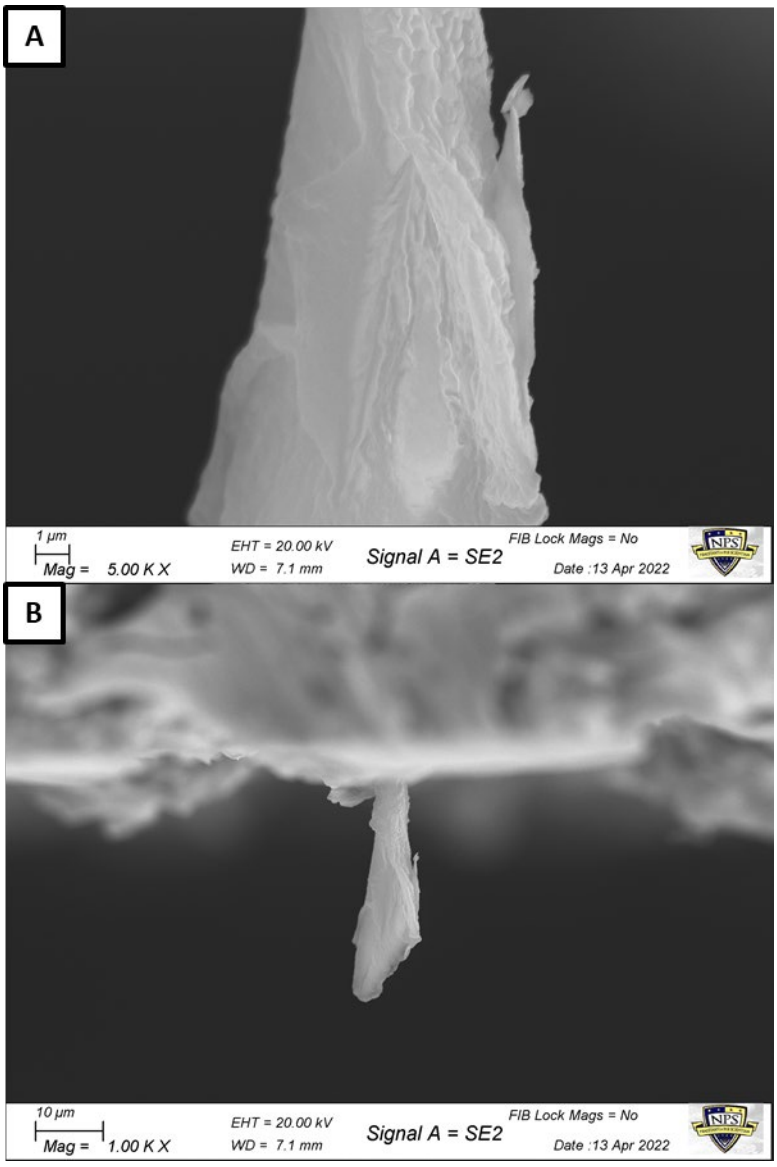

Figure 55. SEM example of a, b) pulled-out GNP bridging the interface between cold-sprayed coating and substrate on Al-GNP/µB4C coating adhesion test fracture surface

The presence of µB4C particles in the splat boundaries of the Al particles helps to strengthen the coatings. This is shown in the maximum adhesion stress in Figure 32 where the Al-µB4C coating had the greatest increase in max stress. However, the microhardness and the nanoindentation both showed a decrease in the hardness of the Al-µB4C coating. The Al-µB4C coating also experienced the lowest mass loss due to wear among the reinforced coatings. Figure 56 shows the µB4C particles located along the splat boundaries. The smooth mass in the upper right-hand corner is the mounting resin that filled the crack in the adhesion test.

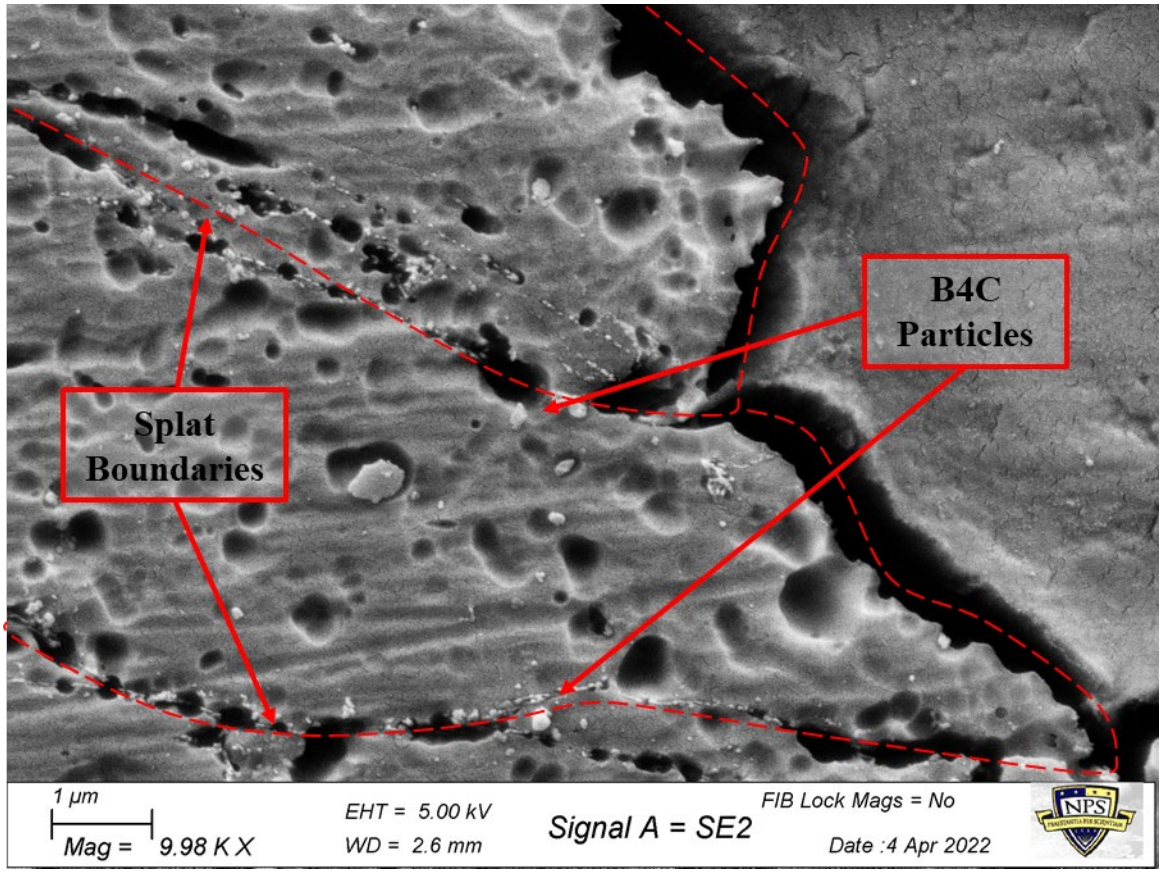

Figure 56. SEM example of µB4C particles in the splat boundaries between Al particles

Synergistic properties were found in the Al-GNP/µB4C coating during nanoindentation. The singly reinforced coatings both had either the same or lower hardness

and elastic modulus than the pure Al coating. But when the reinforcements were combined in the Al-GNP/μB4C coating, an increase in both hardness and elastic modulus was the result. This fits the definition of a synergistic effect given at the end of Chapter II. when combined in the Al coating, the GNPs and μB4C particles create a more significant impact than either substance on its own. Table 15 presents the trends seen in the data. Table 16 explains the trends found in Table 15.

Table 15. Summary of all coating property trends

Property \ Composition		Al		Al-GNP		Al-μB4C		Al-GNP/μB4C	
		Avg	SD	Avg	SD	Avg	SD	Avg	SD
Coating	Thickness [μm]	561	47.4	279	33.2	412	24.7	541	36.1
	Porosity [%]	5.19	2.95	2.88	1.44	0.86	0.73	1.04	0.82
Mechanical Properties	Micro-hardness [GPa]	0.272	0.042	0.476	0.068	0.411	0.046	0.402	0.060
	Nano-hardness [GPa]	0.966	0.197	0.987	0.150	0.752	0.228	1.135	0.297
	Elastic Modulus [GPa]	64.37	12.75	57.78	5.79	62.60	12.34	72.60	11.48
	Plasticity [%]	89.8	2.4	89.3	1.7	91.9	2.1	89.9	2.1
	Adhesion Strength [psi]	1740.0	169.5	1818.0	202.4	2429.0	105.6	2244.0	354.3
Wear	Mass Lost to Wear [g]	0.0006	0.0003	0.0024	0.0003	0.0016	0.0004	0.0020	0.0006
	Max Depth During Wear Test [μm]	8.52	1.78	13.50	2.33	9.21	2.03	11.58	1.81
	Coefficient of Friction [ ]	0.53	0.07	0.53	0.04	0.54	0.06	0.54	0.03

Improved | Same as Aluminum | Worsened

Table 16. Explanation of trends in Table 15

Property		Trend Explanation	Mechanism Explanation
Coating	**Thickness**	A thinner coating under identical spraying conditions denotes issues with either powder flow in the cold spray machine, or with the adhesion of the particles and reinforcements onto the substrate	Two dimensional GNPs often adhere to the inner lining of the powder feed line. High aspect ratio particles such as GNPs also are often blown away due to the high gas speeds
	Porosity	A less porous coating has higher density and shows that the reinforcements aided in the densification of the coatings during the heat treatment process	Particles of μB_4C help to deform the particle on impact and act as point-anchors along splat boundaries
Mechanical Properties	**Micro-hardness**	Micro-hardness measures the hardness over a larger area. These measurements are the average of many grains and they interact more with the reinforcements	Here GNPs located in the splat boundaries greatly increased the average hardness due to their high in-plane tensile strength bearing loads during deformation
	Nano-hardness	Nano-hardness is a more localized measurement of hardness. Most are measurements of a single grain. This trend shows the dual-reinforced coating increased the hardness of the grains deeper inside the splat boundaries	A combination of the mechanism stated for GNPs in micro-hardness and the addition of μB_4C particles that increase the work hardening of the Al particles during the milling process and heat treatment
	Elastic Modulus	Coatings with an increased elastic modulus have higher stiffness. The single-reinforced coatings had a worsened modulus, but when combined together in the dual-reinforced coating, the elastic modulus improved	This synergistic property is from the GNPs and μB_4C particles acting as additional locking mechanisms in splat boundaries. The high in-plane tensile strength and hardness of μB_4C particles work together to stiffen the coating
	Plasticity	A higher percent plasticity means the coating will undergo more plastic deformation under the same load conditions. All of the coatings experienced similar plasticity with Al-μB_4C being slightly higher	Similar to the description above, the μB_4C particles stiffened the coatings, allowing for less plastic deformation by acting as point-anchors
	Adhesion Strength	An increase in adhesion strength shows that the coating has a stronger bond to the substrate. All of the reinforced coatings experienced increased adhesion strength. Coatings containing μB_4C experienced an even greater increase	μB_4C particles, acting as point-anchors, kept the Al particles from fracturing along splat boundaries until a higher stress was reached
Wear	**Mass Lost to Wear**	All reinforced coatings experienced an increase in mass lost to wear when compared to the unreinforced Al coating.	The μB_4C particles were pulled from the coatings and acted as third-body abrasives, and the GNPs allowed more Al particles to be deformed and removed as wear debris due to the sheet sliding property found in GNPs
	Max Depth During Wear Test	Similar to the mass lost during wear, all coatings containing reinforcements experienced deeper wear tracks on average.	More material was removed during identical wear conditions as noted above
	Coefficient of Friction	Coefficients of friction were measured in real-time and averaged over the course of the test. These averages were all consistent regardless of coating composition	No mechanism to note

THIS PAGE INTENTIONALLY LEFT BLANK

V. CONCLUSIONS

A. SUMMARY

The primary focus of this experiment was to study and compare the individual and combined effects of aluminum cold spray coatings, reinforced with GNPs and μB_4C particles. Before this experiment, there had not been any study on the cold spray process using a dual-nano reinforced aluminum composite with GNPs and μB_4C. This study specifically looked at the adhesion of the composite coatings to an aluminum substrate and the cohesion among the coatings. The cold spray method allows for the production of thin coatings with specific desirable mechanical properties. Increased strength, wear and corrosion resistance, and adhesion strength are all desirable properties made possible by composite cold spray coatings. The Department of Defense is always in a constant battle of maintenance on our military equipment. Whether it is corrosion on Naval vessels or surface wear in and on machinery, the military is always faced with protecting our equipment. Cold-sprayed coatings allow for the application of lightweight coatings with specially tailored properties that can protect metal surfaces.

This study met the objectives stated in Chapter I. Hybrid powders were synthesized using high-energy ball milling and single and dual-nanoparticulate reinforced cold-sprayed aluminum coatings were created. These coatings were analyzed and tested to compare hardness, adhesion strength, and wear resistance. Analysis of these coatings included extensive imaging using SEM to look directly at the particulate reinforcements and determine how they improved mechanical properties. Synergistic effects among the reinforcement particulates were noted from the nanoindentation tests. The dual-nanoparticulate reinforced coating experienced an increase in both hardness and elastic modulus, while the single particulate reinforced coatings did not.

B. FUTURE WORKS

The compositions tested in this thesis will be further tested in a high-pressure cold spray system. This testing will show how these compositions form coatings at significantly higher speeds. Al particles will be more deformed and coatings will likely be denser.

Another study that could be done in the future is to look into the corrosion resistance of these compositions. Polarization resistance could be measured to find the resistance to oxidation under galvanic potentials, and the coatings could be exposed to a salt-fog chamber to imitate a sea environment. These samples could then be looked at with EDS to determine any chemical changes. Additionally, the volume percent of reinforcements in these compositions could be altered and examined in a similar way.

APPENDIX A: WEAR DATA MATLAB CODE

All data from each wear test was manipulated in an identical way. The main functions and calculations are provided for the pure Aluminum only. First data was read to a table from the csv file created by the wear tester.

```
%% Data Input
dat_al_1 = readtable('Al_Only_HT_Test_1.csv');
dat_al_2 = readtable('Al_Only_HT_Test_2.csv');
dat_al_3 = readtable('Al_Only_HT_Test_3.csv');
dat_al_4 = readtable('Al_Only_HT_Test_4.csv');
dat_al_5 = readtable('Al_Only_HT_Test_5.csv');
dat_al_6 = readtable('Al_Only_HT_Test_6.csv');
```

The data was then extracted and given a name to work with for the time intervals, coefficients of friction and depth of the encoder.

```
%% Data Extraction
Al_1(:,1) = dat_al_1.Time_min_;
Al_1(:,2) = dat_al_1.CoefficientOfFriction;
Al_1(:,3) = dat_al_1.DepthEncoder_micron_;
```

This data was saved as a .mat file and imported to the plotting function. This function first manipulates the code using the data_manipulator local function. Then plots the coefficients of friction for each test. A similar plot was made for all the depth readings.

```
%% Read Data
load("wear_data.mat");
%% Al Only
[time1,cof1,depth1] = data_manipulator(Al_1);
[time2,cof2,depth2] = data_manipulator(Al_2);
[time3,cof3,depth3] = data_manipulator(Al_3);
[time4,cof4,depth4] = data_manipulator(Al_4);
[time5,cof5,depth5] = data_manipulator(Al_5);
[time6,cof6,depth6] = data_manipulator(Al_6);
figure(1)
plot(time1,cof1)
hold on
plot(time2,cof2)
plot(time3,cof3)
plot(time4,cof4)
plot(Al_time5,Al_cof5)
plot(time6,cof6)
title('COF for Al Only')
ylabel('COF')
xlabel('Time [min]')
legend('Test 1','Test 2','Test 3','Test 4','Test 5','Test 6')
```

The data manipulator function was run separately to try several different methods of smoothing the data. The final method was moving mean as shown below.

```
%% Moving Mean Function
function [time_data,avg_cof,avg_depth] = data_manipulator(data)
    time_data = data(:,1);
    avg_cof =   smoothdata(data(:,2),"movmean",3,"SamplePoints",time_data);
    avg_depth = smoothdata(data(:,3),"movmean",3,"SamplePoints",time_data);
    avg_depth = avg_depth-avg_depth(1);
end
```

The average tests for each composition were compared using a similar plotting method.

```
%% Compared COFs
% Average test for each:
% Al – 5, GNP – 6, B4C – 6, GNP/B4C - 4
figure(9)
plot(Al_time5,Al_cof5)
hold on
plot(GNP_time6,GNP_cof6)
plot(B4C_time6,B4C_cof6)
plot(Both_time4,Both_cof4)
title('COFs Compared')
ylabel('COF')
xlabel('Time [min]')
legend('Al Only','Al-GNP','Al-B4C','Al-GNP/B4C')
```

APPENDIX B: NANOINDENTATION MATLAB CODE

In a similar way to the wear data, the nanoindentation data was fist converted to a .mat file from the data provided from the nanoindentation tester. First, the failed tests needed to be removed. The following code hand selected the test numbers that failed and omits them from the new table. Again, only the code for the pure Aluminum coating is shown.

```
%% Al Only
Al_disp = NaN(160,50);
Al_load = NaN(160,50);
for i = 1:9
    page = append('Test 00',num2str(i));
    displacement = readtable('Al_ONLY_BATCH.xls','Sheet',page,'Range','B:B');
Al_disp((1:length(displacement.DisplacementIntoSurface)),i) =
displacement.DisplacementIntoSurface;
    load = readtable('Al_ONLY_BATCH.xls','Sheet',page,'Range','C:C');
Al_load((1:length(load.LoadOnSample)),i) = load.LoadOnSample;
end
for i = 10:50
    if i==22||i==32||i==40||i==47 % this is for tagged tests
        i = i+1
    else
    page = append('Test 0',num2str(i));
    displacement = readtable('Al_ONLY_BATCH.xls','Sheet',page,'Range','B:B');
Al_disp((1:length(displacement.DisplacementIntoSurface)),i) =
displacement.DisplacementIntoSurface;
    load = readtable('Al_ONLY_BATCH.xls','Sheet',page,'Range','C:C');
Al_load((1:length(load.LoadOnSample)),i) = load.LoadOnSample;
    end
end
```

Next, this data is compiled into a table and loaded into the plotting function.

```
%% Data Reading
T_Al_ONLY = readtable('Al_ONLY_BATCH.xls');
T_Al_GNP =  readtable('Al_GNP_BATCH.xls');
T_Al_B4C =  readtable('Al_B4C_BATCH.xls');
T_Al_GNP_B4C = readtable('Al_GNP_B4C_BATCH.xls');
```

The data was then plotted as a scatter plot with the average plotted in the middle and with an error bar box plotted around the average.

```
%% Scatter Plots
% Function for adding error rectangles
rectplot = @(x,y,sdv_modulus,sdv_hardness,LineColor) rectangle('Position'...
    ,[x-sdv_modulus y-sdv_hardness 2*sdv_modulus 2*sdv_hardness],...
    'EdgeColor',LineColor);
```

```
figure(1)   % Al Only Scatter Plot
plot(T_Al_ONLY.ModulusAtMaxLoad(2:51),T_Al_ONLY.HardnessAtMaxLoad(2:51),'o')
hold on
plot(T_Al_ONLY.ModulusAtMaxLoad(52),T_Al_ONLY.HardnessAtMaxLoad(52),'.r',
'MarkerSize',25)
rectplot(T_Al_ONLY.ModulusAtMaxLoad(52),T_Al_ONLY.HardnessAtMaxLoad(52)...
        ,T_Al_ONLY.ModulusAtMaxLoad(53),T_Al_ONLY.HardnessAtMaxLoad(53),'k');
title('Al Only Nanoindentation')
xlabel('Modulus at Max Load [GPa]')
ylabel('Hardness at Max Load [GPa]')
xlim([0 90])
ylim([0 2])
legend('Nanoindentation Tests','Average')
```

A combined plot of each compositions average and the error boxes were plotted as shown below.

```
figure(5) % Combined Plot of Averages
% Al Only
hold on
plot(T_Al_ONLY.ModulusAtMaxLoad(52),T_Al_ONLY.HardnessAtMaxLoad(52),'.r',
'MarkerSize',25)
rectplot(T_Al_ONLY.ModulusAtMaxLoad(52),T_Al_ONLY.HardnessAtMaxLoad(52)...
        ,T_Al_ONLY.ModulusAtMaxLoad(53),T_Al_ONLY.HardnessAtMaxLoad(53),'r');
% GNP
plot(T_Al_GNP.ModulusAtMaxLoad(52),T_Al_GNP.HardnessAtMaxLoad(52),'.g','MarkerSize',25)
rectplot(T_Al_GNP.ModulusAtMaxLoad(52),T_Al_GNP.HardnessAtMaxLoad(52)...
        ,T_Al_GNP.ModulusAtMaxLoad(53),T_Al_GNP.HardnessAtMaxLoad(53),'g');
% B4C
plot(T_Al_B4C.ModulusAtMaxLoad(52),T_Al_B4C.HardnessAtMaxLoad(52),'.b','MarkerSize',25)
rectplot(T_Al_B4C.ModulusAtMaxLoad(52),T_Al_B4C.HardnessAtMaxLoad(52)...
        ,T_Al_B4C.ModulusAtMaxLoad(53),T_Al_B4C.HardnessAtMaxLoad(53),'b');
% GNP/B4C
plot(T_Al_GNP_B4C.ModulusAtMaxLoad(52),T_Al_GNP_B4C.HardnessAtMaxLoad(52),'.m',
'MarkerSize',25)
rectplot(T_Al_GNP_B4C.ModulusAtMaxLoad(52),T_Al_GNP_B4C.HardnessAtMaxLoad(52)...
        ,T_Al_GNP_B4C.ModulusAtMaxLoad(53),T_Al_GNP_B4C.HardnessAtMaxLoad(53),'m');
title('Nanoindentation Combined Averages')
xlabel('Modulus at Max Load [GPa]')
ylabel('Hardness at Max Load [GPa]')
xlim([0 90])
ylim([0 2])
legend('Al Only','Al-GNP','Al-B4C','Al-GNP/B4C')
```

Plasticity was also calculated using the following function:

```
%% Plasticity Measurement
function [Plasticity,hmax,Pmax] = plasticity(disp_h,load_P)
       [hmax,max_loc] = max(disp_h);    % Max displacement
       Pmax = load_P(max_loc);          % Max Load at max displacement
       k = find(load_P<0);              % Find negative values
       hf_loc = min(k)-1;               % Location of final Depth
       hf = disp_h(hf_loc);             % Final Depth
       Plasticity = 1 - hf/hmax;
end
```

LIST OF REFERENCES

[1] "DOD strategic plan for corrosion prevention and mitigation." Department of Defense, Feb. 2011 [Online]. Available: https://acqnotes.com/Attachments/DOD%20Corrosion%20Prevention%20and%20Mitigation%20Strategic%20Plan%20Feb%202011.pdf

[2] P. Cavaliere and A. Silvello, "Fatigue behaviour of cold sprayed metals and alloys: critical review," *Surf. Eng.*, vol. 32, no. 9, pp. 631–640, Sep. 2016, doi: 10.1179/1743294415Y.0000000100.

[3] T. H. Van Steenkiste, J. R. Smith, and R. E. Teets, "Aluminum coatings via kinetic spray with relatively large powder particles," *Surf. Coat. Technol.*, vol. 154, no. 2–3, pp. 237–252, May 2002, doi: 10.1016/S0257-8972(02)00018-X.

[4] H. Assadi, F. Gärtner, T. Stoltenhoff, and H. Kreye, "Bonding mechanism in cold gas spraying," *Acta Mater.*, vol. 51, no. 15, pp. 4379–4394, Sep. 2003, doi: 10.1016/S1359-6454(03)00274-X.

[5] M. Grujicic, C. L. Zhao, C. Tong, W. S. DeRosset, and D. Helfritch, "Analysis of the impact velocity of powder particles in the cold-gas dynamic-spray process," *Mater. Sci. Eng. A*, vol. 368, no. 1–2, pp. 222–230, Mar. 2004, doi: 10.1016/j.msea.2003.10.312.

[6] R. N. Raoelison et al., "Cold gas dynamic spray technology: A comprehensive review of processing conditions for various technological developments till to date," *Addit. Manuf.*, vol. 19, pp. 134–159, Jan. 2018, doi: 10.1016/j.addma.2017.07.001.

[7] W. Wong, E. Irissou, A. N. Ryabinin, J.-G. Legoux, and S. Yue, "Influence of helium and nitrogen gases on the properties of cold gas dynamic sprayed pure titanium coatings," *J. Therm. Spray Technol.*, vol. 20, no. 1–2, pp. 213–226, Jan. 2011, doi: 10.1007/s11666-010-9568-y.

[8] H. Assadi et al., "On parameter selection in cold spraying," *J. Therm. Spray Technol.*, vol. 20, no. 6, pp. 1161–1176, Dec. 2011, doi: 10.1007/s11666-011-9662-9.

[9] B. Jodoin, L. Ajdelsztajn, E. Sansoucy, A. Zúñiga, P. Richer, and E. J. Lavernia, "Effect of particle size, morphology, and hardness on cold gas dynamic sprayed aluminum alloy coatings," *Surf. Coat. Technol.*, vol. 201, no. 6, pp. 3422–3429, Dec. 2006, doi: 10.1016/j.surfcoat.2006.07.232.

[10] D. A. Rigney, "Sliding wear of metals," *Annu. Rev. Mater. Sci.*, vol. 18, no. 1, pp. 141–163, Aug. 1988, doi: 10.1146/annurev.ms.18.080188.001041.

[11] V. Domnich, S. Reynaud, R. A. Haber, and M. Chhowalla, “Boron carbide: Structure, properties, and stability under stress,” *J. Am. Ceram. Soc.*, vol. 94, no. 11, pp. 3605–3628, Nov. 2011, doi: 10.1111/j.1551-2916.2011.04865.x.

[12] F. Thévenot, “Boron carbide—A comprehensive review,” *J. Eur. Ceram. Soc.*, vol. 6, no. 4, pp. 205–225, Jan. 1990, doi: 10.1016/0955-2219(90)90048-K.

[13] “Boron carbide powder / B4C powder (B4C, 99.9%).” U.S. Research Nanomaterials, Inc [Online]. Available: https://www.us-nano.com/inc/sdetail/6703

[14] A. Nieto, H. Yang, L. Jiang, and J. M. Schoenung, “Reinforcement size effects on the abrasive wear of boron carbide reinforced aluminum composites,” *Wear*, vol. 390–391, pp. 228–235, Nov. 2017, doi: 10.1016/j.wear.2017.08.002.

[15] “PubChem compound summary for CID 6337058, Boron-10.” National Center for Biotechnology Information, 2022 [Online]. Available: https://pubchem.ncbi.nlm.nih.gov/compound/Boron-10

[16] “3M^{TM} 10B enriched boron carbide.” 3M Technical Ceramics, Inc., 2020 [Online]. Available: https://multimedia.3m.com/mws/media/950554O/3m-10b-enriched-boron-carbide-data-sheet.pdf

[17] A. Srivastava, “A review on fabrication and characterization of aluminium metal matrix composite (AMMC),” *Int. J. Adv. Res. Innov.*, vol. 2, no. 2, pp. 516–521, 2014.

[18] W. Choi, I. Lahiri, R. Seelaboyina, and Y. S. Kang, “Synthesis of graphene and its applications: A review,” *Crit. Rev. Solid State Mater. Sci.*, vol. 35, no. 1, pp. 52–71, Feb. 2010, doi: 10.1080/10408430903505036.

[19] C. Lee, X. Wei, J. W. Kysar, and J. Hone, “Measurement of the elastic properties and intrinsic strength of monolayer graphene,” *Science*, vol. 321, no. 5887, pp. 385–388, Jul. 2008, doi: 10.1126/science.1157996.

[20] I. W. Frank, D. M. Tanenbaum, A. M. van der Zande, and P. L. McEuen, “Mechanical properties of suspended graphene sheets,” *J. Vac. Sci. Technol. B Microelectron. Nanometer Struct.*, vol. 25, no. 6, p. 2558, 2007, doi: 10.1116/1.2789446.

[21] A. Nieto, D. Lahiri, and A. Agarwal, “Synthesis and properties of bulk graphene nanoplatelets consolidated by spark plasma sintering,” *Carbon*, vol. 50, no. 11, pp. 4068–4077, Sep. 2012, doi: 10.1016/j.carbon.2012.04.054.

[22] A. Nieto, A. Bisht, D. Lahiri, C. Zhang, and A. Agarwal, “Graphene reinforced metal and ceramic matrix composites: a review,” *Int. Mater. Rev.*, vol. 62, no. 5, pp. 241–302, Jul. 2017, doi: 10.1080/09506608.2016.1219481.

[23] M. Li et al., “Microstructure evolution and properties of graphene nanoplatelets reinforced aluminum matrix composites,” *Mater. Charact.*, vol. 140, pp. 172–178, Jun. 2018, doi: 10.1016/j.matchar.2018.04.007.

[24] J. Yao et al., “The enhanced tribological properties of NiAl intermetallics: Combined lubrication of multilayer graphene and WS2,” *Tribol. Lett.*, vol. 56, no. 3, pp. 573–582, Dec. 2014, doi: 10.1007/s11249-014-0439-4.

[25] R. Huang, M. Sone, W. Ma, and H. Fukanuma, “The effects of heat treatment on the mechanical properties of cold-sprayed coatings,” *Surf. Coat. Technol.*, vol. 261, pp. 278–288, Jan. 2015, doi: 10.1016/j.surfcoat.2014.11.017.

[26] M. Rashad, F. Pan, A. Tang, M. Asif, and M. Aamir, “Synergetic effect of graphene nanoplatelets (GNPs) and multi-walled carbon nanotube (MW-CNTs) on mechanical properties of pure magnesium,” *J. Alloys Compd.*, vol. 603, pp. 111–118, Aug. 2014, doi: 10.1016/j.jallcom.2014.03.038.

[27] H. Kwon, S. Cho, M. Leparoux, and A. Kawasaki, “Dual-nanoparticulate-reinforced aluminum matrix composite materials,” *Nanotechnology*, vol. 23, no. 22, p. 225704, Jun. 2012, doi: 10.1088/0957-4484/23/22/225704.

[28] H. Kwon, G.-G. Lee, S.-G. Kim, B.-W. Lee, W.-C. Seo, and M. Leparoux, “Mechanical properties of nanodiamond and multi-walled carbon nanotubes dual-reinforced aluminum matrix composite materials,” *Mater. Sci. Eng. A*, vol. 632, pp. 72–77, Apr. 2015, doi: 10.1016/j.msea.2015.02.057.

[29] S. Dhandapani, T. Rajmohan, K. Palanikumar, and M. Charan, “Synthesis and characterization of dual particle (MWCT+B $_4$ C) reinforced sintered hybrid aluminum matrix composites,” *Part. Sci. Technol.*, vol. 34, no. 3, pp. 255–262, May 2016, doi: 10.1080/02726351.2015.1069431.

[30] E. Ghasali, P. Sangpour, A. Jam, H. Rajaei, K. Shirvanimoghaddam, and T. Ebadzadeh, “Microwave and spark plasma sintering of carbon nanotube and graphene reinforced aluminum matrix composite,” *Arch. Civ. Mech. Eng.*, vol. 18, no. 4, pp. 1042–1054, Sep. 2018, doi: 10.1016/j.acme.2018.02.006.

[31] S. Polat, Y. Sun, E. Çevik, and H. Colijn, “Microstructure and synergistic reinforcing activity of GNPs-B4C dual-micro and nano supplements in Al-Si matrix composites,” *J. Alloys Compd.*, vol. 806, pp. 1230–1241, Oct. 2019, doi: 10.1016/j.jallcom.2019.06.342.

[32] T. Norrell, G. Ferguson, T. Ansell, T. Saladin, A. Nardi, and A. Nieto, “Synthesis and corrosion behavior of cold sprayed dual nanoparticle reinforced Al coatings,” *Surf. Coat. Technol.*, vol. 401, p. 126280, Nov. 2020, doi: 10.1016/ j.surfcoat.2020.126280.

[33] P. S. Gilman and J. S. Benjamin, “Mechanical alloying,” *Annu. Rev. Mater. Sci.*, vol. 13, no. 1, pp. 279–300, Aug. 1983, doi: 10.1146/annurev.ms.13.080183.001431.

[34] “Mixer/Mill® high energy ball mill.” SPEX Sample Prep, 2020 [Online]. Available: https://www.spexsampleprep.com/uploads/files/brochures/1006-113946-Mixer_Mill%20Brochure%202020.pdf

[35] T. Y. Ansell, T. Hanneman, A. Gonzalez-Perez, C. Park, and A. Nieto, “Effect of high energy ball milling on spherical metallic powder particulates for additive manufacturing,” *Part. Sci. Technol.*, vol. 39, no. 8, pp. 981–989, Nov. 2021, doi: 10.1080/02726351.2021.1876192.

[36] S. B. Pitchuka et al., “Dry sliding wear behavior of cold sprayed aluminum amorphous/nanocrystalline alloy coatings,” *Surf. Coat. Technol.*, vol. 238, pp. 118–125, Jan. 2014, doi: 10.1016/j.surfcoat.2013.10.055.

[37] S. B. Pitchuka, D. Lahiri, G. Sundararajan, and A. Agarwal, “Scratch-induced deformation behavior of cold-sprayed aluminum amorphous/nanocrystalline coatings at multiple load scales,” *J. Therm. Spray Technol.*, vol. 23, no. 3, pp. 502–513, Feb. 2014, doi: 10.1007/s11666-013-0021-x.

[38] K. Bobzin, W. Wietheger, J. Hebing, and L. Gerdt, “Softening behavior of cold-sprayed aluminum-based coatings AA1200 and AA7075 during annealing,” *J. Therm. Spray Technol.*, vol. 30, no. 1–2, pp. 358–370, Jan. 2021, doi: 10.1007/s11666-020-01121-7.

[39] C. Comte and J. von Stebut, “Microprobe-type measurement of Young’s modulus and Poisson coefficient by means of depth sensing indentation and acoustic microscopy,” *Surf. Coat. Technol.*, vol. 154, no. 1, pp. 42–48, May 2002, doi: 10.1016/S0257-8972(01)01706-6.

[40] W. C. Oliver and G. M. Pharr, “An improved technique for determining hardness and elastic modulus using load and displacement sensing indentation experiments,” *J. Mater. Res.*, vol. 7, no. 6, pp. 1564–1583, Jun. 1992, doi: 10.1557/JMR.1992.1564.

[41] W. C. Oliver and G. M. Pharr, “Measurement of hardness and elastic modulus by instrumented indentation: Advances in understanding and refinements to methodology,” *J. Mater. Res.*, vol. 19, no. 1, pp. 3–20, Jan. 2004, doi: 10.1557/jmr.2004.19.1.3.

[42] G. F. Vander Voort, *Metallography, principles and practice*. Materials Park, Ohio: ASM International, 1999.

[43] I. A. Ibrahim, F. A. Mohamed, and E. J. Lavernia, “Particulate reinforced metal matrix composites — a review,” *J. Mater. Sci.*, vol. 26, no. 5, pp. 1137–1156, Mar. 1991, doi: 10.1007/BF00544448.

THIS PAGE INTENTIONALLY LEFT BLANK

INITIAL DISTRIBUTION LIST

1. Defense Technical Information Center
   Ft. Belvoir, Virginia

2. Dudley Knox Library
   Naval Postgraduate School
   Monterey, California